Probing chiral-even and chiral-odd leading twist quark generalized parton distributions through the exclusive photoproduction of a $\gamma\rho$ pair

Goran Duplančić,[1,*] Saad Nabeebaccus[2,†] Kornelija Passek-Kumerički,[1,‡] Bernard Pire[3,§]
Lech Szymanowski,[4,∥] and Samuel Wallon[2,¶]

[1]*Theoretical Physics Division, Rudjer Bošković Institute, HR-10002 Zagreb, Croatia*
[2]*Université Paris-Saclay, CNRS/IN2P3, IJCLab, 91405 Orsay, France*
[3]*CPHT, CNRS, Ecole polytechnique, Institut Polytechnique de Paris, 91128 Palaiseau, France*
[4]*National Centre for Nuclear Research (NCBJ), 02-093 Warsaw, Poland*

We extend our studies of a new class of $2 \to 3$ exclusive processes using the collinear factorization framework by considering the exclusive photoproduction of a $\gamma\rho$ pair, in the kinematics where the pair has a large invariant mass, and the outgoing ρ meson has a sufficiently large transverse momentum to not resonate with the nucleon. We cover the whole kinematical range from medium energies in fixed-target experiments to very large energies of colliders, by considering the experimental conditions of JLab 12-GeV, COMPASS, and future EIC and LHC (in ultra-peripheral collisions) cases. One of the main interests in studying the present process is that it provides access to both chiral-even and chiral-odd generalized parton distributions, depending on the polarization of the outgoing ρ meson, both at leading twist. Our analysis covers both neutral and charged ρ mesons. We find that the orders of magnitude of the obtained cross sections are sufficiently large for a dedicated experimental analysis to be performed, especially at JLab, for both longitudinally and transversely polarized ρ. Furthermore, we compute the linear photon beam polarization asymmetry which is sizable for a longitudinally polarized meson. These predictions are obtained for both the asymptotic distribution amplitude (DA) and the *holographic* DA.

I. INTRODUCTION

In the present study, we extend our previous analysis in Ref. [1] of generalized parton distributions (GPDs) in $2 \to 3$ exclusive processes, e.g. Refs. [2–10], by considering

$$\gamma(q, \epsilon_q) + N(p_1, \lambda_1) \to \gamma(k, \epsilon_k) + N'(p_2, \lambda_2) + \rho(p_\rho, \epsilon_\rho), \tag{1.1}$$

in the kinematical range from medium energies in fixed-target experiments to very large energies of colliders, which correspond to the experimental environments of

*gorand@thphys.irb.hr
†saad.nabeebaccus@ijclab.in2p3.fr
‡passek@irb.hr
§bernard.pire@polytechnique.edu
∥Lech.Szymanowski@ncbj.gov.pl
¶samuel.wallon@ijclab.in2p3.fr

JLab 12-GeV, COMPASS, the future EIC and LHC in ultra-peripheral collisions (UPCs). The main motivation for considering the above photoproduction process is that it gives access to both leading-twist chiral-even (CE) and chiral-odd (CO) GPDs, depending on the polarization of the outgoing ρ meson, described using its distribution amplitude (DA), also at the leading twist. In particular, this process allows us to learn more about the badly known chiral-odd GPDs. Factorization for this process was recently proved in Refs. [11,12], in which the hard scale is provided by the large relative transverse momentum of the outgoing γ/ρ meson. The work presented here builds upon our earlier publications [13,14] and our more recent work [1]. One should note that the present paper extends the study performed in Ref. [13], which focused on the neutral ρ^0 meson, to $\rho^{0,\pm}$ mesons of any possible charge.

The paper is organized as follows. Details regarding the kinematics are recalled in Sec. II. In Sec. III, the non-perturbative inputs, namely the GPDs and the DAs, are presented. In Sec. IV, we show how the amplitude can be expressed in terms of tensorial structures, and how the computation reduces to that of basic building blocks. This section ends with a discussion of polarization asymmetries. Results for the cross sections and linear polarization asymmetries with respect to the incoming photon are the

subject of Sec. V. This section ends with an estimation of counting rates at various experiments. We end with conclusions in Sec. VI. In Appendix A, the diagrams for the chiral-odd case are given in terms of building block integrals, for both the asymptotic and holographic DAs. In Appendix B, we discuss the effect, on the cross section, of the experimental constraints at JLab on the angle of the outgoing photon. Finally, in Appendix C, the vanishing of the circular polarization asymmetry with respect to the incoming photon for the chiral-even case is discussed.

II. KINEMATICS

From Eq. (1.1), one can define the following momenta:

$$P^\mu = \frac{p_1^\mu + p_2^\mu}{2}, \qquad \Delta^\mu = p_2^\mu - p_1^\mu. \qquad (2.1)$$

All momenta are decomposed in a Sudakov basis, such that a generic vector v can be written as

$$v^\mu = a n^\mu + b p^\mu + v_\perp^\mu, \qquad (2.2)$$

with the two light-cone vectors p and n given by

$$p^\mu = \frac{\sqrt{s}}{2}(1,0,0,1), \quad n^\mu = \frac{\sqrt{s}}{2}(1,0,0,-1), \quad p \cdot n = \frac{s}{2}. \quad (2.3)$$

For the transverse vectors, we use the following convention:

$$v_\perp^\mu = (0, v^x, v^y, 0), \qquad v_\perp^2 = -\vec{v}_t^2. \qquad (2.4)$$

The particle momenta for the process now read

$$p_1^\mu = (1+\xi)p^\mu + \frac{M^2}{s(1+\xi)}n^\mu, \qquad (2.5)$$

$$p_2^\mu = (1-\xi)p^\mu + \frac{M^2 + \vec{\Delta}_t^2}{s(1-\xi)}n^\mu + \Delta_\perp^\mu, \qquad (2.6)$$

$$q^\mu = n^\mu, \qquad (2.7)$$

$$k^\mu = \alpha n^\mu + \frac{(\vec{p}_t - \vec{\Delta}_t/2)^2}{\alpha s}p^\mu + p_\perp^\mu - \frac{\Delta_\perp^\mu}{2}, \qquad (2.8)$$

$$p_\rho^\mu = \alpha_\rho n^\mu + \frac{(\vec{p}_t + \vec{\Delta}_t/2)^2 + M_\rho^2}{\alpha_\rho s}p^\mu - p_\perp^\mu - \frac{\Delta_\perp^\mu}{2}, \quad (2.9)$$

where M and M_ρ are the masses of the nucleon and the ρ meson respectively. The square of the center-of-mass energy of the photon-nucleon system is then

$$S_{\gamma N} = (q + p_1)^2 = (1+\xi)s + M^2, \qquad (2.10)$$

while the square of the transferred momentum is

$$t = (p_2 - p_1)^2 = -\frac{1+\xi}{1-\xi}\vec{\Delta}_t^2 - \frac{4\xi^2 M^2}{1-\xi^2}. \qquad (2.11)$$

The invariant mass squared of the $\gamma\rho$ system, $M_{\gamma\rho}^2$, provides the hard scale for factorization. This is guaranteed by having a large *relative* transverse momentum $\vec{p}_t$ between the outgoing photon and meson.

Collinear QCD factorization implies that

$$-u' = (p_\rho - q)^2, \quad -t' = (k-q)^2, \quad M_{\gamma\rho}^2 = (p_\rho + k)^2, \quad (2.12)$$

are large, while

$$-t = (p_2 - p_1)^2, \qquad (2.13)$$

needs to be small. In practice, we employ the cuts

$$-u', -t' > 1 \text{ GeV}^2, \qquad -t < 0.5 \text{ GeV}^2. \qquad (2.14)$$

We note that these cuts are sufficient to ensure that $M_{\gamma\rho}^2 > 2 \text{ GeV}^2$. Furthermore, the above kinematical cuts ensure that the $\rho N'$ invariant mass, $M_{\rho N'}$, is *completely* out of the resonance region. Indeed, through a numerical analysis, taking into account Eq. (2.14), we find that[1]

$$M_{\rho N'}^2 > 3.11 \text{ GeV}^2, \qquad (2.15)$$

which is much larger than the mass squared of the Δ baryon, $m_\Delta^2 \approx 1.52 \text{ GeV}^2$. Thus, unlike the case of the charged pion in Ref. [1], we find that the larger mass of the ρ meson with respect to the pion mass is such that $M_{\rho N'}^2$ is pushed to larger values.

Neglecting $\vec{\Delta}_t$ in front of $\vec{p}_t$, as well as hadronic masses, we have that the approximate kinematics, as used in the hard part of the factorized amplitude, is

$$M_{\gamma\rho}^2 \approx \frac{\vec{p}_t^2}{\alpha\bar\alpha}, \qquad \alpha_\rho \approx 1 - \alpha \equiv \bar\alpha, \qquad \xi = \frac{\tau}{2-\tau}, \qquad (2.16)$$

$$\tau \approx \frac{M_{\gamma\rho}^2}{S_{\gamma N} - M^2}, \quad -t' \approx \bar\alpha M_{\gamma\rho}^2, \quad -u' \approx \alpha M_{\gamma\rho}^2. \quad (2.17)$$

We choose as independent variables $(-t)$, $(-u')$ and $M_{\gamma\rho}^2$.

Regarding the polarization vectors, we work in the *axial gauge*, such that $p \cdot \varepsilon = 0$. In particular, this implies that the polarization vector of the initial photon is given by

$$\varepsilon_q^\mu = \varepsilon_{q\perp}^\mu, \qquad (2.18)$$

---

[1]In all rigor, we should also exclude the kinematical region where one of the pion decay products from the ρ meson resonates with the final nucleon. Such a constraint is however difficult to fulfill at our level since we do not specify the kinematics of the ρ decay.

i.e. it only has nonzero components in the transverse plane. For the polarization vector of the outgoing photon, one obtains

$$\epsilon_k^\mu = \epsilon_{k\perp}^\mu - \frac{\epsilon_{k\perp} \cdot k_\perp}{p \cdot k} p^\mu. \tag{2.19}$$

Regarding the polarization of the ρ meson, we have[2]

$$\epsilon_\rho^\mu(p_\rho, L) = \frac{1}{M_\rho} p_\rho^\mu - \frac{M_\rho}{(p \cdot p_\rho)} p^\mu, \tag{2.20}$$

for the longitudinally polarized case. For the transversely polarized ρ meson, we exploit the transversity relation $p_\rho \cdot \epsilon_\rho(p_\rho, T) = 0$ to write the polarization vector as

$$\epsilon_\rho^\mu(p_\rho, T) = \epsilon_{\rho\perp}^\mu - \frac{\epsilon_{\rho\perp} \cdot p_\rho}{p \cdot p_\rho} p^\mu, \tag{2.21}$$

where we have chosen the basis for which $p \cdot \epsilon_\rho(p_\rho, T) = 0$. The sum over all three polarizations gives

$$\sum_{i=L,T} \epsilon_\rho^\mu(p_\rho, i) \epsilon_\rho^{\nu*}(p_\rho, i) = -g^{\mu\nu} + \frac{p_\rho^\mu p_\rho^\nu}{m_\rho^2}. \tag{2.22}$$

Using Eqs. (2.20) and (2.21), restricting the sum to only *transverse* polarizations leads to

$$\sum_T \epsilon_\rho^\mu(p_\rho, T) \epsilon_\rho^{\nu*}(p_\rho, T)$$

$$= -g_\perp^{\mu\nu} + \frac{p^\mu p_{\rho\perp}^\nu + p^\nu p_{\rho\perp}^\mu}{p \cdot p_\rho} - \frac{p_{\rho\perp}^2}{(p \cdot p_\rho)^2} p^\mu p^\nu, \tag{2.23}$$

where $p_{\rho\perp} \equiv -p_\perp - \frac{\Delta_\perp}{2}$; see Eq. (2.9).

Further details on the kinematics can be found in our previous works [1,13,14].

III. NONPERTURBATIVE INPUTS

For the self-consistency of the paper, we choose to recall the basic nonperturbative ingredients needed for computing the amplitude.

A. Generalized parton distributions

For our case, both the $p \to n$ and $n \to p$ quark transition GPDs are needed. By isospin symmetry, they are identical and are related to the proton GPD by the relation [15]

$$\langle n|\bar{d}\Gamma u|p\rangle = \langle p|\bar{u}\Gamma d|n\rangle = \langle p|\bar{u}\Gamma u|p\rangle - \langle p|\bar{d}\Gamma d|p\rangle. \tag{3.1}$$

Therefore, we only use the proton GPDs in practice. The chiral-even GPDs of a parton q (where $q = u$, d) in the nucleon target are defined by [16]

$$\langle p(p_2, \lambda_2)|\bar{q}\left(-\frac{y}{2}\right)\gamma^+ q\left(\frac{y}{2}\right)|p(p_1, \lambda_1)\rangle = \int_{-1}^1 dx \, e^{-\frac{i}{2}x(p_1^+ + p_2^+)y^-} \bar{u}(p_2, \lambda_2)\left[\gamma^+ H^q(x, \xi, t) + \frac{i}{2m}\sigma^{+\alpha}\Delta_\alpha E^q(x, \xi, t)\right] u(p_1, \lambda_1), \tag{3.2}$$

for the chiral-even vector GPDs, and

$$\langle p(p_2, \lambda_2)|\bar{q}\left(-\frac{y}{2}\right)\gamma^+\gamma^5 q\left(\frac{y}{2}\right)|p(p_1, \lambda_1)\rangle = \int_{-1}^1 dx \, e^{-\frac{i}{2}x(p_1^+ + p_2^+)y^-} \bar{u}(p_2, \lambda_2)\left[\gamma^+\gamma^5 \tilde{H}^q(x, \xi, t) + \frac{1}{2m}\gamma^5\Delta^+ \tilde{E}^q(x, \xi, t)\right] u(p_1, \lambda_1). \tag{3.3}$$

for chiral-even axial GPDs. In the above, λ_1 and λ_2 are the light-cone helicities of the nucleons with momenta p_1 and p_2. In our analysis, the contributions from E^q and $\tilde{E}^q$ are neglected, since they are suppressed by kinematical factors at the cross-section level; see Eq. (4.32).

The transversity (chiral-odd) GPD of a quark q is defined by

$$\langle p(p_2, \lambda_2)|\bar{q}\left(-\frac{y}{2}\right)i\sigma^{+j} q\left(\frac{y}{2}\right)|p(p_1, \lambda_1)\rangle = \int_{-1}^1 dx \, e^{-\frac{i}{2}x(p_1^+ + p_2^+)y^-} \bar{u}(p_2, \lambda_2)[i\sigma^{+j}H_T^q(x, \xi, t) + ...] u(p_1, \lambda_1), \tag{3.4}$$

where ... denotes the remaining three chiral-odd GPDs whose contributions are omitted in the present analysis.

---

[2]Our conventions are such that $\epsilon_\rho^\mu(p_\rho, L) = (0, 0, 0, -1)$ in the ρ-meson rest frame.

The GPDs are parametrized in terms of double distributions [17]. The details can be found in Refs. [13,14], and we do not repeat them here. The t dependence of the GPDs is modeled by a simplistic dipole ansatz, discussed in Appendix E of Ref. [1].

In our current study, which is performed at leading order in α_s, we neglect any evolution of the GPDs/parton distribution functions (PDFs), and take a fixed factorization scale of $\mu_F^2 = 10\ \mathrm{GeV}^2$. As in Refs. [1,13,14], the PDF data sets that we use to construct the GPDs are as follows:

(1) For $xq(x)$, we use the GRV-98 parametrization [18], as made available from the Durham database.

(2) For $x\Delta q(x)$, we use the GRSV-2000 parametrization [19], also available from the Durham database. Two scenarios are proposed within this parametrization:

    (a) The *standard* scenario, for which the light sea quark and antiquark distributions are *flavor symmetric*.

    (b) The *valence* scenario, which corresponds to *flavor-asymmetric* light sea quark densities.

        The above two scenarios can be used to obtain an order-of-magnitude estimate of the theoretical uncertainties.[3]

B. Distribution amplitudes

The chiral-even light-cone DA for the longitudinally polarized ρ_L meson is defined, at the leading twist 2, by the matrix element [20],

$$\langle 0|\bar{q}(0)\gamma^\mu T^i q(x)|\rho_L^i(p_\rho,\varepsilon_\rho)\rangle = p_\rho^\mu f_\rho^\parallel \int_0^1 dz\, e^{-izp_\rho\cdot x}\phi_\parallel(z),$$
(3.5)

with $f_\rho^\parallel = 216\ \mathrm{MeV}$ and $i = 0, \pm$.[4] In the above, $q = (u\,d)$ is a two-dimensional vector in flavor space, and the matrices T^i (in flavor space) are defined by

$$T^0 = \frac{1}{\sqrt{2}}\begin{pmatrix} 1 & 0 \\ 0 & -1 \end{pmatrix}, \quad T^+ = \begin{pmatrix} 0 & 0 \\ 1 & 0 \end{pmatrix}, \quad T^- = \begin{pmatrix} 0 & 1 \\ 0 & 0 \end{pmatrix}. \quad (3.6)$$

The chiral-odd light-cone DA for the transversely polarized meson vector ρ_T is defined as

$$\langle 0|\bar{q}(0)\sigma^{\mu\nu}T^i q(x)|\rho_T^i(p_\rho,\varepsilon_\rho)\rangle$$
$$= i(\varepsilon_\rho^\mu p_\rho^\nu - \varepsilon_\rho^\nu p_\rho^\mu)f_\rho^\perp \int_0^1 dz\, e^{-izp_\rho\cdot x}\phi_\perp(z), \quad (3.7)$$

where ε_ρ^μ is the ρ-meson transverse polarization and $f_\rho^\perp = 160\ \mathrm{MeV}$.

For the computation, we use the asymptotic form of the distribution amplitude, ϕ^{as}, as well as an alternative form, which is often called the "holographic" DA, ϕ^{hol}. They are given by

$$\phi^{\mathrm{as}}(z) = 6z(1-z), \quad (3.8)$$

$$\phi^{\mathrm{hol}}(z) = \frac{8}{\pi}\sqrt{z(1-z)}, \quad (3.9)$$

where both are normalized to 1. With the above two forms of the DA, the integration over z can be performed analytically. For the chiral-even case, including the building block integrals, the results can be found in Appendix D of Ref. [14] for the asymptotic DA case, and in Appendix C of Ref. [1] for the holographic DA case. For the chiral-odd case, the results can be found in Appendix A.

IV. THE COMPUTATION

A. Gauge-invariant decomposition of the hard amplitude

In the framework of collinear factorization, we set $\vec{\Delta}_t = 0$ in the hard amplitude, which implies that $(-t) = (-t)_{\mathrm{min}}$, where

$$(-t)_{\mathrm{min}} = \frac{4\xi^2 M^2}{1-\xi^2}. \quad (4.1)$$

For the sake of completeness, we remind the reader of the properties of the diagrams contributing to the coefficient function, which significantly simplify the calculation. The hard part is described at leading order in α_s by 20 Feynman diagrams. As discussed in Refs. [1,14], half of the diagrams are related by C-parity transformations.[5]

The sets of diagrams (without including charge factors) are denoted as $(\cdots)$. We denote the A and B diagrams by the order in which the incoming photon and virtual gluon join one of the quark lines. The numbers (1 to 5) denote the five different ways of attaching the outgoing photon to the quark lines. The remaining set of diagrams, C and D, is obtained by exchanging the role of the two quarks in the t channel. In practice, one obtains four separately QED gauge-invariant sets of diagrams, namely $(AB)_{123}$, $(AB)_{45}$, $(CD)_{12}$ and $(CD)_{345}$ [1,14]. Figure 1 shows the first two sets.

Defining the charges Q_q through $e_q = Q_q|e|$, by QED gauge invariance, one can write any amplitude for photon meson production as the sum of three separate gauge-invariant terms, in the form

$$\mathcal{M} = (Q_1^2 + Q_2^2)\mathcal{M}_{\mathrm{sum}} + (Q_1^2 - Q_2^2)\mathcal{M}_{\mathrm{diff}} + 2Q_1 Q_2 \mathcal{M}_{\mathrm{prod}},$$
(4.2)

---

[3]Using more recent tables for the PDFs leads to variations that are smaller than the above-mentioned theoretical uncertainties. This effect was studied in Ref. [13] (see e.g. Fig. 8).

[4]The wave functions are $|\rho^0\rangle = \frac{1}{\sqrt{2}}(|u\bar{u}\rangle - |d\bar{d}\rangle)$, $|\rho^+\rangle = |u\bar{d}\rangle$ and $|\rho^-\rangle = |d\bar{u}\rangle$ for the ρ^0-, ρ^+- and ρ^- mesons respectively.

[5]This corresponds to a C-parity transformation ($z \leftrightarrow 1-z$ and $x \leftrightarrow -x$) *after* the electric charges have been factored out, such that effectively, q and $\bar{q}$ have a charge of 1.
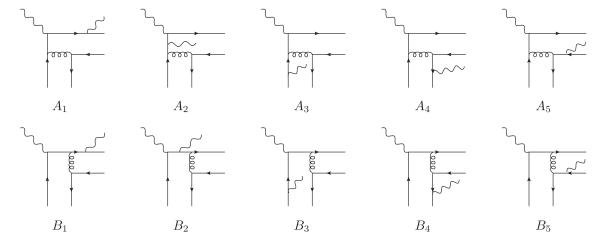
FIG. 1. Half of the Feynman diagrams contributing to the hard part of the amplitude.

where Q_1 is the charge of the quark entering the DA and Q_2 is the charge of the quark leaving the DA, in each diagram.

B. Chiral-even case

The parity properties of the $q\bar{q}$ correlators appearing in the DA and in the GPDs allow the separation of the contributions for parity $(+)$, denoted as S and parity $(-)$, denoted as P. Only two structures occur in the hard part, namely SS (no γ^5 matrices, vector GPD case) and SP (one γ^5, axial GPD case).[6]

A careful examination of the C-parity transformation which relates the two sets of ten diagrams gives the following results. For the vector contribution, the sum of diagrams reads

$$\mathcal{M}_\rho^V = Q_1^2[(AB)_{123}]_{SS} \otimes f + Q_1 Q_2[(AB)_{45}]_{SS} \otimes f$$
$$+ Q_2^2[(AB)_{123}]_{SS}^{(C)} \otimes f + Q_1 Q_2[(AB)_{45}]_{SS}^{(C)} \otimes f,$$
$$(4.3)$$

while for the axial contribution, one gets

$$\mathcal{M}_\rho^A = Q_1^2[(AB)_{123}]_{SP} \otimes \tilde{f} + Q_1 Q_2[(AB)_{45}]_{SP} \otimes \tilde{f}$$
$$- Q_2^2[(AB)_{123}]_{SP}^{(C)} \otimes \tilde{f} - Q_1 Q_2[(AB)_{45}]_{SP}^{(C)} \otimes \tilde{f}.$$
$$(4.4)$$

In the above two formulas, f denotes a GPD of the set H, E appearing in the decomposition of the vector correlator (3.2), while $\tilde{f}$ denotes a GPD of the set $\tilde{H}, \tilde{E}$ appearing in the decomposition of the axial correlator (3.3).

---

[6]Note that the SS structure is equivalent to the PP structure that enters the amplitude for the charged pion [1] since the two γ^5 matrices can be combined through anticommutation relations. They are of course associated with different GPDs in each case.

The symbol $\otimes$ represents the integration over x. The integration over z for the ρ-meson DA is implicit, since the DA is symmetric over $z \leftrightarrow 1 - z$. The superscript (C) denotes $x \to -x$ and $z \to (1 - z)$.

The above decomposition is convenient since the integration over z is performed *analytically*, while the integration over x is performed *numerically*. This allows us to evaluate the amplitude in blocks which can be used for computing various observables. Equations (4.3) and (4.4) are obtained by making the identification

$$[(CD)_{345}]_{SP} = -[(AB)_{123}]_{SP}^{(C)}, \quad (4.5)$$

$$[(CD)_{12}]_{SP} = -[(AB)_{45}]_{SP}^{(C)}, \quad (4.6)$$

$$[(CD)_{345}]_{SS} = [(AB)_{123}]_{SS}^{(C)}, \quad (4.7)$$

$$[(CD)_{12}]_{SS} = [(AB)_{45}]_{SS}^{(C)}. \quad (4.8)$$

We introduce a few convenient notations. A superscript s (a) refers to the symmetric (antisymmetric) structures of the hard amplitude and of the GPD with respect to x, i.e.

$$f(x) = \frac{1}{2}(f(x) + f(-x)) + \frac{1}{2}(f(x) - f(-x))$$
$$= f^s(x) + f^a(x). \quad (4.9)$$

This thus leads to

$$\mathcal{M}_\rho^V = (Q_1^2 + Q_2^2)[(AB)_{123}]_{SS}^s \otimes f^s$$
$$+ (Q_1^2 - Q_2^2)[(AB)_{123}]_{SS}^a \otimes f^a$$
$$+ 2Q_1 Q_2[(AB)_{45}]_{SS}^s \otimes f^s, \quad (4.10)$$

for the vector GPD contribution, and

$$\mathcal{M}_\rho^A = (Q_1^2 + Q_2^2)[(AB)_{123}]_{SP}^a \otimes \tilde{f}^a$$
$$+ (Q_1^2 - Q_2^2)[(AB)_{123}]_{SP}^s \otimes \tilde{f}^s$$
$$+ 2Q_1 Q_2[(AB)_{45}]_{SP}^a \otimes \tilde{f}^a, \tag{4.11}$$

for the axial GPD contribution, i.e. *SP*. In the above formulas, $Q_1 = Q_u$ and $Q_2 = Q_d$ correspond to a ρ^+, $Q_1 = Q_d$ and $Q_2 = Q_u$ correspond to a ρ^-, and $Q_1 = Q_2 = Q_{u,d}$ corresponds to ρ^0.

In the case of ρ^0 meson production [13], which is $C(-)$, the exchange in the t channel is fixed to be $C(-)$. In Eq. (4.10), this implies that only the symmetric part of the vector GPD contributes, while in Eq. (4.11), only the antisymmetric part of the axial GPD contributes. On the other hand, ρ^+ production (and similarly for ρ^-) involves both C-parity exchanges in the t channel, which explains why both symmetrical and antisymmetrical parts of the GPDs are involved in Eqs. (4.10) and (4.11).

The detailed evaluation of one diagram was already illustrated in Ref. [14], and therefore, we do not repeat it here.

1. Tensor structure

For convenience, we introduce the common normalization coefficients[7]

$$C^\| = -\frac{4}{9} f_\rho^\| \alpha_{em} \alpha_s \pi^2. \tag{4.12}$$

Note that we include the charge factors Q_u and Q_d inside the hard matrix element, using the decompositions obtained in Eqs. (4.10) and (4.11).

For the *SS* sector, two tensor structures appear, namely

$$T_A = (\varepsilon_{q\perp} \cdot \varepsilon_{k\perp}^*),$$
$$T_B = (\varepsilon_{q\perp} \cdot p_\perp)(p_\perp \cdot \varepsilon_{k\perp}^*), \tag{4.13}$$

while for the *SP* sector, the two following structures appear:

$$T_{A_5} = (p_\perp \cdot \varepsilon_{k\perp}^*)\epsilon^{np\varepsilon_{q\perp}p_\perp},$$
$$T_{B_5} = -(p_\perp \cdot \varepsilon_{q\perp})\epsilon^{np\varepsilon_{k\perp}^* p_\perp}. \tag{4.14}$$

2. Organization of the chiral-even amplitude

The scattering amplitude of the process (1.1), in the factorized form, is expressed in terms of form factors $\mathcal{H}_\rho$, $\mathcal{E}_\rho$, $\tilde{\mathcal{H}}_\rho$, $\tilde{\mathcal{E}}_\rho$, analogous to Compton form factors in DVCS, and reads

$$\mathcal{M}_\rho^\| \equiv \frac{1}{n \cdot p} \bar{u}(p_2, \lambda_2)\left[\slashed{n}\mathcal{H}_\rho(\xi, t) + \frac{i\sigma^{n\alpha}\Delta_\alpha}{2m}\mathcal{E}_\rho(\xi, t)\right.$$
$$\left. + \slashed{n}\gamma^5\tilde{\mathcal{H}}_\rho(\xi, t) + \frac{n \cdot \Delta}{2m}\gamma^5\tilde{\mathcal{E}}_\rho(\xi, t)\right]u(p_1, \lambda_1). \tag{4.15}$$

We isolate the tensor structures of the form factors as

$$\mathcal{H}_\rho(\xi, t) = \mathcal{H}_{\rho A}(\xi, t)T_A + \mathcal{H}_{\rho B}(\xi, t)T_B,$$
$$\tilde{\mathcal{H}}_\rho(\xi, t) = \tilde{\mathcal{H}}_{\rho A_5}(\xi, t)T_{A_5} + \tilde{\mathcal{H}}_{\rho B_5}(\xi, t)T_{B_5}. \tag{4.16}$$

These coefficients can be expressed in terms of the sum over diagrams of the integral of the product of their traces, of GPDs and DAs, as defined and given explicitly in Appendix C of Ref. [1] for the case of the holographic DA, and Appendix D of Ref. [14] for the asymptotic DA case. We introduce dimensionless coefficients N and $\tilde{N}$ as follows:

$$\mathcal{H}_{\rho A} = \frac{1}{s}C^\| N_{\rho A}, \qquad \mathcal{H}_{\rho B} = \frac{1}{s^2}C^\| N_{\rho B}, \tag{4.17}$$

and

$$\tilde{\mathcal{H}}_{\rho A_5} = \frac{1}{s^3}C^\| \tilde{N}_{\rho A_5}, \qquad \tilde{\mathcal{H}}_{\rho B_5} = \frac{1}{s^3}C^\| \tilde{N}_{\rho B_5}, \tag{4.18}$$

In order to emphasize the gauge-invariant structure and to organize the numerical study, we factorize out the charge coefficients, and put an explicit index q for the flavor of the quark GPDs f^q and $\tilde{f}^q$. In accordance with the decompositions (4.10) and (4.11) we thus introduce[8]

$$N_{\rho A}^q(Q_1, Q_2) = (Q_1^2 + Q_2^2)N_A^q[(AB)_{123}]^s + (Q_1^2 - Q_2^2)N_A^q[(AB)_{123}]^a + 2Q_1 Q_2 N_A^q[(AB)_{45}]^s, \tag{4.19}$$

$$N_{\rho B}^q(Q_1, Q_2) = (Q_1^2 + Q_2^2)N_B^q[(AB)_{123}]^s + (Q_1^2 - Q_2^2)N_B^q[(AB)_{123}]^a + 2Q_1 Q_2 N_B^q[(AB)_{45}]^s, \tag{4.20}$$

and

$$\tilde{N}_{\rho A_5}^q(Q_1, Q_2) = (Q_1^2 + Q_2^2)\tilde{N}_{A_5}^q[(AB)_{123}]^a + (Q_1^2 - Q_2^2)\tilde{N}_{A_5}^q[(AB)_{123}]^s + 2Q_1 Q_2 \tilde{N}_{A_5}^q[(AB)_{45}]^a, \tag{4.21}$$

$$\tilde{N}_{\rho B_5}^q(Q_1, Q_2) = (Q_1^2 + Q_2^2)\tilde{N}_{B_5}^q[(AB)_{123}]^a + (Q_1^2 - Q_2^2)\tilde{N}_{B_5}^q[(AB)_{123}]^s + 2Q_1 Q_2 \tilde{N}_{B_5}^q[(AB)_{45}]^a. \tag{4.22}$$

---

[7]Note that the sign has been corrected here with respect to our previous publication [13]. We note however that this does not affect the cross section, which corresponds to the square of the amplitude and is therefore insensitive to the sign.

[8]Effectively, what changes here for the ρ-meson case from the pion case is that the association of the coefficients in Eqs. (4.21) to (4.20) to the GPDs is swapped, i.e. vector for axial and vice versa. This explains why the tildes are swapped with respect to the pion case.

The above four terms, which have a superscript "q," are not to be confused with the coefficients that appear in Eqs. (4.17) and (4.18). Instead, the four terms are used in Eqs. (4.23)–(4.30) below to construct the coefficients.

For the specific case of our four processes, namely $\gamma\rho^0$ production on a proton (denoted by ρ_p^0), $\gamma\rho^0$ production on a neutron (denoted by ρ_n^0), $\gamma\rho^+$ production on a proton and $\gamma\rho^-$ production on a neutron, taking into account the structure (3.1) of the transition GPD structure we thus need to compute the coefficients

$$N_{\rho_p^0 A} = \frac{1}{\sqrt{2}}[N_{\rho A}^u(Q_u, Q_u) - N_{\rho A}^d(Q_d, Q_d)],$$

$$N_{\rho_p^0 B} = \frac{1}{\sqrt{2}}[N_{\rho B}^u(Q_u, Q_u) - N_{\rho B}^d(Q_d, Q_d)], \qquad (4.23)$$

$$N_{\rho_n^0 A} = \frac{1}{\sqrt{2}}[N_{\rho A}^u(Q_d, Q_d) - N_{\rho A}^d(Q_u, Q_u)],$$

$$N_{\rho_n^0 B} = \frac{1}{\sqrt{2}}[N_{\rho B}^u(Q_d, Q_d) - N_{\rho B}^d(Q_u, Q_u)], \qquad (4.24)$$

$$N_{\rho^+ A} = N_{\rho A}^u(Q_u, Q_d) - N_{\rho A}^d(Q_u, Q_d),$$
$$N_{\rho^+ B} = N_{\rho B}^u(Q_u, Q_d) - N_{\rho B}^d(Q_u, Q_d), \qquad (4.25)$$

$$N_{\rho^- A} = N_{\rho A}^u(Q_d, Q_u) - N_{\rho A}^d(Q_d, Q_u),$$
$$N_{\rho^- B} = N_{\rho B}^u(Q_d, Q_u) - N_{\rho B}^d(Q_d, Q_u), \qquad (4.26)$$

corresponding to the case with vector GPDs, as well as

$$\tilde{N}_{\rho_p^0 A_5} = \frac{1}{\sqrt{2}}[\tilde{N}_{\rho A_5}^u(Q_u, Q_u) - \tilde{N}_{\rho A_5}^d(Q_d, Q_d)],$$

$$\tilde{N}_{\rho_p^0 B_5} = \frac{1}{\sqrt{2}}[\tilde{N}_{\rho B_5}^u(Q_u, Q_u) - \tilde{N}_{\rho B_5}^d(Q_d, Q_d)], \qquad (4.27)$$

$$\tilde{N}_{\rho_n^0 A_5} = \frac{1}{\sqrt{2}}[\tilde{N}_{\rho A_5}^u(Q_d, Q_d) - \tilde{N}_{\rho A_5}^d(Q_u, Q_u)],$$

$$\tilde{N}_{\rho_n^0 B_5} = \frac{1}{\sqrt{2}}[\tilde{N}_{\rho B_5}^u(Q_d, Q_d) - \tilde{N}_{\rho B_5}^d(Q_u, Q_u)], \qquad (4.28)$$

$$\tilde{N}_{\rho^+ A_5} = \tilde{N}_{\rho A_5}^u(Q_u, Q_d) - \tilde{N}_{\rho A_5}^d(Q_u, Q_d),$$
$$\tilde{N}_{\rho^+ B_5} = \tilde{N}_{\rho B_5}^u(Q_u, Q_d) - \tilde{N}_{\rho B_5}^d(Q_u, Q_d), \qquad (4.29)$$

$$\tilde{N}_{\rho^- A_5} = \tilde{N}_{\rho A_5}^u(Q_d, Q_u) - \tilde{N}_{\rho A_5}^d(Q_d, Q_u),$$
$$\tilde{N}_{\rho^- B_5} = \tilde{N}_{\rho B_5}^u(Q_d, Q_u) - \tilde{N}_{\rho B_5}^d(Q_d, Q_u), \qquad (4.30)$$

which correspond to the case of axial GPDs. Therefore, for each flavor u and d, by knowing the 12 numerical coefficients

$$\tilde{N}_{A_5}^q[(AB)_{123}]^s, \quad \tilde{N}_{A_5}^q[(AB)_{123}]^a, \quad \tilde{N}_{A_5}^q[(AB)_{45}]^a,$$
$$\tilde{N}_{B_5}^q[(AB)_{123}]^s, \quad \tilde{N}_{B_5}^q[(AB)_{123}]^a, \quad \tilde{N}_{B_5}^q[(AB)_{45}]^a,$$
$$N_A^q[(AB)_{123}]^s, \quad N_A^q[(AB)_{123}]^a, \quad N_A^q[(AB)_{45}]^s,$$
$$N_B^q[(AB)_{123}]^s, \quad N_B^q[(AB)_{123}]^a, \quad N_B^q[(AB)_{45}]^s, \qquad (4.31)$$

for two given GPDs f and $\tilde{f}$ (in practice H and $\tilde{H}$; see next subsection), one can reconstruct the scattering amplitudes of the two processes. These 12 coefficients can be expanded in terms of five building block integrals which we label as I_b, I_c, I_h, I_i and I_e for the asymptotic DA case, and two extra building blocks labeled as χ_b, χ_c for the case of the holographic DA. The building block integrals can be found in Appendix C of Ref. [1], and in Appendix D of Ref. [14].

3. Cross section

In the forward limit $\Delta_\perp = 0 = P_\perp$, one can show that the square of the $\mathcal{M}_\rho^\parallel$ from Eq. (4.15) reads, after summing over nucleon helicities

$$\mathcal{M}_\rho^\parallel \mathcal{M}_\rho^{\parallel*} \equiv \sum_{\lambda_2, \lambda_1} \mathcal{M}_\rho^\parallel(\lambda_1, \lambda_2) \mathcal{M}_\rho^{\parallel*}(\lambda_1, \lambda_2)$$

$$= 8(1 - \xi^2)(\mathcal{H}_\rho(\xi, t)\mathcal{H}_\rho^*(\xi, t) + \tilde{\mathcal{H}}_\rho(\xi, t)\tilde{\mathcal{H}}_\rho^*(\xi, t)) + 8\frac{\xi^4}{1 - \xi^2}(\mathcal{E}_\rho(\xi, t)\mathcal{E}_\rho^*(\xi, t) + \tilde{\mathcal{E}}_\rho(\xi, t)\tilde{\mathcal{E}}_\rho^*(\xi, t))$$

$$- 8\xi^2(\mathcal{H}_\rho(\xi, t)\mathcal{E}_\rho^*(\xi, t) + \mathcal{H}_\rho^*(\xi, t)\mathcal{E}_\rho(\xi, t) + \tilde{\mathcal{H}}_\rho(\xi, t)\tilde{\mathcal{E}}_\rho^*(\xi, t) + \tilde{\mathcal{H}}_\rho^*(\xi, t)\tilde{\mathcal{E}}_\rho(\xi, t)). \qquad (4.32)$$

For moderately small values of ξ, this becomes

$$\mathcal{M}_\rho^\parallel \mathcal{M}_\rho^{\parallel*} \simeq 8(\mathcal{H}_\rho(\xi, t)\mathcal{H}_\rho^*(\xi, t) + \tilde{\mathcal{H}}_\rho(\xi, t)\tilde{\mathcal{H}}_\rho^*(\xi, t)). \qquad (4.33)$$

Hence we will restrict ourselves to the GPDs H, $\tilde{H}$ to perform our estimates of the cross section.[9] We note that this approximation remains valid for the linear polarization asymmetry with respect to the incoming photon, as the above equation still contains the helicities of the incoming and outgoing photons.

---

[9]In practice, we keep the first term on the rhs of Eq. (4.32), i.e. including the $(1 - \xi^2)$ prefactor.

We now perform the sum/averaging over the polarizations of the incoming and outgoing photons,

$$|\mathcal{H}_\rho(\xi,t)|^2 \equiv \sum_{\lambda_k,\lambda_q} \mathcal{H}_\rho(\xi,t,\lambda_k,\lambda_q)\mathcal{H}_\rho(\xi,t,\lambda_k,\lambda_q)$$

$$= 2|\mathcal{H}_{\rho A}(\xi,t)|^2 + p_\perp^4|\mathcal{H}_{\rho B}(\xi,t)|^2$$
$$+ p_\perp^2[\mathcal{H}_{\rho A}(\xi,t)\mathcal{H}_{\rho B}^*(\xi,t) + \mathcal{H}_{\rho A}^*(\xi,t)\mathcal{H}_{\rho B}(\xi,t)],$$
$$(4.34)$$

$$|\tilde{\mathcal{H}}_\rho(\xi,t)|^2 \equiv \sum_{\lambda_k,\lambda_q} \tilde{\mathcal{H}}_\rho(\xi,t,\lambda_k,\lambda_q)\tilde{\mathcal{H}}_\rho^*(\xi,t,\lambda_k,\lambda_q)$$

$$= \frac{s^2 p_\perp^4}{4}(|\tilde{\mathcal{H}}_{\rho A_5}(\xi,t)|^2 + |\tilde{\mathcal{H}}_{\rho B_5}(\xi,t)|^2). \quad (4.35)$$

Finally, we define the averaged amplitude squared $|\overline{\mathcal{M}}_\rho^\parallel|^2$, which includes the factor $1/4$ coming from the averaging over the polarizations of the initial particles. Collecting all prefactors, which read

$$\frac{1}{s^2}8(1-\xi^2)|C^\parallel|^2\frac{1}{2^2}, \quad (4.36)$$

we have that

$$|\overline{\mathcal{M}}_\rho^\parallel|^2 = \frac{2}{s^2}(1-\xi^2)|C^\parallel|^2\left\{2|N_{\rho A}|^2 + \frac{p_\perp^4}{s^2}|N_{\rho B}|^2\right.$$
$$\left. + \frac{p_\perp^2}{s}(N_{\rho A}N_{\rho B}^* + \text{c.c.}) + \frac{p_\perp^4}{4s^2}|\tilde{N}_{\rho A_5}|^2 + \frac{p_\perp^4}{4s^2}|\tilde{N}_{\rho B_5}|^2\right\}.$$
$$(4.37)$$

Here ρ corresponds to ρ_p^0, ρ_n^0, ρ_p^+ or ρ_n^-, where the subscript denotes the target. The corresponding coefficients $N_{\rho A}$, $N_{\rho B}$, $\tilde{N}_{\rho A_5}$, $\tilde{N}_{\rho B_5}$ are given by Eqs. (4.23)–(4.30).

The differential cross section as a function of t, $M_{\gamma\rho}^2$, $-u'$ then reads

$$\frac{d\sigma^\parallel}{dtdu'dM_{\gamma\rho}^2}\Bigg|_{-t=(-t)_{\min}} = \frac{|\overline{\mathcal{M}}_\rho^\parallel|^2}{32S_{\gamma N}^2 M_{\gamma\rho}^2(2\pi)^3}. \quad (4.38)$$

C. Chiral-odd case

As before, one can group diagrams based on their charges. Using the same notations as in Sec. IV B, exploiting the C-parity symmetry of the process, one obtains

$$\mathcal{M}_\rho^\perp = Q_1^2[(AB)_{123}]_{TT} \otimes f_T + Q_1Q_2[(AB)_{45}]_{TT} \otimes f_T$$
$$+ Q_2^2[(AB)_{123}]_{TT}^{(C)} \otimes f_T + Q_1Q_2[(AB)_{45}]_{TT}^{(C)} \otimes f_T,$$
$$(4.39)$$

where

$$[(CD)_{345}]_{TT} = [(AB)_{123}]_{TT}^{(C)}, \quad (4.40)$$

$$[(CD)_{12}]_{TT} = [(AB)_{45}]_{TT}^{(C)}, \quad (4.41)$$

have been used. In the above, f_T represents a generic "tensor" chiral-odd GPD (in practice, H_T). Only eight diagrams out of the 20 diagrams are nonvanishing in the chiral-odd case. They are A_3, B_1, A_4 and B_5, and the corresponding ones given by the symmetry transformation in Eqs. (4.40) and (4.41). Writing the GPDs in terms of symmetric and antisymmetric parts, we have

$$\mathcal{M}_\rho^\perp = (Q_1^2 + Q_2^2)[(AB)_{123}]_{TT}^s \otimes f_T^s$$
$$+ (Q_1^2 - Q_2^2)[(AB)_{123}]_{TT}^a \otimes f_T^a$$
$$+ 2Q_1Q_2[(AB)_{45}]_{TT}^s \otimes f_T^s. \quad (4.42)$$

The detailed evaluation of one diagram was performed in Ref. [13], and we do not repeat this here.

1. Tensor structure

It is convenient to introduce the common normalization factor[10]

$$C^\perp = \frac{4}{9}f_\rho^\perp\alpha_{em}\alpha_s\pi^2. \quad (4.43)$$

Note that we include the charge factors Q_u and Q_d inside the hard matrix element, using the decomposition obtained in Eq. (4.42).

In this case, two tensor structures appear, namely

$$T_{A\perp}^i = \frac{-8s}{\bar{\alpha}}\{\alpha\varepsilon_{k\perp}^{i*}[(p_\perp\cdot\varepsilon_{q\perp})(p_\perp\cdot\varepsilon_{\rho\perp}^*) + \alpha\bar{\alpha}\xi s(\varepsilon_{q\perp}\cdot\varepsilon_{\rho\perp}^*)] - \bar{\alpha}\varepsilon_{\rho\perp}^{i*}[\alpha(\alpha-2)\xi s(\varepsilon_{q\perp}\cdot\varepsilon_{k\perp}^*) - (p_\perp\cdot\varepsilon_{q\perp})(p_\perp\cdot\varepsilon_{k\perp}^*)]$$
$$+ p_\perp^i[(p_\perp\cdot\varepsilon_{\rho\perp}^*)(\varepsilon_{q\perp}\cdot\varepsilon_{k\perp}^*) - \bar{\alpha}(\varepsilon_{k\perp}^*\cdot\varepsilon_{\rho\perp}^*)(p_\perp\cdot\varepsilon_{q\perp})] + \varepsilon_{q\perp}^i[-(p_\perp\cdot\varepsilon_{\rho\perp}^*)(p_\perp\cdot\varepsilon_{k\perp}^*) + \alpha\bar{\alpha}(\alpha-2)\xi s(\varepsilon_{k\perp}^*\cdot\varepsilon_{\rho\perp}^*)]\}, \quad (4.44)$$

$$T_{B\perp}^i = \frac{8s}{\alpha\bar{\alpha}}\{\bar{\alpha}\varepsilon_{\rho\perp}^{i*}[(p_\perp\cdot\varepsilon_{q\perp})(p_\perp\cdot\varepsilon_{k\perp}^*) - \alpha(2\alpha-1)\xi s(\varepsilon_{q\perp}\cdot\varepsilon_{k\perp}^*)] + \alpha\varepsilon_{k\perp}^{i*}[\bar{\alpha}(2\alpha-1)\xi s(\varepsilon_{q\perp}\cdot\varepsilon_{\rho\perp}^*) + (p_\perp\cdot\varepsilon_{q\perp})(p_\perp\cdot\varepsilon_{\rho\perp}^*)]$$
$$+ \varepsilon_{q\perp}^i[-(p_\perp\cdot\varepsilon_{\rho\perp}^*)(p_\perp\cdot\varepsilon_{k\perp}^*) - \alpha\bar{\alpha}\xi s(\varepsilon_{k\perp}^*\cdot\varepsilon_{\rho\perp}^*)] + p_\perp^i[-\alpha(p_\perp\cdot\varepsilon_{\rho\perp}^*)(\varepsilon_{q\perp}\cdot\varepsilon_{k\perp}^*) - \bar{\alpha}(\varepsilon_{q\perp}\cdot\varepsilon_{\rho\perp}^*)(p_\perp\cdot\varepsilon_{k\perp}^*)]\}. \quad (4.45)$$

---

[10]Note that the sign has been corrected here with respect to our previous publication [13]. We note however that this does not affect the cross section, which corresponds to the square of the amplitude and is therefore insensitive to the sign.

When summing over the polarizations $\varepsilon_{\rho\perp}$ of the ρ meson in order to compute the square of the amplitude, only

$$\sum_T \varepsilon_{\rho\perp}^\mu \varepsilon_{\rho\perp}^{\nu*} = -g_\perp^{\mu\nu}, \qquad (4.46)$$

is needed, since we have chosen the basis as defined in Sec. II.

$$\mathcal{M}_\rho^\perp \equiv \frac{1}{n \cdot p} \bar{u}(p_2, \lambda_2) \left[i\sigma^{nj} \mathcal{H}_{T\rho j}(\xi, t) + \frac{P \cdot n\Delta^j - \Delta \cdot nP^j}{m^2} \tilde{\mathcal{H}}_{T\rho j}(\xi, t) \right.$$
$$\left. + \frac{\gamma \cdot n\Delta^j - \Delta \cdot n\gamma^j}{2m} \mathcal{E}_{T\rho j}(\xi, t) + \frac{\gamma \cdot nP^j - P \cdot n\gamma^j}{m} \tilde{\mathcal{E}}_{T\rho j}(\xi, t) \right] u(p_1, \lambda_1), \qquad (4.47)$$

where j corresponds to a transverse vector index. From the form factors, one can isolate the following tensor structures:

$$\mathcal{H}_T^j(\xi, t) = \mathcal{H}_{T\rho A}(\xi, t) T_{A\perp}^j + \mathcal{H}_{T\rho B}(\xi, t) T_{B\perp}^j. \qquad (4.48)$$

We further express the above coefficients in terms of dimensionless ones through

$$\mathcal{H}_{T\rho A} = \frac{1}{s^3} C^\perp N_{T\rho A}, \qquad (4.49)$$

$$\mathcal{H}_{T\rho B} = \frac{1}{s^3} C^\perp N_{T\rho B}. \qquad (4.50)$$

Proceeding as in Sec. IV B 2, the electric charges are factorized, and we introduce an explicit index q to denote the flavor of the quark GPDs f_T^q and $\tilde{f}_T^q$. Thus, using the decomposition in Eq. (4.42), we have that

$$N_{T\rho A}^q(Q_1, Q_2) = (Q_1^2 + Q_2^2) N_{TA}^q [(AB)_{123}]^s$$
$$+ (Q_1^2 - Q_2^2) N_{TA}^q [(AB)_{123}]^a$$
$$+ 2Q_1 Q_2 N_{TA}^q [(AB)_{45}]^s, \qquad (4.51)$$

$$N_{T\rho B}^q(Q_1, Q_2) = (Q_1^2 + Q_2^2) N_{TB}^q [(AB)_{123}]^s$$
$$+ (Q_1^2 - Q_2^2) N_{TB}^q [(AB)_{123}]^a$$
$$+ 2Q_1 Q_2 N_{TB}^q [(AB)_{45}]^s. \qquad (4.52)$$

Just like in the chiral-even case, the above two terms, which have a superscript "q," are not to be confused with the coefficients that appear in Eq. (4.49). Instead, the two terms are used in Eqs. (4.53)–(4.56) below to construct the coefficients.

For the specific case of our four processes, namely $\gamma\rho^0$ production on a proton (denoted by ρ_p^0), $\gamma\rho^0$ production on a neutron (denoted by ρ_n^0), $\gamma\rho^+$ production on a proton and $\gamma\rho^-$ production on a neutron, taking into account the structure (3.1) of the transition GPD structure, we find that the following coefficients need to be computed:

2. Organization of the chiral-odd amplitude

Following the same steps as the chiral-even case, we can write the chiral-odd amplitude in terms of form factors $\mathcal{H}_{T\rho}^j, \tilde{\mathcal{H}}_{T\rho}^j, \mathcal{E}_{T\rho}^j, \tilde{\mathcal{E}}_{T\rho}^j$, analogous to Compton form factors in Deeply Virtual Compton Scattering (DVCS),

$$N_{T\rho_p^0 A} = \frac{1}{\sqrt{2}} [N_{T\rho A}^u(Q_u, Q_u) - N_{T\rho A}^d(Q_d, Q_d)],$$

$$N_{T\rho_p^0 B} = \frac{1}{\sqrt{2}} [N_{T\rho B}^u(Q_u, Q_u) - N_{T\rho B}^d(Q_d, Q_d)], \qquad (4.53)$$

$$N_{T\rho_n^0 A} = \frac{1}{\sqrt{2}} [N_{T\rho A}^u(Q_d, Q_d) - N_{T\rho A}^d(Q_u, Q_u)],$$

$$N_{T\rho_n^0 B} = \frac{1}{\sqrt{2}} [N_{T\rho B}^u(Q_d, Q_d) - N_{T\rho B}^d(Q_u, Q_u)], \qquad (4.54)$$

$$N_{T\rho^+ A} = N_{T\rho A}^u(Q_u, Q_d) - N_{T\rho A}^d(Q_u, Q_d),$$
$$N_{T\rho^+ B} = N_{T\rho B}^u(Q_u, Q_d) - N_{T\rho B}^d(Q_u, Q_d), \qquad (4.55)$$

$$N_{T\rho^- A} = N_{T\rho A}^u(Q_d, Q_u) - N_{T\rho A}^d(Q_d, Q_u),$$
$$N_{T\rho^- B} = N_{T\rho B}^u(Q_d, Q_u) - N_{T\rho B}^d(Q_d, Q_u). \qquad (4.56)$$

In practice, we deduce that the following six numerical coefficients need to be computed, for each flavor u and d,

$$N_{TA}^q[(AB)_{123}]^s, \quad N_{TA}^q[(AB)_{123}]^a, \quad N_{TA}^q[(AB)_{45}]^s,$$
$$N_{TB}^q[(AB)_{123}]^s, \quad N_{TB}^q[(AB)_{123}]^a, \quad N_{TB}^q[(AB)_{45}]^s, \qquad (4.57)$$

for a given chiral-odd GPD f_T (in practice, H_T). This is sufficient to reconstruct the amplitude for all four processes we are interested in. The six coefficients can be expressed in terms of three building block integrals, which we label as I_e, I_i and I_d for the asymptotic DA case, and one extra building block integral labeled χ_a for the case of the holographic DA. The expressions for the coefficients in Eq. (4.57) in terms of the building block integrals are given in Appendix A.

3. Cross section

In the forward limit $\Delta_\perp = 0 = P_\perp$, one can show that the square of $\mathcal{M}_\perp$ in Eq. (4.47) reads, after summing over nucleon helicities,

$$\mathcal{M}_\rho^\perp \mathcal{M}_\rho^{\perp*} \equiv \sum_{\lambda_1,\lambda_2} \mathcal{M}_\rho^\perp(\lambda_1,\lambda_2)\mathcal{M}_\rho^{\perp*}(\lambda_1,\lambda_2)$$

$$= 8\Big[-(1-\xi^2)\mathcal{H}_{T\rho}^i(\xi,t)\mathcal{H}_{T\rho}^{j*}(\xi,t) - \frac{\xi^2}{1-\xi^2}[\xi\mathcal{E}_{T\rho}^i(\xi,t) - \tilde{\mathcal{E}}_{T\rho}^i(\xi,t)][\xi\mathcal{E}_{T\rho}^{j*}(\xi,t) - \tilde{\mathcal{E}}_{T\rho}^{j*}(\xi,t)]$$

$$+ \xi\{\mathcal{H}_{T\rho}^i(\xi,t)[\xi\mathcal{E}_{T\rho}^j(\xi,t) - \tilde{\mathcal{E}}_{T\rho}^j(\xi,t)]^* + \mathcal{H}_{T\rho}^{i*}(\xi,t)[\xi\mathcal{E}_{T\rho}^j(\xi,t) - \tilde{\mathcal{E}}_{T\rho}^j(\xi,t)]\}\Big]g_{\perp ij}. \qquad (4.58)$$

For moderately small values of ξ, it reduces to

$$\mathcal{M}_\rho^\perp \mathcal{M}_\rho^{\perp*} = -8\mathcal{H}_{T\rho}^i(\xi,t)\mathcal{H}_{T\rho}^{j*}(\xi,t)g_{\perp ij}. \qquad (4.59)$$

Hence, we will restrict ourselves to $H_{T\rho}$ to perform our estimates of the cross section.[11] Performing the sum over the transverse polarizations of the ρ meson, and the incoming and outgoing photons, one obtains

$$-g_{\perp ij}\sum_{\lambda_k\lambda_q\lambda_\rho} \mathcal{H}_{T\rho}^i(\xi,t,\lambda_k,\lambda_q,\lambda_\rho)\mathcal{H}_{T\rho}^{j*}(\xi,t,\lambda_k,\lambda_q,\lambda_\rho)$$

$$= 512\xi^2 s^4(\alpha^4|\mathcal{H}_{T\rho A}(\xi,t)|^2 + |\mathcal{H}_{T\rho B}(\xi,t)|^2). \qquad (4.60)$$

We can now compute the averaged amplitude squared $|\overline{\mathcal{M}}_\rho^\perp|^2$, which includes a factor of $1/4$ coming from the averaging of the polarizations of the incoming particles. Collecting all prefactors,

$$512\xi^2 s^4 \times \frac{1}{s^6}|C^\perp|^2 \times \frac{1}{4} \times 8(1-\xi^2), \qquad (4.61)$$

we have that

$$|\overline{\mathcal{M}}_\rho^\perp|^2 = \frac{1024}{s^2}\xi^2(1-\xi^2)|C^\perp|^2[\alpha^4|N_{T\rho A}(\xi,t)|^2$$

$$+ |N_{T\rho B}(\xi,t)|^2]. \qquad (4.62)$$

Here ρ corresponds to ρ_p^0, ρ_n^0, ρ_p^+ or ρ_n^-, where the subscript denotes the target. The corresponding coefficients $N_{T\rho A}$ and $N_{T\rho B}$ are given by Eqs. (4.53)–(4.56).

As for the longitudinally polarized ρ-meson case, the differential cross section as a function of $(-t)$, $M_{\gamma\rho}^2$, $(-u')$ then reads

$$\frac{d\sigma^\perp}{d(-t)d(-u')dM_{\gamma\rho}^2}\Big|_{-t=(-t)_{\min}} = \frac{|\overline{\mathcal{M}}_\rho^\perp|^2}{32S_{\gamma N}^2 M_{\gamma\rho}^2(2\pi)^3}. \qquad (4.63)$$

D. Polarization asymmetry

1. Chiral-even case

In the chiral-even case, as discussed in Appendix C, the circular polarization asymmetry vanishes as a result of conservation of parity P for an unpolarized target, which is the case we consider here.[12] Therefore, we compute the *linear* polarization asymmetry (LPA) with respect to the incoming photon, which is defined by

$$\text{LPA} = \frac{\int d\sigma_x - \int d\sigma_y}{\int d\sigma_x + \int d\sigma_y}, \qquad (4.64)$$

where $d\sigma_{x(y)}$ corresponds to the differential cross section with the incoming photon linearly polarized along the $x(y)$ direction. The integral symbol in Eq. (4.64) corresponds to phase space integration and hence, the LPA can be calculated at the fully differential (by dropping the integral altogether), single differential or integrated level.

The LPA is usually calculated in the lab frame, which corresponds to fixing the directions of the polarization vectors. However, for convenience in performing the computation, we first take the polarization vector in the x direction to be along $p_\perp$, which changes on an event-by-event basis. Then, the polarization vector in the y direction is chosen such that the x, y, z directions form a right-handed basis. Thus,

$$\varepsilon_x^\mu(q) \equiv \frac{p_\perp^\mu}{|\vec{p}_t|}, \qquad (4.65)$$

$$\varepsilon_y^\mu(q) \equiv -\frac{2}{s|\vec{p}_t|}\epsilon^{pnp_\perp\mu}. \qquad (4.66)$$

The LPA corresponding to this choice of polarization vectors is denoted by $\text{LPA}_{\max}$, since the directions of the polarization vectors are such that the LPA is maximized. The LPA in the lab frame, LPA_{Lab}, can then be related to $\text{LPA}_{\max}$ via a simple modulation of $\cos 2\theta$, where θ corresponds to the angle between $p_\perp$ and the x direction defined by the lab frame. Thus,

$$\text{LPA}_{\text{Lab}} = \text{LPA}_{\max}\cos 2\theta. \qquad (4.67)$$

---

[11]In practice, we keep the first term on the rhs of Eq. (4.58).

[12]The circular double spin asymmetry does not vanish and may be an interesting observable for a polarized target experiment.

The proof of this result, including the derivation of relevant expressions for the LPA, can be found in Appendix F in Ref. [1]. When showing the results in Sec. V, we therefore choose to show plots for LPA$_{\text{max}}$, as the modification due to $\cos 2\theta$ is trivial.

We now turn to the calculation of LPA$_{\text{max}}$. Amplitudes corresponding to specific linear polarization states in Eqs. (4.65) and (4.66) can be defined as

$$\mathcal{M}_x = \varepsilon_x^\mu(q)\mathcal{M}_\mu, \qquad \mathcal{M}_y = \varepsilon_y^\mu(q)\mathcal{M}_\mu. \qquad (4.68)$$

For convenience, let us decompose the amplitude as [cf. Eqs. (4.13) to (4.16)]

$$\mathcal{M} = C_A T_A + C_B T_B + C_{A_5} T_{A_5} + C_{B_5} T_{B_5}, \qquad (4.69)$$

i.e. in terms of the tensor structures $T_A, T_B, T_{A_5}, T_{B_5}$ defined in Eqs. (4.13) and (4.14). We note that the coefficients of the tensor structures include the spinors of the nucleons, as well as Dirac matrices associated with the definition of the GPDs. More explicitly, using Eqs. (4.15) and (4.16),

$$C_A \equiv \frac{1}{n \cdot p}\bar{u}(p_2,\lambda_2)\slashed{n}u(p_1,\lambda_1)\mathcal{H}_{\rho A}(\xi,t), \qquad (4.70)$$

$$C_B \equiv \frac{1}{n \cdot p}\bar{u}(p_2,\lambda_2)\slashed{n}u(p_1,\lambda_1)\mathcal{H}_{\rho B}(\xi,t), \qquad (4.71)$$

$$C_{A_5} \equiv \frac{1}{n \cdot p}\bar{u}(p_2,\lambda_2)\slashed{n}\gamma^5 u(p_1,\lambda_1)\tilde{\mathcal{H}}_{\rho A_5}(\xi,t), \qquad (4.72)$$

$$C_{B_5} \equiv \frac{1}{n \cdot p}\bar{u}(p_2,\lambda_2)\slashed{n}\gamma^5 u(p_1,\lambda_1)\tilde{\mathcal{H}}_{\rho B_5}(\xi,t). \qquad (4.73)$$

By squaring the amplitude, and summing over the polarization λ_k of the outgoing photon, we obtain

$$\sum_{\lambda_k}|\mathcal{M}_x|^2 = |C_A|^2 + |\vec{p}_t|^4|C_B|^2 + \frac{s^2}{4}|\vec{p}_t|^4|C_{B_5}|^2$$
$$- 2|\vec{p}_t|^2\text{Re}(C_A^* C_B), \qquad (4.74)$$

$$\sum_{\lambda_k}|\mathcal{M}_y|^2 = |C_A|^2 + \frac{s^2}{4}|\vec{p}_t|^4|C_{A_5}|^2. \qquad (4.75)$$

From the above polarized amplitude squared, one can compute the LPA$_{\text{max}}$ at various levels (from fully differential to integrated).

2. Chiral-odd case

For the case of the transversely polarized ρ meson, we find, through a direct computation, that both the circular and linear polarization asymmetries *always* vanish in the limit of

$\Delta_\perp = 0$. This is the consequence of the fact that, after squaring the amplitude and summing/averaging over all polarizations except ε_q, one obtains, after setting $\Delta_\perp = 0$,

$$\sum_{\substack{\lambda_1\lambda_2,\\\lambda_k\lambda_\rho}}\mathcal{M}_\rho^\perp\mathcal{M}_\rho^{\perp*} = -\frac{512}{s^2}\xi^2(1-\xi^2)|C^\perp|^2[\alpha^4|N_{T\rho A}(\xi,t)|^2$$
$$+ |N_{T\rho B}(\xi,t)|^2](\varepsilon_q^* \cdot \varepsilon_q). \qquad (4.76)$$

First, we note that upon summing over the transverse polarizations of the incoming photon, one recovers the averaged amplitude squared in Eq. (4.62). Second, the term $(\varepsilon_q^* \cdot \varepsilon_q)$ is trivially -1, and thus can never give rise to any polarization asymmetry.

Comparing with the chiral-even case in Sec. IV D 1, we find that repeating the same steps leads to two types of terms, namely the same one that appears in Eq. (4.76) $(\varepsilon_q^* \cdot \varepsilon_q)$, and also $(\varepsilon_q^* \cdot p_\perp)(\varepsilon_q \cdot p_\perp)$. It is terms of the latter type that lead to linear polarization asymmetries. For instance, in Eqs. (4.74) and (4.75), we note that $|C_A|^2$ comes from terms of the first type [from the square of the tensor T_A after summing over the polarization of the outgoing photon; see Eq. (4.14)], and it is easy to see that $|C_A|^2$ indeed cancels in the computation of the LPA.

Before ending this section, we stress that the result in Eq. (4.76) is obtained by working in the limit of $\Delta_\perp = 0$. In general, for nonzero $\Delta_\perp$, the analogue of Eq. (4.76) contains all possible contractions involving ε_q, namely $(\varepsilon_q^* \cdot \varepsilon_q)$, $(\varepsilon_q^* \cdot p_\perp)(\varepsilon_q \cdot p_\perp)$, $(\varepsilon_q^* \cdot \Delta_\perp)(\varepsilon_q \cdot p_\perp)$, $(\varepsilon_q^* \cdot p_\perp)(\varepsilon_q \cdot \Delta_\perp)$ and $(\varepsilon_q^* \cdot \Delta_\perp)(\varepsilon_q \cdot \Delta_\perp)$, which gives rise to polarization asymmetries. On the other hand, the result depends on transversity GPDs other than H_T, whose contributions are beyond the scope of this work. We therefore postpone the analysis of polarization asymmetries for nonzero $\Delta_\perp$ for a future publication.

V. RESULTS

A. Conventions for plots

For consistency, we use the same conventions for the plots as in our previous study [1]. We typically include four cases, considering two models for the DA (asymptotic or holographic), and two GPD models (valence or standard scenario). The conventions used throughout this section are as follows:

(1) Solid line: asymptotic DA, valence scenario
(2) Dashed line: holographic DA, valence scenario
(3) Dotted line: asymptotic DA, standard scenario
(4) Dot-dashed line: holographic DA, standard scenario
Dashed lines imply the use of the holographic DA, while dotted lines imply the use of the standard scenario for the GPD.

We present results for JLab kinematics in Sec. V C, COMPASS kinematics in Sec. V D and EIC as well as LHC UPC kinematics in Sec. V E. In each subsection, we present results for fully differential cross sections first, then single-differential cross sections [i.e. integrated over $(-t)$ and $(-u')$], followed by integrated cross sections as a function of $S_{\gamma N}$, and finally the linear polarization asymmetries with respect to the incoming photon. Each figure has four plots, with:

(1) top left corresponding to $\gamma \rho^0$ photoproduction on proton target (denoted by ρ_p^0),

(2) top right to $\gamma \rho^0$ photoproduction on neutron target (denoted by ρ_n^0),

(3) bottom left to $\gamma \rho^+$ photoproduction on a proton target (denoted by ρ_p^+), and

(4) bottom right to $\gamma \rho^-$ photoproduction on a neutron target (denoted by ρ_n^-).

Finally, the figures are presented in such an order that the chiral-even case (longitudinally polarized ρ meson) always appears before the chiral-odd case (transversely polarized ρ meson). We note that since the polarization asymmetry is always vanishing for the chiral-odd case, only plots for the linear polarization asymmetry corresponding to the chiral-even case are shown. Furthermore, these correspond to LPA$_{\max}$; see Sec. IV D 1.

B. Description of the numerics

The GPDs are computed as tables in x, for different ξ. For the amplitudes, we compute tables at different $(-u')$ and $M_{\gamma\rho}^2$, at a particular value of $S_{\gamma N}$. To compute the fully differential cross section (and hence amplitudes), $(-t)$ is fixed to its minimum value $(-t)_{\min}$; see Eq. (4.38). The t dependence of the cross section is then modeled by a simplistic ansatz, namely a factorized dipole form

$$F_H(t) = \frac{(t_{\min} - C)^2}{(t - C)^2}, \qquad (5.1)$$

with $C = 0.71 \text{ GeV}^2$.

We compute the cross section covering the *full* phase space in the region $20 \text{ GeV}^2 < S_{\gamma N} < 20\,000 \text{ GeV}^2$, since this covers the full kinematical range of JLab, COMPASS, EIC, and most of the relevant kinematical range for UPCs at the LHC; see Sec. V F 4. We compute seven sets of amplitude tables in total:

(1) $S_{\gamma N} = 20 \text{ GeV}^2$, $2.1 \leq M_{\gamma\rho}^2 \leq 10 \text{ GeV}^2$ with a uniform step of 0.1 GeV^2

(2) $S_{\gamma N} = 200 \text{ GeV}^2$, $2.1 \leq M_{\gamma\rho}^2 \leq 51.4 \text{ GeV}^2$ with a uniform step of 0.2 GeV^2

(3) $S_{\gamma N} = 200 \text{ GeV}^2$, $2.1 \leq M_{\gamma\rho}^2 \leq 110.5 \text{ GeV}^2$ with a uniform step of 1.1 GeV^2

(4) $S_{\gamma N} = 2000 \text{ GeV}^2$, $2.1 \leq M_{\gamma\rho}^2 \leq 51.4 \text{ GeV}^2$ with a uniform step of 0.2 GeV^2

(5) $S_{\gamma N} = 2000 \text{ GeV}^2$, $2.1 \leq M_{\gamma\rho}^2 \leq 1041.1 \text{ GeV}^2$ with a uniform step of 10.5 GeV^2

(6) $S_{\gamma N} = 20000 \text{ GeV}^2$, $2.1 \leq M_{\gamma\rho}^2 \leq 51.4 \text{ GeV}^2$ with a uniform step of 0.2 GeV^2

(7) $S_{\gamma N} = 20000 \text{ GeV}^2$, $2.1 \leq M_{\gamma\rho}^2 \leq 10396.6 \text{ GeV}^2$ with a uniform step of 105 GeV^2

The first, third, fifth and seventh sets cover the full range of the phase space, while the second, fourth and sixth sets are needed to resolve the peak in $M_{\gamma\rho}^2$ (importance sampling), like for the charged pion case [1]. This is particularly important for the chiral-even case, i.e. for the longitudinally polarized ρ meson.

For each amplitude table, the whole range of $(-u')$ is covered. More details regarding the boundaries of the kinematic variables can be found in Appendix E of Ref. [1], and in Appendix E of Ref. [14]. At each value of $S_{\gamma N} = 200, 2000, 20\,000 \text{ GeV}^2$, two separate data sets were needed: one to cover the whole range of the phase space, and the other to ensure that peaks in the distribution of $M_{\gamma\rho}^2$ were well resolved in the chiral-even case. This is not needed for the $S_{\gamma N} = 20 \text{ GeV}^2$ case, as the peak is moderate in that case. We refer to Sec. V. 2. 1 in Ref. [1] for details regarding the importance sampling procedure.

In practice, we compute amplitude tables in $(-u')$ for each of value of $M_{\gamma\rho}^2$. The steps we take are as follows:

(1) We calculate, for each of the above types of GPDs (in the present paper H, $\tilde{H}$ and H_T), sets of u and d quarks GPDs indexed by $M_{\gamma\rho}^2$, i.e. ultimately by ξ given by

$$\xi = \frac{M_{\gamma\rho}^2}{2(S_{\gamma N} - M^2) - M_{\gamma\rho}^2}. \qquad (5.2)$$

The GPDs are computed as tables of 1000 values for x ranging from -1 to 1, unless importance sampling is needed, in which case 1000 more values around the peak are added; see Sec. V. 2. 1 in Ref. [1].

(2) We compute the building block integrals which do not depend on $-u'$. In the asymptotic DA case, this corresponds to I_e (see Appendix D in Ref. [14] for the notation), while in the holographic DA case, this corresponds to both I_e and χ_c; see Appendix C of Ref. [1].

(3) We choose 100 values of $(-u')$, linearly varying from $(-u')_{\min} = 1 \text{ GeV}^2$ up to its maximum possible value $(-u')_{\max\text{Max}}$ (see Appendix E in Ref. [14] for how this is computed). Again, if importance sampling is needed (when the cross section varies rapidly at the boundaries), an extra set of 100 values of $(-u')$ is added at each boundary.

(4) At each value of $(-u')$, we compute, for each GPD and each flavor u and d, the remaining building block integrals, which are I_b, I_c, I_d, I_h, I_i in the
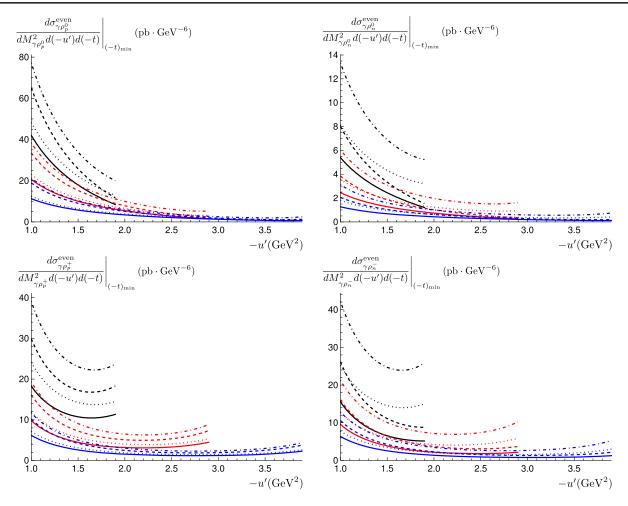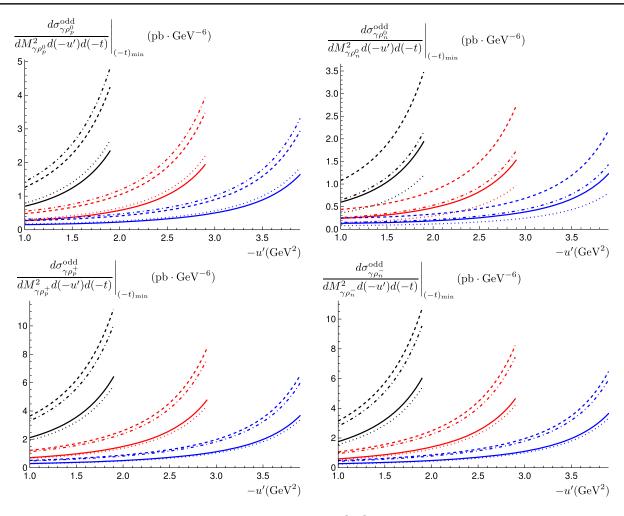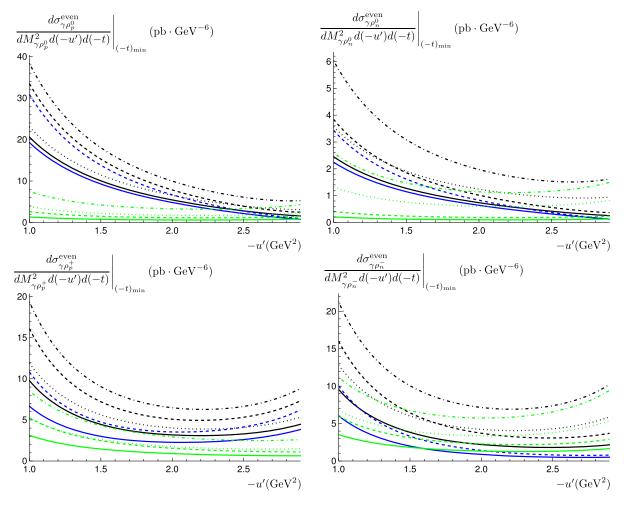
FIG. 2.   The fully differential cross section for longitudinally polarized $\rho_p^0, \rho_n^0, \rho_p^+, \rho_n^-$ is shown as a function of $(-u')$ in the top left, top right, bottom left and bottom right plots respectively for different values of $M_{\gamma\rho}^2$. The black, red and blue curves correspond to $M_{\gamma\rho}^2 = 3, 4, 5$ GeV^2 respectively. The dashed (nondashed) lines correspond to the holographic (asymptotic) DA, while the dotted (nondotted) lines correspond to the standard (valence) scenario. $S_{\gamma N}$ is fixed at 20 GeV^2.

asymptotic DA case, and χ_a and χ_b in the holographic DA case.[13]

(5) This gives, for each of these couples of values of $(M_{\gamma\rho}^2, -u')$ and each flavor, a set of 12 coefficients listed in Eq. (4.31) for the CE case, and Eq. (4.57) for the CO case.

(6) One can then get the desired cross sections using Eqs. (4.38) (CE case) and (4.63) (CO case).

To optimize the computation, we use a mapping procedure, described in Sec. 5.2 of Ref. [1], which allows us to obtain amplitude tables corresponding to lower values of $S_{\gamma N}$ from a single table (which can correspond to any one of the seven sets of amplitude tables mentioned above). This allows for a significant decrease in computing time, from the order of months to only a few days.

C. JLab kinematics

The electron beam at JLab hits a fixed target consisting of protons and neutrons, at an energy of 12 GeV. The electron-nucleon center-of-mass energy, S_{eN}, is thus roughly 23 GeV^2. Therefore, for most of the plots in this section, we use $S_{\gamma N} = 20$ GeV^2 as a representative value for JLab kinematics. This allows us to probe GPDs for the range of skewnesses of $0.04 \leq \xi \leq 0.33$.

At this point, we would like to point out that a programming mistake, related to the sign of the interference term in the squared amplitude, cf. Eq. (4.37), was made in the previous publication [13]. Thus, the plots corresponding to the ρ^0-meson case are slightly different.

1. Fully differential cross section

The effect of different values of $M_{\gamma\rho}^2$ on the cross section is shown in Fig. 2 for the longitudinally polarized ρ-meson case. The values chosen for $M_{\gamma\rho}^2$ are 3, 4 and 5 GeV^2. As $M_{\gamma\rho}^2$ grows, the range of allowed $(-u')$ values increases.

---

[13]We note that the chiral-odd case requires the computation of the extra building blocks I_d and χ_a, which are not needed in the chiral-even case.

FIG. 3. The fully differential cross section for transversely polarized $\rho_p^0, \rho_n^0, \rho_p^+, \rho_n^-$ is shown as a function of $(-u')$ in the top left, top right, bottom left and bottom right plots respectively for different values of $M_{\gamma\rho}^2$. The black, red and blue curves correspond to $M_{\gamma\rho}^2 = 3, 4, 5$ GeV^2 respectively. The dashed (nondashed) lines correspond to the holographic (asymptotic) DA, while the dotted (nondotted) lines correspond to the standard (valence) scenario. $S_{\gamma N}$ is fixed at 20 GeV^2.

On the other hand, the value of the cross section itself decreases. When integrating over $(-u')$, these two competing effects will become clearer later when we show the single differential plots in Sec. V C 2 as a function of $M_{\gamma\rho}^2$, leading to a peak in the distribution at low values of $M_{\gamma\rho}^2$. In general, the GPD model corresponding to the standard scenario leads to a larger value for the cross section. The maximum value of $(-u')$ allowed by the kinematics, attained when $-t = (-t)_{\max}$, is given by (see Appendix E of Ref. [14])

$$(-u')_{\mathrm{maxMax}} = (-t)_{\max} - m_\rho^2 + M_{\gamma\rho}^2 - (-t')_{\min}. \quad (5.3)$$

In the case of the ρ meson, this has the effect of cutting the upper end of the $(-u')$ range at a smaller value, compared to the pion case; see Fig. 3 of Ref. [14]. In general, using a holographic DA gives a higher cross section than using an asymptotic DA. We observe that the model used for the

GPD (valence vs standard) has a small effect for the photoproduction of $\gamma\rho_p^+$ and $\gamma\rho_p^0$, compared to $\gamma\rho_n^-$ and $\gamma\rho_n^0$. Finally, we note that the case of $\gamma\rho^0$ photoproduction on a proton target has the largest cross section, followed by the two charged ρ-meson cases, and lastly the $\gamma\rho^0$ photoproduction on a neutron target.

The corresponding figure for the differential cross section as a function of $(-u')$ for the chiral-odd case is shown in Fig. 3. In this case, the cross section increases with $(-u')$, as opposed to the chiral-even case. Although the chiral-odd cross section seems smaller than the chiral-even one at first sight, the maximum value over the range of $(-u')$ plays a key role when one performs the phase space integration over $(-u')$ and $(-t)$ (as can be understood from the phase space figures in Appendix D of Ref. [13]). This explains why the single differential cross sections as a function of $M_{\gamma\rho}^2$ are not heavily suppressed for the chiral-odd case when compared with the chiral-even one; see
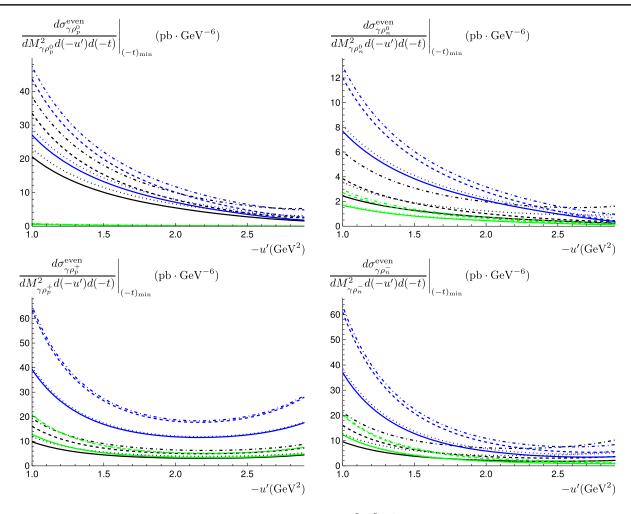
FIG. 4.　The fully differential cross section for longitudinally polarized $\rho_p^0, \rho_n^0, \rho_p^+, \rho_n^-$ is shown as a function of $(-u')$ in the top left, top right, bottom left and bottom right plots respectively. The blue and green curves correspond to contributions from the vector and axial GPDs respectively. The black curves correspond to the total contribution, i.e. vector and axial GPD contributions combined. As before, the dashed (nondashed) lines correspond to the holographic (asymptotic) DA, while the dotted (nondotted) lines correspond to the standard (valence) scenario. We fix $S_{\gamma N} = 20$ GeV^2 and $M_{\gamma\rho}^2 = 4$ GeV^2. Note that the vector contributions consist of only two curves in each case, since they are insensitive to either valence or standard scenarios.

Figs. 7 and 8. We observe that the case of photoproduction of $\gamma\rho_n^0$ has the strongest dependence on the GPD model used. This can be traced back to the larger sensitivity of the d-quark transversity GPD vs the u-quark one, as can be seen from Fig. 4 in Ref. [13]. As with the chiral-even case, using a holographic DA gives the larger cross section.

An interesting observation is that the plots for $\gamma\rho_p^+$ and $\gamma\rho_n^-$ are very similar. In fact, a closer look indicates that the difference between them becomes negligible when $(-u')$ becomes larger. This effect can be traced back to Eqs. (4.51), (4.52), (4.55) and (4.56). One then finds that the only difference between the amplitudes of ρ_p^+ and ρ_n^- comes from the terms $(Q_1^2 - Q_2^2)N_{TA}^q[(AB)_{123}]^a$ and $(Q_1^2 - Q_2^2)N_{TB}^q[(AB)_{123}]^a$, since they are antisymmetric with respect to the exchange of Q_1 and Q_2. Furthermore,

from Eq. (A23), one finds that $N_{TA}^q[(AB)_{123}]^a = 0$. In the cross section (4.62), one also observes that the coefficient $|N_{T\rho A}|^2$ has a factor of α^4 in front compared to the $|N_{T\rho B}|^2$, which includes the contribution $N_{TB}^q[(AB)_{123}]^a$ that causes the difference between $\gamma\rho_p^+$ and $\gamma\rho_n^-$. Since $\alpha \propto (-u')$ [see Eq. (2.17)], this explains why the difference between ρ_p^+ and ρ_n^- becomes negligible as $(-u')$ increases.

The relative contributions of the vector and axial GPDs to the cross section for the longitudinally polarized ρ meson are shown in Fig. 4. The kinematical variables chosen for the plots are $S_{\gamma N} = 20$ GeV^2 and $M_{\gamma\rho}^2 = 4$ GeV^2. The first point to note is that the vector contribution does not depend on the valence or standard scenarios, since they only enter the modeling of the axial GPDs. Hence, only two blue curves appear in each plot in the figure, corresponding to
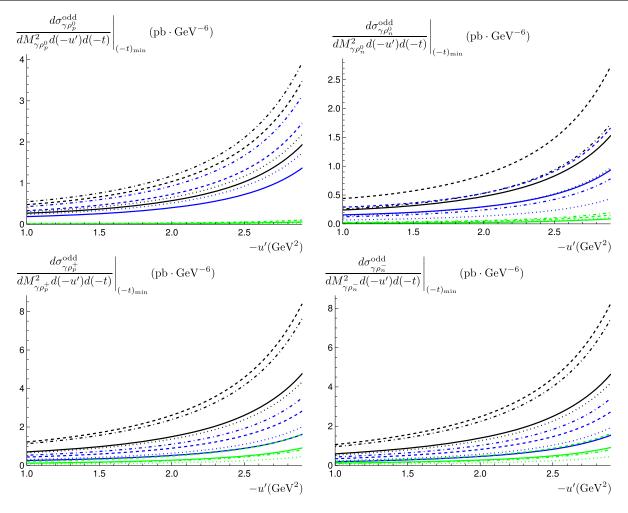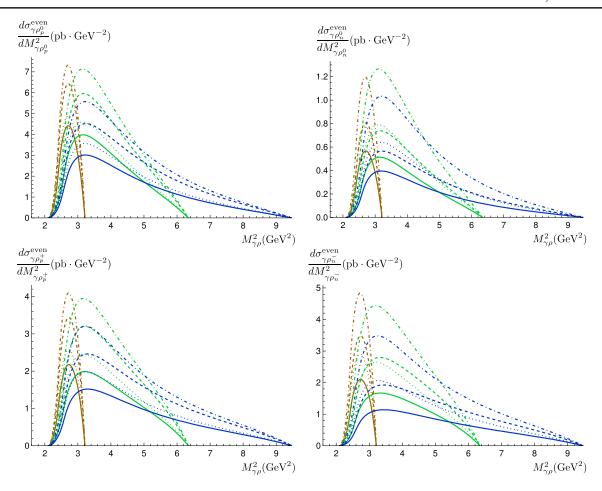
FIG. 5.   The fully differential cross section for longitudinally polarized $\rho_p^0, \rho_n^0, \rho_p^+, \rho_n^-$ is shown as a function of $(-u')$ in the top left, top right, bottom left and bottom right plots respectively. The blue and green curves correspond to contributions from the u-quark (H_u and $\tilde{H}_u$) and d-quark (H_d and $\tilde{H}_d$) GPDs respectively. The black curves correspond to the total contribution. Otherwise, conventions are the same as in previous plots. We fix $S_{\gamma N} = 20$ GeV^2 and $M_{\gamma\rho}^2 = 4$ GeV^2.

the DA model. Moreover, we note that the total contribution (black curve) corresponds simply to the sum of the vector (blue) and axial (green) contributions, since there is no interference between them; see Eq. (4.32). We thus find that the largest contribution to the cross section for the neutral meson case comes from the vector GPDs H, while the contribution from the axial GPDs become more important for the charged ρ-meson cases. This effect was also observed in the case of charged pions (see Fig. 4 in Ref. [1] and Fig. 4 in Ref. [14]).

To conclude this subsection, the relative contributions of the u- and d-quark GPDs to the cross section are shown in Fig. 5 for the longitudinally polarized ρ-meson case and Fig. 6 for the transversely polarized ρ-meson case. To generate the plots, $S_{\gamma N} = 20$ GeV^2 and $M_{\gamma\rho}^2 = 4$ GeV^2 were used. Here, unlike in Fig. 4, there are important interference terms between the u-quark and d-quark contributions, and therefore, the total contribution (black) is

not simply a sum of the individual quark GPD contributions. An interesting point to note is that the interference terms (which are not shown in the plots) are very sensitive to the axial GPDs $\tilde{H}$.

2. Single differential cross section

We now integrate over the kinematical variables $(-u')$ and $(-t)$ and obtain the single differential cross section as a function of $M_{\gamma\rho}^2$. The details of this integration are given in Appendix D of Ref. [13], and in Appendix E of Ref. [14]. The ansatz used for the t dependence of the cross section has been modified in this work [see Eq. (5.1)] compared to the previous paper [13], leading to slightly different values for the cross sections. The effect of different values of $S_{\gamma N}$ on the single differential cross section is shown in Fig. 7 for the chiral-even case and in Fig. 8 for the chiral-odd case. The different colors, brown, green and blue, correspond to
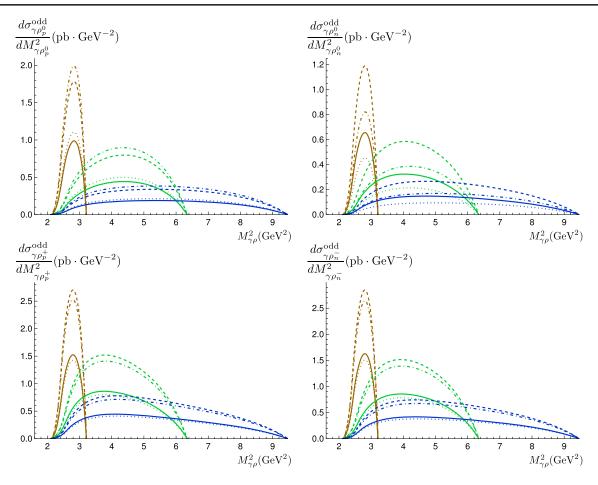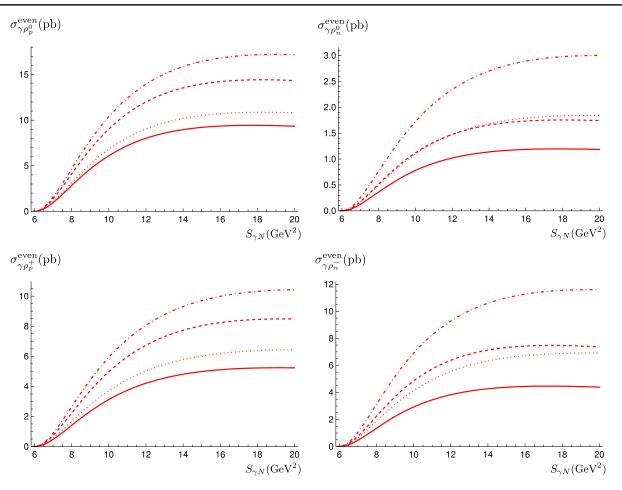
FIG. 6. The fully differential cross section for transversely polarized $\rho_p^0, \rho_n^0, \rho_p^+, \rho_n^-$ is shown as a function of $(-u')$ in the top left, top right, bottom left and bottom right plots respectively. The blue and green curves correspond to contributions from the u-quark (H_u and $\tilde{H}_u$) and d-quark (H_d and $\tilde{H}_d$) GPDs respectively. The black curves correspond to the total contribution. Otherwise, conventions are the same as in previous plots. We fix $S_{\gamma N} = 20$ GeV^2 and $M_{\gamma\rho}^2 = 4$ GeV^2.

FIG. 7. The single differential cross section for longitudinally polarized $\rho_p^0, \rho_n^0, \rho_p^+, \rho_n^-$ is shown as a function of $M_{\gamma\rho}^2$ in the top left, top right, bottom left and bottom right plots respectively for different values of $S_{\gamma N}$. The brown, green and blue curves correspond to $S_{\gamma N} = 8, 14, 20 \text{ GeV}^2$. The dashed (nondashed) lines correspond to the holographic (asymptotic) DA, while the dotted (nondotted) lines correspond to the standard (valence) scenario.

FIG. 8. The single differential cross section for transversely polarized $\rho_p^0, \rho_n^0, \rho_p^+, \rho_n^-$ is shown as a function of $M_{\gamma\rho}^2$ in the top left, top right, bottom left and bottom right plots respectively for different values of $S_{\gamma N}$. The brown, green and blue curves correspond to $S_{\gamma N} = 8, 14, 20$ GeV^2. The dashed (nondashed) lines correspond to the holographic (asymptotic) DA, while the dotted (nondotted) lines correspond to the standard (valence) scenario.

FIG. 9. The integrated cross section for longitudinally polarized $\rho_p^0, \rho_n^0, \rho_p^+, \rho_n^-$ is shown as a function of $S_{\gamma N}$ in the top left, top right, bottom left and bottom right plots respectively. The dashed (nondashed) lines correspond to the holographic (asymptotic) DA, while the dotted (nondotted) lines correspond to the standard (valence) scenario.

$S_{\gamma N}$ values of 8, 14 and 20 GeV^2 respectively. As $S_{\gamma N}$ increases, the maximum value of $M_{\gamma\rho}^2$ increases (simply due to the increase in the phase space), while the value of the cross section decreases.[14]

As previously mentioned, the peaks in the plots in Figs. 7 and 8 are the consequence of the competition between the decrease in the cross section and the increase in the volume of the phase space as $M_{\gamma\rho}^2$ increases. An interesting point to note is that the peak of the distribution is always found at *low* $M_{\gamma\rho}^2$, around 3 GeV^2. The reason for this is that the cross section grows rapidly as $M_{\gamma\rho}^2$ decreases, but at the same time, the kinematical cuts that we impose to use collinear QCD factorization causes the volume of the phase space to vanish at a minimum value of $M_{\gamma\rho}^2$ of about 2.1 GeV^2. Furthermore, the height of the peak in the chiral-odd case decreases faster as $S_{\gamma N}$ increases. This can be

traced back to the ξ^2 prefactor in Eq. (4.62), since ξ decreases as $M_{\gamma\rho}^2$ decreases.

Like for the fully differential cross section plots, we observe that the case of the photoproduction of $\gamma\rho_n^0$ has the strongest dependence on the GPD model used for the chiral-odd case, while both $\gamma\rho_n^0$ and $\gamma\rho_n^-$ channels (i.e. on a neutron target) are very sensitive to the GPD model used for the chiral-even case. Finally, in both chiral-even and chiral-odd cases, using a holographic DA instead of an asymptotic DA gives a larger cross section, by a factor of roughly 2.

3. Integrated cross section

In this subsection, we discuss the variation of the cross section as a function of $S_{\gamma N}$, after integration over $(-u')$, $(-t)$ and $M_{\gamma\rho}^2$. The details of the integration are found in Appendix D of Ref. [13] and Appendix E of Ref. [14]. The variation of the cross section as a function of $S_{\gamma N}$ is shown in Fig. 9 for the chiral-even case and Fig. 10 for the chiral-odd case. In both cases, the cross section has a peak, which occurs at around 20 GeV^2 for the chiral-even case, and

---

[14]A similar effect was observed in Fig. 2 with increasing $M_{\gamma\rho}^2$, instead of $S_{\gamma N}$.
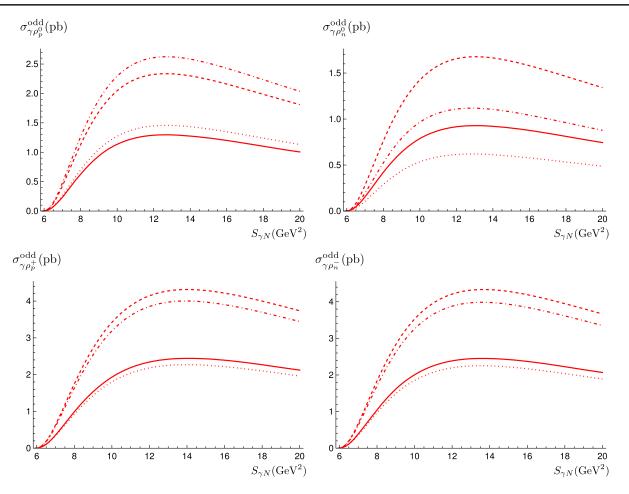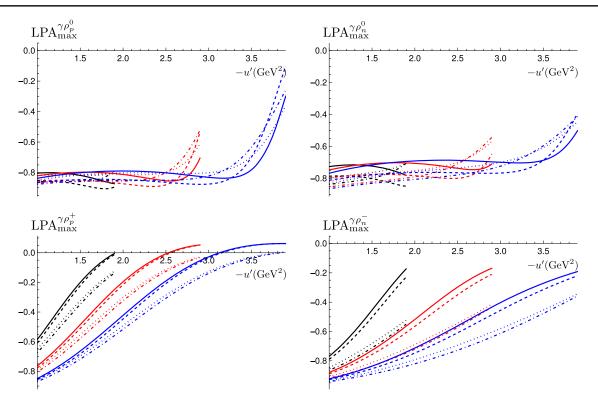
FIG. 10.   The integrated cross section for transversely polarized $\rho_p^0, \rho_n^0, \rho_p^+, \rho_n^-$ is shown as a function of $S_{\gamma N}$ in the top left, top right, bottom left and bottom right plots respectively. The dashed (nondashed) lines correspond to the holographic (asymptotic) DA, while the dotted (nondotted) lines correspond to the standard (valence) scenario.

FIG. 11. The LPA at the fully differential level for longitudinally polarized $\rho_p^0, \rho_n^0, \rho_p^+, \rho_n^-$ is shown as a function of $(-u')$ in the top left, top right, bottom left and bottom right plots respectively for different values of $M_{\gamma\rho}^2$. The black, red and blue curves correspond to $M_{\gamma\rho}^2 = 3, 4, 5$ GeV^2 respectively, and $S_{\gamma N} = 20$ GeV^2. The same conventions as in Fig. 2 are used here.

around 12 GeV^2 for the chiral-odd case (in the chiral-even case, the presence of the peak becomes evident in Fig. 23 which corresponds to the same plot but extends to higher energies typical of COMPASS kinematics). In accordance with Figs. 7 and 8, where we observed that the peak of the single-differential cross section decreases more rapidly with increasing $S_{\gamma N}$ for the chiral-odd case, we observe here that the peak in the integrated cross section occurs at lower values of $S_{\gamma N}$ with chiral-odd GPDs. Similar comments as in the previous subsection apply, i.e. the case of the photoproduction of $\gamma\rho_n^0$ has the strongest dependence on the GPD model used for the chiral-odd case, while both $\gamma\rho_n^0$ and $\gamma\rho_n^-$ channels (i.e. on a neutron target) are very sensitive to the GPD model used for the chiral-even case. Furthermore, in both chiral-even and chiral-odd cases, using a holographic DA instead of an asymptotic DA gives a larger cross section, by a factor of roughly 2.

4. Polarization asymmetries

We now discuss the plots for the LPA. First, we show the effect of different $M_{\gamma\rho}^2$ on the LPAs at the fully differential level [i.e. differential in $(-u')$, $M_{\gamma\rho}^2$ and $(-t)$ as in Sec. V C 1] in Fig. 11. As in Fig. 2, the values of $M_{\gamma\rho}^2$ used are 3, 4 and 5 GeV^2. One thus finds that the process is

dominated by incoming linearly polarized photons along the y direction, since the LPA is in general negative.

For the neutral ρ-meson case, we observe that the LPA has a weak dependence on both the GPD and DA models used, especially at low $(-u')$. Furthermore, the LPA remains quite flat and very sizable except close to the maximum value of $(-u')$. Finally, we also find that the LPA does not change significantly for different values of $M_{\gamma\rho}^2$. Both of the previous two observations make the LPA very promising for being measured at JLab.

For the charged ρ-meson case, the LPA is very sizable at low $(-u')$ and its magnitude gradually decreases as $(-u')$ increases. The shape is thus very different from the neutral ρ-meson one. On the other hand, the shape of the LPA is very similar to the one for the charged $\pi^\pm$ case (see Fig. 8 in Ref. [1]), except that the effect of the GPD model goes in the opposite direction (i.e. the more sizable LPA comes from the standard scenario for the ρ-meson case, but for the $\pi^\pm$, this corresponds to the valence scenario). The LPA also becomes more sizable when $M_{\gamma\rho}^2$ increases.

Next, we show how the relative contributions from the vector and axial GPDs affect the LPA at the fully differential level in Fig. 12. To obtain the green (blue)
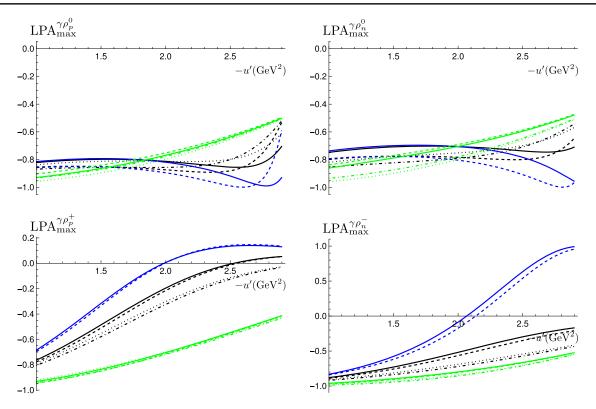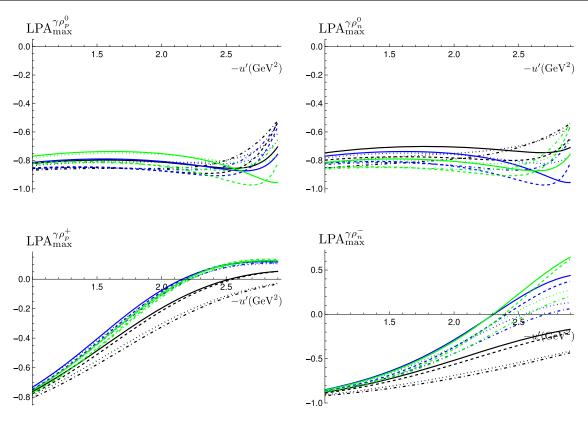
FIG. 12. The LPA at the fully differential level for longitudinally polarized $\rho_p^0, \rho_n^0, \rho_p^+, \rho_n^-$ is shown as a function of $(-u')$ in the top left, top right, bottom left and bottom right plots respectively, using $M_{\gamma\rho}^2 = 4 \text{ GeV}^2$ and $S_{\gamma N} = 20 \text{ GeV}^2$. The same conventions as in Fig. 4 are used here. Note that the vector contributions consist of only two curves in each case, since they are insensitive to either valence or standard scenarios.

FIG. 13. The LPA at the fully differential level for longitudinally polarized $\rho_p^0, \rho_n^0, \rho_p^+, \rho_n^-$ is shown as a function of $(-u')$ in the top left, top right, bottom left and bottom right plots respectively, using $M_{\gamma\rho}^2 = 4$ GeV^2 and $S_{\gamma N} = 20$ GeV^2. The blue and green curves correspond to contributions from the u-quark (H_u and $\tilde{H}_u$) and d-quark (H_d and $\tilde{H}_d$) GPDs respectively. The black curves correspond to the total contribution. The same conventions as in Fig. 5 are used here.

curves, we set *all* vector (axial) contributions to the polarized cross sections to zero, in both the numerator and denominator of Eq. (4.64). In the case of ρ^0, the relative contribution of the axial GPD to the LPA is small at low $(-u')$, but becomes important as $(-u')$ increases, which can be implied from Fig. 4. Interestingly, for ρ^-, the contribution to the LPA from the vector GPD changes from -1 at low $(-u')$ to $+1$ at high $(-u')$. The LPA calculated from the axial GPD contribution has very little sensitivity to the GPD model used, in contrast with the $\pi^\pm$ case, cf. Fig. 9 in Ref. [1].

At first sight, it may seem strange that the GPD model nevertheless has a sizable effect on the total LPA for the ρ meson in Fig. 12. This can be understood from the way the LPA is normalized. Taking the ρ_p^+ as a specific example, one observes that the cross section corresponding to the axial contribution, though small, changes by a factor of roughly 2 between the two GPD models; see Fig. 4. For the LPA, one finds that the axial GPD contribution has a negative value of -0.5 (independent of the GPD model), and has a larger absolute size than

the vector GPD part which is roughly 0.1. Therefore, the only difference between the two GPD models when computing the LPA for the total contribution occurs due to the factor of 2 coming from the cross section, which when coupled with the large negative value of -0.5, leads to a sizable difference.

The relative contributions from the u-quark GPDs (H_u and $\tilde{H}_u$) and d-quark GPDs (H_d and $\tilde{H}_d$) to the LPA are shown in Fig. 13.

Next, we show the LPA, at the single differential level, for different values of $S_{\gamma N}$ in Fig. 14. As for the cross section plots in Sec. V C 2, the values of $S_{\gamma N}$ used are 8, 14 and 20 GeV^2. We note that neither the GPD nor the DA models have a significant effect on the LPA. This is contrast to the $\pi^\pm$ case, where the GPD model had an important effect; see Fig. 11 in Ref. [1]. Moreover, the magnitude of the LPA remains quite large throughout the range of $M_{\gamma\rho}^2$. This makes the LPA at the single differential level very promising to be measured experimentally.

Finally, we show the LPA, integrated over all differential variables, as a function of $S_{\gamma N}$ in Fig. 15. The LPA in all
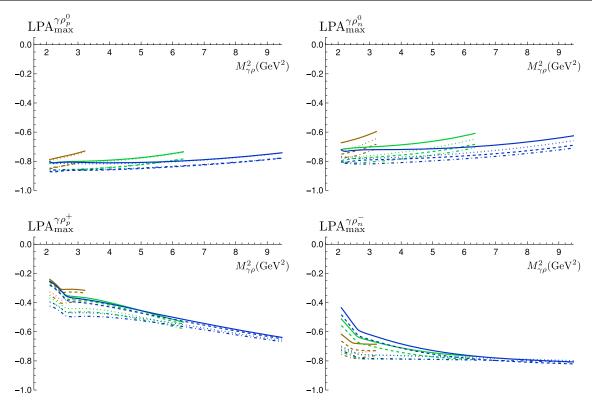
FIG. 14.   The LPA at the single differential level for longitudinally polarized $\rho_p^0, \rho_n^0, \rho_p^+, \rho_n^-$ is shown as a function of $M_{\gamma\rho}^2$ in the top left, top right, bottom left and bottom right plots respectively. The brown, green and blue curves correspond to $S_{\gamma N} = 8, 14, 20$ GeV^2. The same color and line style conventions as in Fig. 7 are used here.
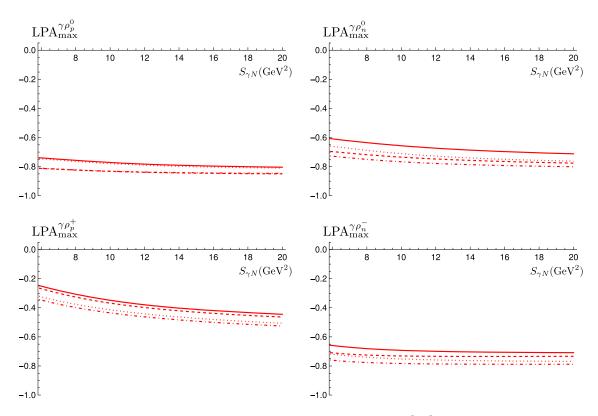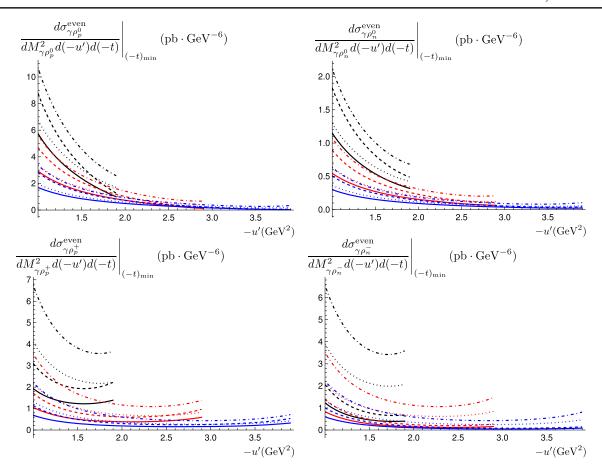

FIG. 15.   The LPA integrated over all differential variables for longitudinally polarized $\rho_p^0, \rho_n^0, \rho_p^+, \rho_n^-$ is shown in the top left, top right, bottom left and bottom right plots respectively. The same color and line style conventions as in Fig. 9 are used here.

FIG. 16. The fully differential cross section for longitudinally polarized $\rho_p^0, \rho_n^0, \rho_p^+, \rho_n^-$ is shown as a function of $(-u')$ in the top left, top right, bottom left and bottom right plots respectively for different values of $M_{\gamma\rho}^2$. The black, red and blue curves correspond to $M_{\gamma\rho}^2 = 3, 4, 5$ GeV^2 respectively. The dashed (nondashed) lines correspond to the holographic (asymptotic) DA, while the dotted (nondotted) lines correspond to the standard (valence) scenario. As mentioned in the main text, $S_{\gamma N}$ is fixed at 200 GeV^2 here.

four plots is rather flat, and is quite sizable, with the ρ_p^+ having the smallest magnitude of roughly 40%, while it goes up to about 80% for the others. As at the single differential level, the LPA here has little sensitivity to the DA and GPD models used. Thus, the LPA is sizable, and taking into account the fact that the expected counting rates found in Sec. V F 1 are large, the measurement of such an observable is very promising.

D. COMPASS kinematics

Typically, COMPASS consists of colliding muons at an energy of 160 GeV onto a fixed target. This translates to a muon-nucleon center-of-mass energy of roughly 301 GeV^2. Since the skewness ξ decreases with increasing $S_{\gamma N}$ [see Eq. (2.16)], COMPASS can in principle give us access to a kinematical region of small ξ for GPDs $(0.0027 \leq \xi \leq 0.35)$, not accessible at JLab. The typical

center-of-mass energy $S_{\gamma N}$ used for the plots that we show in this section is 200 GeV^2.

1. Fully differential cross section

Figure 16 shows the effect of different values of $M_{\gamma\rho}^2$ on the fully differential cross section for the chiral-even case. We choose three different values for $M_{\gamma\rho}^2$, namely $M_{\gamma\rho}^2 = 3, 4, 5$ GeV^2. Compared to the corresponding plots at $S_{\gamma N} = 20$ GeV^2 in Fig. 2, the cross sections here are smaller by a factor of roughly 8. We note that the uncertainty due to the model used is significant for the charged ρ-meson case, and is particularly driven by the GPD model. This allows in principle to discriminate between the two GPD models that are investigated.

The variation of the differential cross section with $(-u')$ for the chiral-odd case is shown in Fig. 17. Here, we note that the cross section is much smaller than in the chiral-even
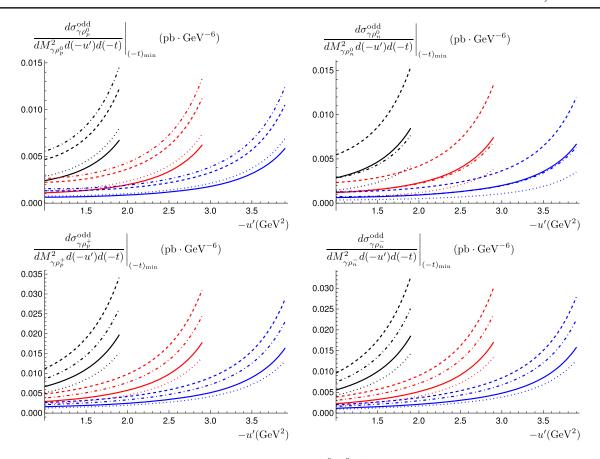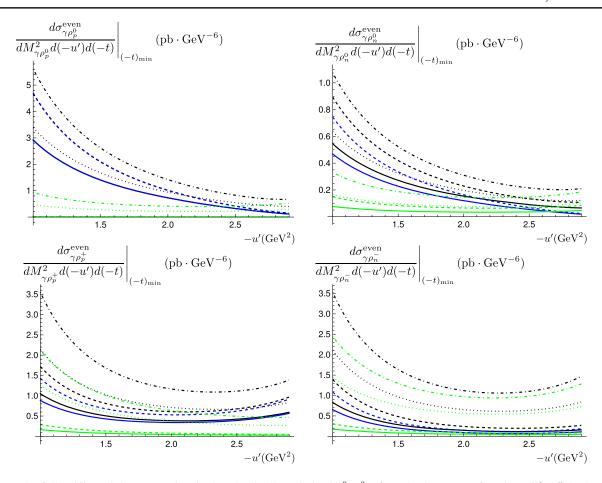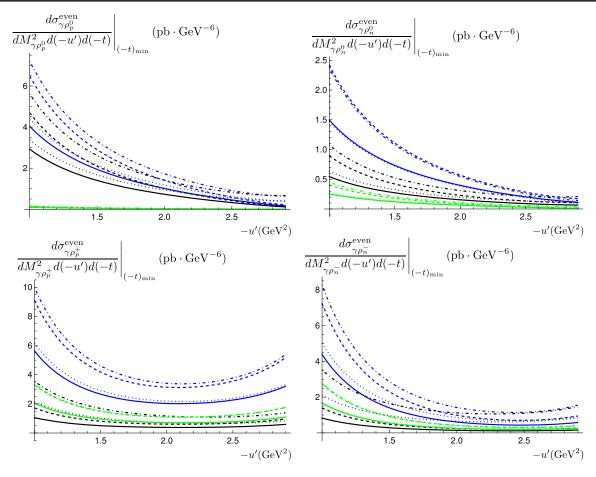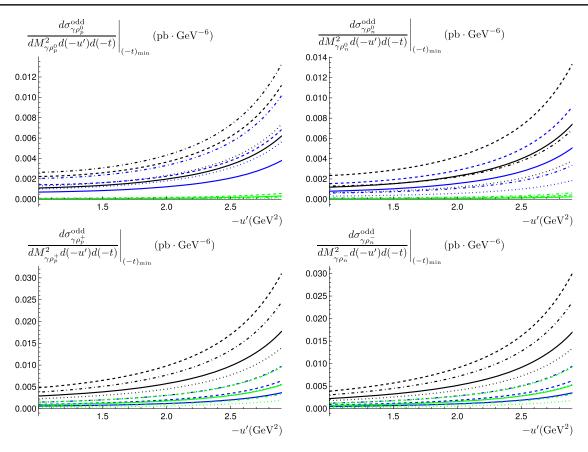
FIG. 17. The fully differential cross section for transversely polarized $\rho_p^0, \rho_n^0, \rho_p^+, \rho_n^-$ is shown as a function of $(-u')$ in the top left, top right, bottom left and bottom right plots respectively for different values of $M_{\gamma\rho}^2$. The black, red and blue curves correspond to $M_{\gamma\rho}^2 = 3$, 4, 5 GeV^2 respectively. The dashed (nondashed) lines correspond to the holographic (asymptotic) DA, while the dotted (nondotted) lines correspond to the standard (valence) scenario. As mentioned in the main text, $S_{\gamma N}$ is fixed at 200 GeV^2 here.

FIG. 18. The fully differential cross section for longitudinally polarized $\rho_p^0, \rho_n^0, \rho_p^+, \rho_n^-$ is shown as a function of $(-u')$ in the top left, top right, bottom left and bottom right plots respectively. The blue and green curves correspond to contributions from the vector and axial GPDs respectively. The black curves correspond to the total contribution, i.e. vector and axial GPD contributions combined. As before, the dashed (nondashed) lines correspond to the holographic (asymptotic) DA, while the dotted (nondotted) lines correspond to the standard (valence) scenario. We fix $S_{\gamma N} = 200$ GeV^2 and $M_{\gamma\rho}^2 = 4$ GeV^2. Note that the vector contributions consist of only two curves in each case, since they are insensitive to either valence or standard scenarios.

FIG. 19. The fully differential cross section for longitudinally polarized $\rho_p^0, \rho_n^0, \rho_p^+, \rho_n^-$ is shown as a function of $(-u')$ in the top left, top right, bottom left and bottom right plots respectively. The blue and green curves correspond to contributions from the u-quark (H_u and $\tilde{H}_u$) and d-quark (H_d and $\tilde{H}_d$) GPDs respectively. The black curves correspond to the total contribution. Otherwise, conventions are the same as in previous plots. We fix $S_{\gamma N} = 200$ GeV^2 and $M_{\gamma\rho}^2 = 4$ GeV^2.

FIG. 20. The fully differential cross section for transversely polarized $\rho_p^0, \rho_n^0, \rho_p^+, \rho_n^-$ is shown as a function of $(-u')$ in the top left, top right, bottom left and bottom right plots respectively. The blue and green curves correspond to contributions from the u-quark (H_u and $\tilde{H}_u$) and d-quark (H_d and $\tilde{H}_d$) GPDs respectively. The black curves correspond to the total contribution. Otherwise, conventions are the same as in previous plots. We fix $S_{\gamma N} = 200$ GeV^2 and $M_{\gamma\rho}^2 = 4$ GeV^2.

case, a feature which is more pronounced than in the JLab kinematics case. This can be attributed to the fact that the amplitude squared is proportional to ξ^2 [see Eq. (4.62)], and ξ becomes smaller at higher center-of-mass energies $S_{\gamma N}$. On the other hand, this ξ^2 factor is absent for the chiral-even case; see Eq. (4.33).

The relative contributions of the vector and axial GPDs to the cross section for the longitudinally polarized ρ-meson case are shown in Fig. 18. Similar comments as in Sec. V C 1 apply.

Finally, to conclude this subsection, the relative contributions of the u-quark and d-quark GPDs to the cross section are shown in Fig. 19 for the chiral-even case, and in Fig. 20 for the chiral-odd case.

2. Single differential cross section

Figure 21 shows the variation of the single differential cross section with $M_{\gamma\rho}^2$ for different values of $S_{\gamma N}$ for the chiral-even case. We choose three different values for

$S_{\gamma N}$, namely 80, 140 and 200 GeV^2. Due to large variations in the cross section over the full range of $M_{\gamma\rho}^2$, a log scale is used for the vertical axis. We observe that the cross section is dominated by the region of very small $M_{\gamma\rho}^2$.

For the chiral-odd case, shown in Fig. 22, we first note that the cross section is smaller with respect to the chiral-even case, by a factor of roughly 100. In particular, the height of the peak for the chiral-odd case is much lower than that in the chiral-even case. Again, this is related to the ξ^2 suppression factor that comes from the square of the chiral-odd amplitude.

3. Integrated cross section

In Fig. 23, we show the variation of the integrated cross section as a function of $S_{\gamma N}$ for the chiral-even case. We cover the entire kinematical range of COMPASS by going to $S_{\gamma N} = 300$ GeV^2. The peak of the cross section occurs at around 20 GeV^2.
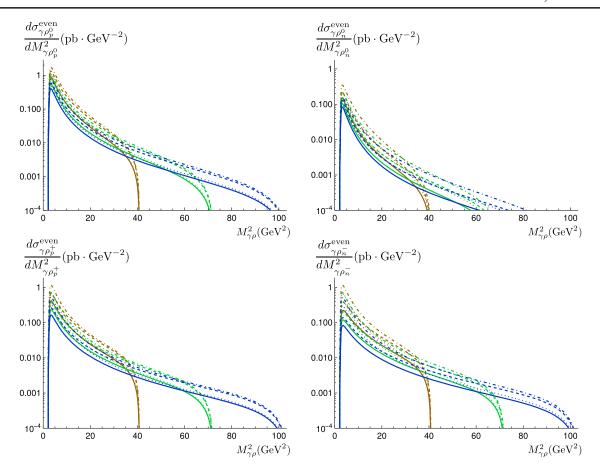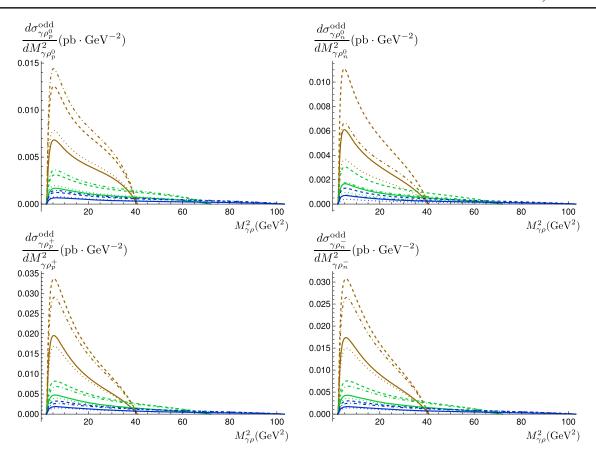
FIG. 21. The single differential cross section for longitudinally polarized $\rho_p^0, \rho_n^0, \rho_p^+, \rho_n^-$ is shown as a function of $M_{\gamma\rho}^2$ in the top left, top right, bottom left and bottom right plots respectively for different values of $S_{\gamma N}$. The brown, green and blue curves correspond to $S_{\gamma N} = 80, 140, 200$ GeV^2. The dashed (nondashed) lines correspond to the holographic (asymptotic) DA, while the dotted (nondotted) lines correspond to the standard (valence) scenario. The holographic DA with the standard scenario has the largest contribution for every $S_{\gamma N}$.

FIG. 22.   The single differential cross section for transversely polarized $\rho_p^0, \rho_n^0, \rho_p^+, \rho_n^-$ is shown as a function of $M_{\gamma\rho}^2$ in the top left, top right, bottom left and bottom right plots respectively for different values of $S_{\gamma N}$. The brown, green and blue curves correspond to $S_{\gamma N} = 80, 140, 200 \text{ GeV}^2$. The dashed (nondashed) lines correspond to the holographic (asymptotic) DA, while the dotted (nondotted) lines correspond to the standard (valence) scenario.

FIG. 23. The integrated cross section for longitudinally polarized $\rho_p^0, \rho_n^0, \rho_p^+, \rho_n^-$ is shown as a function of $S_{\gamma N}$ in the top left, top right, bottom left and bottom right plots respectively. The dashed (nondashed) lines correspond to the holographic (asymptotic) DA, while the dotted (nondotted) lines correspond to the standard (valence) scenario. We thus find that the maximum cross section appears at around 20 GeV^2, a feature which was not clear in Fig. 9.

For the chiral-odd case, the variation of the integrated cross section as a function of $S_{\gamma N}$ is shown in Fig. 24. The cross section here also has a peak at around 20 GeV^2, but falls more rapidly with increasing $S_{\gamma N}$ thereafter. Consequently, only the region of $S_{\gamma N}$ close to the peak is relevant for the chiral-odd case.

4. Polarization asymmetries

In this section, we show the results for the LPAs for COMPASS kinematics. As for the cross section plots in the previous section, we choose the reference value of 200 GeV^2 for $S_{\gamma N}$ for the fully differential and single differential plots. As discussed in Sec. V C 4, the plots that we show here correspond to LPA$_{max}$. Furthermore, we note that only plots of the LPAs for the chiral-even case are shown here, since the LPAs for the chiral-odd case vanish.

In Fig. 25, the LPAs at the fully differential level are shown as a function of $(-u')$, for different values of $M_{\gamma\rho}^2$.

The three values of $M_{\gamma\rho}^2$ that we use are $M_{\gamma\rho}^2 = 3, 4, 5$ GeV^2, which correspond to the black, red and blue curves respectively. As in the JLab kinematics case, we observe that for the charged ρ-meson case, the LPAs can be used to discriminate between the GPD models used. Furthermore, for the ρ_n^- case, the sign of the LPA changes from negative to positive as $(-u')$ increases for the valence scenario only.

In Fig. 26, we show the relative contributions of the vector and axial GPDs to the LPA at the fully differential level. The values $S_{\gamma N} = 200$ GeV^2 and $M_{\gamma\rho}^2 = 4$ GeV^2 are used to generate the plots. For the ρ_p^0 case, the LPA remains very negative and relatively flat, except for the axial contribution in the standard GPD scenario. For ρ_n^0, we observe that the LPA remains rather flat at very negative values throughout the range of $(-u')$. Finally, for the charged ρ-meson case, the LPA covers a wider range, starting at a sizable value at low $(-u')$.
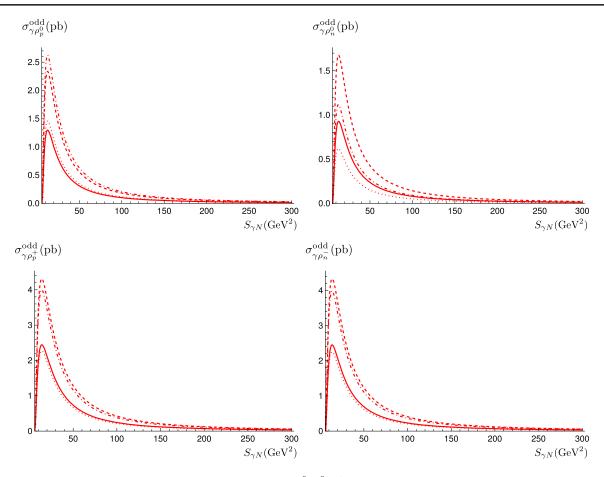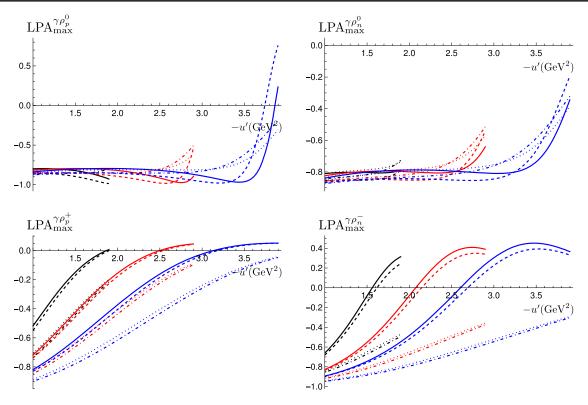
FIG. 24. The integrated cross section for transversely polarized $\rho_p^0, \rho_n^0, \rho_p^+, \rho_n^-$ is shown as a function of $S_{\gamma N}$ in the top left, top right, bottom left and bottom right plots respectively. The dashed (nondashed) lines correspond to the holographic (asymptotic) DA, while the dotted (nondotted) lines correspond to the standard (valence) scenario.
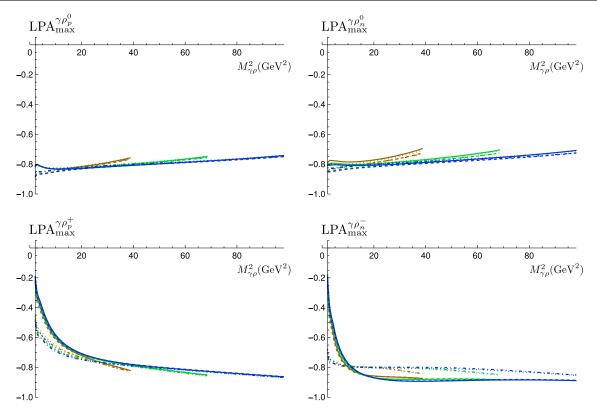
FIG. 25. The LPA at the fully differential level for longitudinally polarized $\rho_p^0, \rho_n^0, \rho_p^+, \rho_n^-$ is shown as a function of $(-u')$ in the top left, top right, bottom left and bottom right plots respectively for different values of $M_{\gamma\rho}^2$. The black, red and blue curves correspond to $M_{\gamma\rho}^2 = 3, 4, 5 \text{ GeV}^2$ respectively, and $S_{\gamma N} = 200 \text{ GeV}^2$. The same conventions as in Fig. 16 are used here.

FIG. 26. The LPA at the fully differential level for longitudinally polarized $\rho_p^0, \rho_n^0, \rho_p^+, \rho_n^-$ is shown as a function of $(-u')$ in the top left, top right, bottom left and bottom right plots respectively, using $M_{\gamma\rho}^2 = 4$ GeV^2 and $S_{\gamma N} = 200$ GeV^2. The same conventions as in Fig. 18 are used here. Note that the vector contributions consist of only two curves in each case, since they are insensitive to either valence or standard scenarios.

FIG. 27. The LPA at the fully differential level for longitudinally polarized $\rho_p^0, \rho_n^0, \rho_p^+, \rho_n^-$ is shown as a function of $(-u')$ in the top left, top right, bottom left and bottom right plots respectively, using $M_{\gamma\rho}^2 = 4$ GeV^2 and $S_{\gamma N} = 200$ GeV^2. The blue and green curves correspond to contributions from the u-quark (H_u and $\tilde{H}_u$) and d-quark (H_d and $\tilde{H}_d$) GPDs respectively. The black curves correspond to the total contribution. The same conventions as in Fig. 19 are used here.

FIG. 28.   The LPA at the single differential level for longitudinally polarized $\rho_p^0, \rho_n^0, \rho_p^+, \rho_n^-$ is shown as a function of $M_{\gamma\rho}^2$ in the top left, top right, bottom left and bottom right plots respectively. The brown, green and blue curves correspond to $S_{\gamma N} = 80, 140, 200$ GeV^2. The same color and line style conventions as in Fig. 21 are used here.

The relative contributions of the u-quark and d-quark GPDs to the LPA at the fully differential level are shown in Fig. 27. We choose $S_{\gamma N} = 200$ GeV^2 and $M_{\gamma\rho}^2 = 4$ GeV^2 to generate the plots.

In Fig. 28, we show the variation of the LPA at the single-differential level as a function of $M_{\gamma\rho}^2$ for different values of $S_{\gamma N}$. We observe that the LPA is rather flat at a value of about -0.8, with the exception of the charged ρ-meson case at low $M_{\gamma\rho}^2$. Furthermore, we note that the GPD or DA model used has little effect on the LPA, with the exception of the ρ_n^- case, where the GPD model nevertheless has a non-negligible effect. This is in contrast to the charged $\pi^\pm$, where we found that the LPA is very sensitive to the GPD model; see Fig. 21 in Ref. [1].

To conclude this section on COMPASS kinematics, the variation of the LPA, integrated over all differential variables, is shown as a function of $S_{\gamma N}$ in Fig. 29. Here, the LPA is again rather flat at roughly -0.8 with the exception of the ρ_p^+ case, for which the magnitude of the LPA is smaller. We also observe that the LPA is rather insensitive to the GPD or DA model used, except for the charged ρ-meson cases, for which the GPD model has an effect.

E. EIC and UPCs at LHC kinematics

We consider photon-nucleon center-of-mass energies $S_{\gamma N}$ of up to $20\,000$ GeV^2. Such a choice covers the whole range of the expected EIC kinematics (with a maximum center-of-mass energy of the electron-proton system of roughly $19\,600$ GeV^2 [21]), and the most relevant part of LHC UPC kinematics (which in principle involves center-of-mass energies of the order of the TeV scale).

Increasing the center-of-mass energy causes the skewness ξ to decrease; see Eq. (5.2). At $S_{\gamma N} = 20\,000$ GeV^2, ξ can reach as low as $\sim 10^{-4}$. One might therefore ask the question of whether small-x resummation effects (and ultimately saturation effects), in which gluons play an essential role, could become important in that kinematical domain. First, we note that for charged ρ mesons in the final state, quarks have to be exchanged in the t channel, simply by virtue of charge conservation. For the neutral ρ^0-meson case, which is C-odd, gluon exchanges start at next-to-leading order, resulting in the C-odd odderon exchange. This odderon exchange is poorly known and is presumably not too large [22–24], and a detailed discussion of this exchange is beyond the scope of our work.
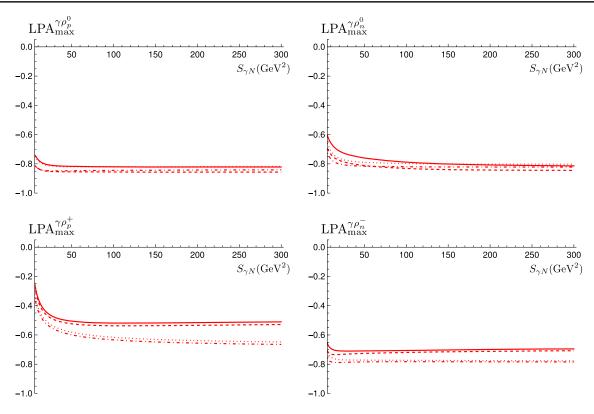
FIG. 29.   The LPA integrated over all differential variables for longitudinally polarized $\rho_p^0, \rho_n^0, \rho_p^+, \rho_n^-$ is shown in the top left, top right, bottom left and bottom right plots respectively as a function of $S_{\gamma N}$. The same color and line style conventions as in Fig. 23 are used here.
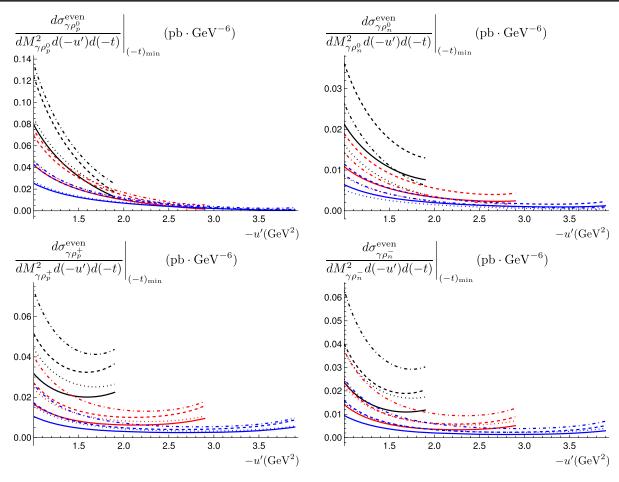
FIG. 30. The fully differential cross section for longitudinally polarized $\rho_p^0, \rho_n^0, \rho_p^+, \rho_n^-$ is shown as a function of $(-u')$ in the top left, top right, bottom left and bottom right plots respectively for different values of $M_{\gamma\rho}^2$. The black, red and blue curves correspond to $M_{\gamma\rho}^2 = 3, 4, 5 \text{ GeV}^2$ respectively. The dashed (nondashed) lines correspond to the holographic (asymptotic) DA, while the dotted (nondotted) lines correspond to the standard (valence) scenario. As mentioned in the main text, $S_{\gamma N}$ is fixed at $20\,000 \text{ GeV}^2$ here.

For UPCs at LHC kinematics, we note that both the cross section and the photon flux drop very rapidly as $S_{\gamma N}$ increases. Therefore, only a tiny contribution is lost by neglecting contributions which are beyond the kinematics of EIC, i.e. above $S_{\gamma N} = 20\,000 \text{ GeV}^2$.

1. Fully differential cross section

At large $S_{\gamma N}$, typical of EIC and UPCs at LHC kinematics, the cross section for the chiral-odd case is heavily suppressed compared to the chiral-even case. As mentioned before, this is due to the ξ^2 factor that appears in front of the squared amplitude for the chiral-odd case. Consequently, in this section, we only show the plots for the chiral-even case.

In Fig. 30, the fully differential cross section as a function of $(-u')$ is shown for different values of $M_{\gamma\rho}^2$. We choose $S_{\gamma N} = 20\,000 \text{ GeV}^2$. For $M_{\gamma\rho}^2$, we take $M_{\gamma\rho}^2 = 3, 4, 5 \text{ GeV}^2$, since the cross section becomes much

smaller at higher values of $M_{\gamma\rho}^2$. We observe a decrease of the cross section by a factor of roughly 100 compared to the COMPASS kinematics case in Sec. V D 1.

The relative contributions of the vector and axial GPDs to the fully differential cross section are shown in Fig. 31 as a function of $(-u')$. The plots are generated using $M_{\gamma\rho}^2 = 4 \text{ GeV}^2$ and $S_{\gamma N} = 20\,000 \text{ GeV}^2$.

To conclude this subsection, we show the relative contributions of the u-quark and d-quark GPDs to the fully differential cross section in Fig. 32, as a function of $(-u')$. The value of $S_{\gamma N}$ is fixed at $20\,000 \text{ GeV}^2$ and $M_{\gamma\rho}^2$ at 4 GeV^2.

2. Single differential cross section

We proceed as in Sec. V E 1, and show only plots for the dominant chiral-even case.

Here, we show the variation of the cross section at the single-differential level as a function of $M_{\gamma\rho}^2$ for different
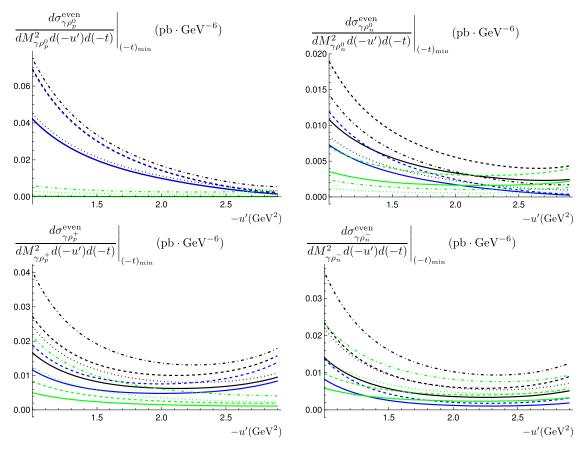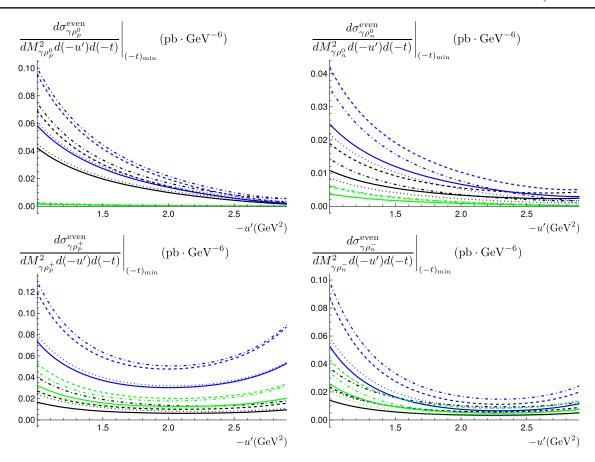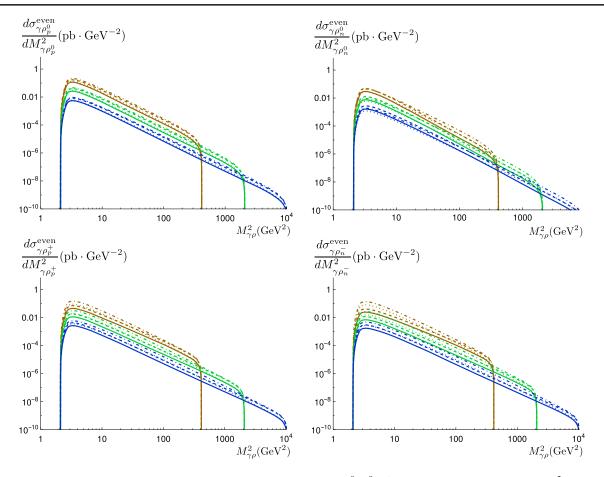
FIG. 31. The fully differential cross section for longitudinally polarized $\rho_p^0, \rho_n^0, \rho_p^+, \rho_n^-$ is shown as a function of $(-u')$ in the top left, top right, bottom left and bottom right plots respectively. The blue and green curves correspond to contributions from the vector and axial GPDs respectively. The black curves correspond to the total contribution, i.e. vector and axial GPD contributions combined. As before, the dashed (nondashed) lines correspond to the holographic (asymptotic) DA, while the dotted (nondotted) lines correspond to the standard (valence) scenario. We fix $S_{\gamma N} = 20\,000$ GeV^2 and $M_{\gamma\rho}^2 = 4$ GeV^2. Note that the vector contributions consist of only two curves in each case, since they are insensitive to either valence or standard scenarios.

FIG. 32. The fully differential cross section for longitudinally polarized $\rho_p^0, \rho_n^0, \rho_p^+, \rho_n^-$ is shown as a function of $(-u')$ in the top left, top right, bottom left and bottom right plots respectively. The blue and green curves correspond to contributions from the u-quark (H_u and $\tilde{H}_u$) and d-quark (H_d and $\tilde{H}_d$) GPDs respectively. The black curves correspond to the total contribution. Otherwise, conventions are the same as in previous plots. We fix $S_{\gamma N} = 20\,000 \text{ GeV}^2$ and $M_{\gamma\rho}^2 = 4 \text{ GeV}^2$.

FIG. 33. The single differential cross section for longitudinally polarized $\rho_p^0, \rho_n^0, \rho_p^+, \rho_n^-$ is shown as a function of $M_{\gamma\rho}^2$ in the top left, top right, bottom left and bottom right plots respectively for different values of $S_{\gamma N}$. The brown, green and blue curves correspond to $S_{\gamma N} = 800, 4000, 20\,000$ GeV^2. The dashed (nondashed) lines correspond to the holographic (asymptotic) DA, while the dotted (nondotted) lines correspond to the standard (valence) scenario. Note that both axes are log scales.

values of $S_{\gamma N}$ in Fig. 33. We choose three different values for $S_{\gamma N}$, namely 800, 4000 and 20 000 GeV^2 for the brown, green and blue curves respectively. We observe that the peak of the cross section lies at low values of $M_{\gamma\rho}^2$ (roughly 3–4 GeV^2).

3. Integrated cross section

In Fig. 34, the variation of the integrated cross section as a function of $S_{\gamma N}$ is shown for the chiral-even case. We observe that the largest cross section is obtained by using a holographic DA model and the GPD model corresponding to the standard scenario (dash-dotted line). We note that the cross section falls to very low values at $S_{\gamma N} = 20\,000$ GeV^2, roughly 200 times less than its value at the peak, which occurs at around 20 GeV^2. This, coupled with the fact that the photon flux in UPCs also decreases with $S_{\gamma N}$, justifies the truncation at $S_{\gamma N} = 20\,000$ GeV^2

when considering UPCs at LHC kinematics, which involves TeV energies.

The corresponding plots for the chiral-odd case are shown in Fig. 35. Here, we observe that the cross section, after the peak, drops at a much faster rate compared to the chiral-even case. In fact, the cross section at $S_{\gamma N} = 20\,000$ GeV^2 drops by a factor of roughly 10^6 compared to its value at the peak.

4. Polarization asymmetries

We recall that the LPA for the chiral-odd case vanishes, and therefore, we only show plots for the chiral-even case in this section.

In Fig. 36, the LPA at the fully differential level is shown as a function of $(-u')$, for different values of $M_{\gamma\rho}^2$. The kinematical values chosen are $S_{\gamma N} = 20\,000$ GeV^2, and $M_{\gamma\rho}^2 = 3, 4, 5$ GeV^2. The behavior of the LPA is similar to the ones described in previous sections.
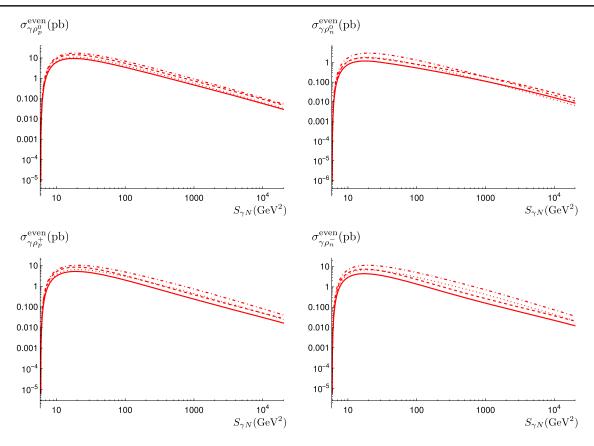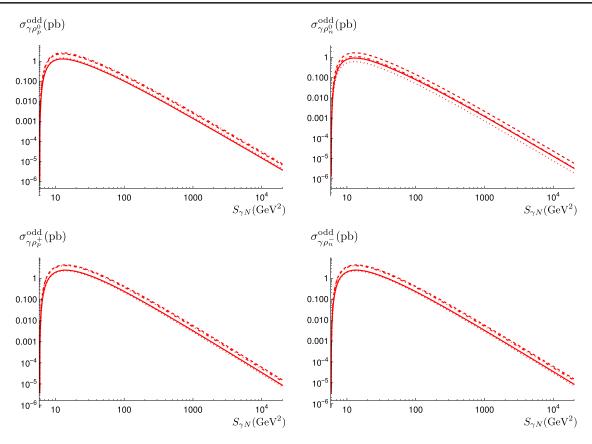
FIG. 34.   The integrated cross section for longitudinally polarized $\rho_p^0, \rho_n^0, \rho_p^+, \rho_n^-$ is shown as a function of $S_{\gamma N}$ in the top left, top right, bottom left and bottom right plots respectively. The dashed (nondashed) lines correspond to the holographic (asymptotic) DA, while the dotted (nondotted) lines correspond to the standard (valence) scenario.
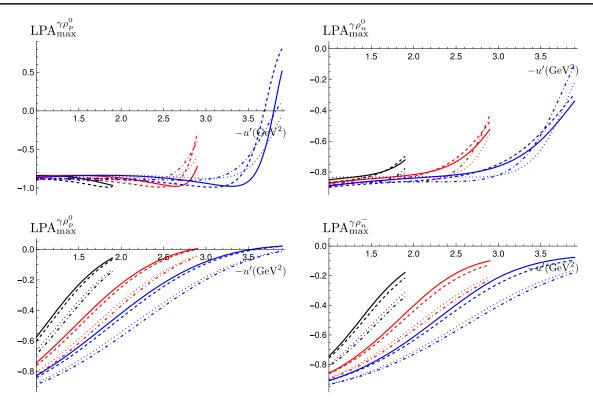
FIG. 35. The integrated cross section for transversely polarized $\rho_p^0, \rho_n^0, \rho_p^+, \rho_n^-$ is shown as a function of $S_{\gamma N}$ in the top left, top right, bottom left and bottom right plots respectively. The dashed (nondashed) lines correspond to the holographic (asymptotic) DA, while the dotted (nondotted) lines correspond to the standard (valence) scenario.

FIG. 36.   The LPA at the fully differential level for longitudinally polarized $\rho_p^0, \rho_n^0, \rho_p^+, \rho_n^-$ is shown as a function of $(-u')$ in the top left, top right, bottom left and bottom right plots respectively for different values of $M_{\gamma\rho}^2$. The black, red and blue curves correspond to $M_{\gamma\rho}^2 = 3, 4, 5 \text{ GeV}^2$ respectively, and $S_{\gamma N} = 20\,000 \text{ GeV}^2$. The same conventions as in Fig. 30 are used here.

FIG. 37. The LPA at the fully differential level for longitudinally polarized $\rho_p^0, \rho_n^0, \rho_p^+, \rho_n^-$ is shown as a function of $(-u')$ in the top left, top right, bottom left and bottom right plots respectively, using $M_{\gamma\rho}^2 = 4$ GeV^2 and $S_{\gamma N} = 20\,000$ GeV^2. The same conventions as in Fig. 31 are used here. Note that the vector contributions consist of only two curves in each case, since they are insensitive to either valence or standard scenarios.

We show the relative contributions from the vector and axial GPDs to the LPA at the fully differential level in Fig. 37, as a function of $(-u')$. We choose $S_{\gamma N} = 20\,000$ GeV^2 and $M_{\gamma\rho}^2 = 4$ GeV^2 to generate the plots.

Next, the relative contributions from the vector and axial GPDs to the LPA are shown in Fig. 37. $S_{\gamma N} = 20\,000$ GeV^2 and $M_{\gamma\rho}^2 = 4$ GeV^2 are used to generate the plots. As before, the axial GPD contributions using the standard and valence scenarios are significantly different, while the DA model has little effect on the LPA. Similar comments as before apply.

Finally, the relative contributions to the LPA from the u-quark and d-quark GPDs are shown in Fig. 38 as a function of $(-u')$. The kinematical values used to generate the plots are $S_{\gamma N} = 20\,000$ GeV^2 and $M_{\gamma\rho}^2 = 4$ GeV^2.

The LPA at the single differential level is shown in Fig. 39 as a function of $M_{\gamma\rho}^2$ for different values of $S_{\gamma N}$. The three values of $S_{\gamma N}$ chosen are 800, 4000 and 20\,000 GeV^2 corresponding to the brown, green and blue curves respectively. We observe that the behavior of the LPA is very similar to the one for COMPASS kinematics in Fig. 28.

To conclude this section, the LPA, computed after integration over the differential variables, is shown as a function of $S_{\gamma N}$ in Fig. 40. Again, we note that the behavior of the LPA is very similar to the one corresponding to COMPASS kinematics; see Fig. 29.

F. Counting rates

1. JLab

At JLab, to calculate the photon flux, we use the Weizsäcker-Williams distribution. The details of the formulas used are found in Appendix D. 1 of Ref. [1].

The lepton beam at JLab forces one to also consider Bethe-Heitler-type processes. However, such contributions are suppressed with respect to the photoproduction mechanism studied here; see Ref. [13].

The angular coverage of the final-state particles is in principle a potential experimental issue. It can be shown that the angular distribution of the outgoing photon at JLab Hall B, which might evade detection, does not affect our predictions. The discussion on this subject is presented in Appendix B.
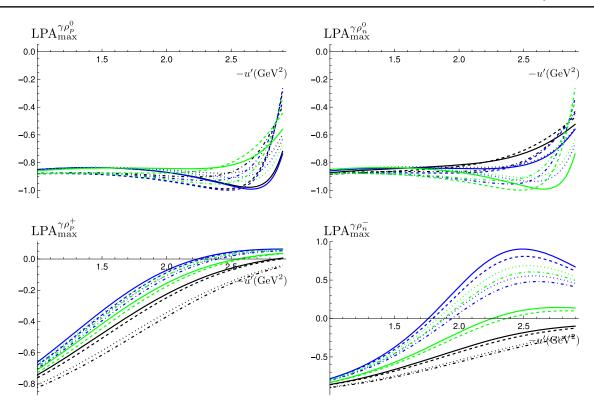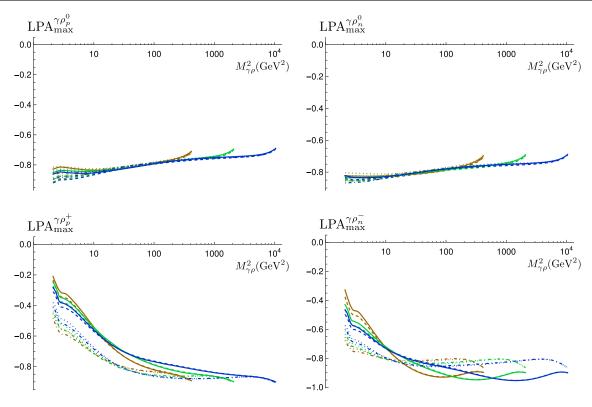
FIG. 38. The LPA at the fully differential level for longitudinally polarized $\rho_p^0, \rho_n^0, \rho_p^+, \rho_n^-$ is shown as a function of $(-u')$ in the top left, top right, bottom left and bottom right plots respectively, using $M_{\gamma\rho}^2 = 4$ GeV^2 and $S_{\gamma N} = 20\,000$ GeV^2. The blue and green curves correspond to contributions from the u-quark (H_u and $\tilde{H}_u$) and d-quark (H_d and $\tilde{H}_d$) GPDs respectively. The black curves correspond to the total contribution. The same conventions as in Fig. 32 are used here.

FIG. 39. The LPA at the single differential level for longitudinally polarized $\rho_p^0, \rho_n^0, \rho_p^+, \rho_n^-$ is shown as a function of $M_{\gamma\rho}^2$ in the top left, top right, bottom left and bottom right plots respectively. The brown, green and blue curves correspond to $S_{\gamma N} = 800$, 4000 and 20 000 GeV^2. The same color and line style conventions as in Fig. 33 are used here. Note that a log scale is used for the horizontal axis.
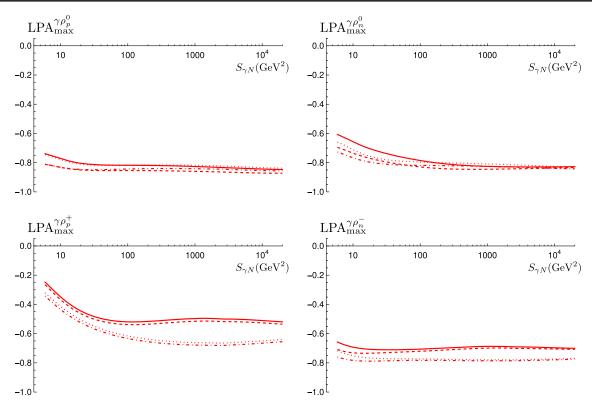
FIG. 40.   The LPA integrated over all differential variables for longitudinally polarized $\rho_p^0, \rho_n^0, \rho_p^+, \rho_n^-$ is shown in the top left, top right, bottom left and bottom right plots respectively as a function of $S_{\gamma N}$. The same color and line style conventions as in Fig. 34 are used here.

The counting rates expected at JLab for our process are shown in Table I, assuming a luminosity of 100 nb^{-1} s^{-1}, and 100 days of data-taking. The minimum and maximum values of the counting rates correspond to the boundaries obtained by considering all four different possibilities, i.e. the two models for the GPDs (standard and valence scenarios) and the two models for the DAs (asymptotic and holographic DA). The smallest value is in general obtained for an asymptotic DA with a valence scenario GPD model, while the largest value is obtained for a holographic DA with a standard scenario GPD model. The values obtained for the JLab experiment are very promising.

2. COMPASS

At COMPASS, one again uses the Weizsäcker-Williams distribution to obtain the photon flux from the muon beam. Here, we also fix $Q_{\max}^2 = 0.1$ GeV^2.

The counting rates expected at COMPASS for our process are shown in Table II. Like before, the minimum and maximum values of the counting rates correspond to the boundaries obtained by considering all the different possibilities, i.e. the two models for the GPDs (standard and valence scenarios) and the two models for the DAs (asymptotic and holographic DA). In general, the lowest value is obtained for an asymptotic DA with the valence

TABLE I.   Estimated counting rates at JLab for $\gamma\rho$ photoproduction.

GPD	Meson	Counting rates
Chiral-even	ρ_p^0	1.3–2.4×10^5
	ρ_n^0	1.7–4.0×10^4
	ρ_p^+	0.9–1.4×10^5
	ρ_n^-	0.3–1.8×10^5
Chiral-odd	ρ_p^0	2.1–4.2×10^4
	ρ_n^0	1.0–2.6×10^4
	ρ_p^+	3.5–6.7×10^4
	ρ_n^-	3.5–6.8×10^4

TABLE II.   Estimated counting rates at COMPASS for $\gamma\rho$ photoproduction.

GPD	Meson	Counting rates
Chiral-even	ρ_p^0	0.7–1.2×10^3
	ρ_n^0	0.8–2.1×10^2
	ρ_p^+	3.6–7.4×10^2
	ρ_n^-	3.0–8.1×10^2
Chiral-odd	ρ_p^0	75–152
	ρ_n^0	36–98
	ρ_p^+	135–257
	ρ_n^-	133–257

TABLE III. Estimated counting rates at EIC kinematics for $\gamma\rho$ photoproduction.

GPD	Meson	Total counting rates	Counting rates with $S_{\gamma N} > 300$ GeV^2
Chiral-even	ρ_p^0	1.3–2.4×10^4	0.6–1.2×10^3
	ρ_n^0	1.7–4.3×10^3	1.3–2.4×10^2
	ρ_p^+	0.7–1.5×10^4	3.1–9.3×10^2
	ρ_n^-	0.6–1.6×10^4	2.0–9.1×10^2
Chiral-odd	ρ_p^0	1.2–2.4×10^3	
	ρ_n^0	0.6–1.5×10^3	
	ρ_p^+	2.1–4.2×10^3	
	ρ_n^-	2.1–4.1×10^3	

TABLE IV. Estimated counting rates at p-Pb UPCs at LHC for $\gamma\rho$ photoproduction.

GPD	Meson	Total counting rates	Counting rates with $S_{\gamma N} > 300$ GeV^2
Chiral-even	ρ_p^0	0.9–1.6×10^4	4.1–8.1×10^2
	ρ_p^+	0.5–1.1×10^4	2.1–6.4×10^2
Chiral-odd	ρ_p^0	0.8–1.7×10^3	
	ρ_p^+	1.5–2.9×10^3	

scenario, while the largest value is obtained for a holographic DA with the standard scenario. We assume a luminosity of 0.1 nb^{-1} s^{-1}, and 300 days of data-taking.

3. EIC

The counting rates for EIC, assuming a total integrated luminosity of 10^7 nb^{-1}, are shown in Table III. In particular, we use the highest expected electron-nucleon center-of-mass energy, corresponding to $S_{eN} = 19\,600$ GeV^2 [21]. Since the center-of-mass energies available at EIC are high enough, one can study the kinematic region where the skewness ξ is small. Therefore, we also show the counting rates with the constraint that $S_{\gamma N} > 300$ GeV^2, which corresponds roughly to $\xi \lesssim 5 \times 10^{-3}$.[15] In fact, values of the skewness ξ as small as 7.5×10^{-6} can be probed. By imposing the cut in $S_{\gamma N}$, the counting rates decrease by a factor of roughly 20 in the chiral-even case. This significant decrease is due to the fact that the peak of the cross section is located at low $S_{\gamma N}$, roughly 20 GeV^2, as can be seen in Figs. 23 and 34. In the chiral-odd case, the region of small ξ is heavily suppressed, since the cross section is multiplied by a factor of ξ^2, compared to the chiral-even case; see Eqs. (4.37) and (4.62). As a result, we do not show the counting rates for the chiral-odd case when imposing the $S_{\gamma N} > 300$ GeV^2 cut. The minimum and maximum values for the counting rates in Table III are obtained as described in previous sections.

4. Ultraperipheral collisions at LHC

In UPCs, the beam and target are far enough apart such that there are no hadronic interactions between them, such that the nucleus/proton interacts by the exchange of photons. In particular, heavy nuclei, such as lead, can

act as a good source of photons, since the photon flux scales as Z^2, where Z is the charge of the nucleus. The details on how the photon flux is obtained can be found in Appendix D.2 of Ref. [1].

The counting rates corresponding to p-Pb UPCs at the LHC, assuming an integrated luminosity of 1200 nb^{-1}, are shown in Table IV. This corresponds to the expected data taking for runs 3 and 4 [25]. As in Sec. V F 3, there is an order-of-magnitude drop in the counting rates for the chiral-even case when a cut of $S_{\gamma N} > 300$ GeV^2 is imposed. The chiral-odd counting rates are also very small when the $S_{\gamma N} > 300$ GeV^2 cut is applied, and they are thus omitted from Table IV.

VI. CONCLUSION

In this work, we extended the analysis of the $\gamma N \to \gamma\rho^0 N'$ process introduced in Ref. [13] by including the linear polarization asymmetries, extending the kinematics to selected future experiments (COMPASS, EIC and UPCs at the LHC), computing predictions for an alternative "holographic" DA [Eq. (3.9)] and considering charged ρ mesons. Since we considered the large-angle scattering kinematics, which amounts to large $(-u')$ and $M_{\gamma\rho}^2$, and small $(-t)$, we were able to employ the collinear factorization. In fact, QCD factorization has been recently proven to hold for a family of $2 \to 3$ exclusive processes [11,12], which includes our process, for large $|\vec{p}_t|$. We found that imposing kinematical cuts on $(-u')$, $(-t')$ and $(-t)$ in Eq. (2.14) is sufficient to push the $\rho N'$ invariant mass above the resonance region.

Our results show that the exclusive photoproduction of a $\gamma\rho$ pair provides another interesting channel to study GPDs, besides the extensively studied channels such as DVCS, Deeply Virtual Meson Production (DVMP) and Timelike Compton Scattering (TCS). We have estimated the counting rates at various experiments in Sec. V F, and the values obtained are promising, especially at JLab where they were found to be of the order of 10^5, assuming a luminosity of 100 nb^{-1} s^{-1}, and 100 days of data-taking. In fact, the GPD model corresponding to the standard scenario, which is favored by lattice results [26], as well as its recent update in Ref. [27], gives larger cross sections in general. Furthermore, we found that the linear polarization

---

[15]Note that the relation between $S_{\gamma N}$ and ξ involves $M_{\gamma\rho}^2$, which is why a cut in $S_{\gamma N}$ does not directly correspond to a cut in ξ. However, as can be seen in Sec. V E 2, the cross section is dominated by small $M_{\gamma\rho}^2$, so the region of small ξ is actually the one where most of the contribution comes from.

asymmetries with respect to the incoming photon are sizable. Moreover, by exploiting the high energies available at EIC and UPCs at the LHC, one is able to probe GPDs in the region of small skewness ξ, a region where very little is known about GPDs. We found that by restricting the kinematics to the region of $\xi \leq 5 \times 10^{-3}$, the counting rates drop by a factor of roughly 10, which still leaves sufficient statistics.

We intend to extend the present computation by including next-to-leading-order corrections in α_s. While QCD collinear factorization was proved for our process, the knowledge of such corrections, which are often significant for phenomenology, will increase the precision of our predictions and will give us the opportunity to estimate the uncertainties related to our process based on the collinear factorization approach.

ACKNOWLEDGMENTS

APPENDIX A: CHIRAL-ODD AMPLITUDES

For the chiral-odd case, diagrams A_3 and A_4 contribute to the structure $T^i_{A\perp}$ while diagrams B_1 and B_5 contribute to the structure $T^i_{B\perp}$. Thus,

$$N^q_{TA}[(AB)_{123}] \equiv N^q_{TA}[A_3], \qquad (A1)$$

$$N^q_{TA}[(AB)_{45}] \equiv N^q_{TA}[A_4], \qquad (A2)$$

$$N^q_{TB}[(AB)_{123}] \equiv N^q_{TB}[B_1], \qquad (A3)$$

$$N^q_{TB}[(AB)_{45}] \equiv N^q_{TB}[B_5]. \qquad (A4)$$

For convenience, we define the coefficients $T^\perp_A[A_3]$, $T^\perp_A[A_4]$, $T^\perp_B[B_1]$ and $T^\perp_B[B_5]$, given by

$$N^q_{TA}[A_3] \equiv \int_{-1}^{1} \int_0^1 T^\perp_A[A_3]\phi(z)dz H_T(x,\xi)dx, \qquad (A5)$$

$$N^q_{TA}[A_4] \equiv \int_{-1}^{1} \int_0^1 T^\perp_A[A_4]\phi(z)dz H_T(x,\xi)dx, \qquad (A6)$$

$$N^q_{TB}[B_1] \equiv \int_{-1}^{1} \int_0^1 T^\perp_B[B_1]\phi(z)dz H_T(x,\xi)dx, \qquad (A7)$$

$$N^q_{TB}[B_5] \equiv \int_{-1}^{1} \int_0^1 T^\perp_B[B_5]\phi(z)dz H_T(x,\xi)dx. \qquad (A8)$$

1. Asymptotic DA case

For the case of the asymptotic DA in Eq. (3.8), we get[16]

$$T^\perp_A[A_3]\phi^{as}(z) = -\frac{3}{\alpha^2\bar{\alpha}\xi(\xi-x-i\epsilon)(\xi+x-i\epsilon)}, \qquad (A9)$$

$$T^\perp_A[A_4]\phi^{as}(z) = \frac{3(1-z)}{\alpha^2\xi(\xi-x-i\epsilon)(\alpha(-\xi+x+i\epsilon)+(1-z)(2\xi+(1-\alpha)(-\xi+x+i\epsilon)))}, \qquad (A10)$$

$$T^\perp_B[B_1]\phi^{as}(z) = -\frac{3}{(1-\alpha)\xi(\xi-x-i\epsilon)(\xi+x+i\epsilon)}, \qquad (A11)$$

$$T^\perp_B[B_5]\phi^{as}(z) = \frac{3z}{\xi(\xi+x+i\epsilon)(\alpha(-\xi+x+i\epsilon)+(1-z)(2\xi+(1-\alpha)(-\xi+x+i\epsilon)))}. \qquad (A12)$$

The integral with respect to z is trivially performed in this case. Thus, one gets

---

[16]We note that some typos have been corrected here with respect to results in Appendix B 2 of our previous publication [13].

$$\int_0^1 T_A^\perp[A_3]\phi^{\text{as}}(z)dz = -\frac{3}{\alpha^2\bar\alpha\xi(\xi-x-i\epsilon)(\xi+x-i\epsilon)},$$

$$\int_0^1 T_A^\perp[A_4]\phi^{\text{as}}(z)dz = \frac{3}{\alpha^2\xi(\xi-x-i\epsilon)(2\xi+(1-\alpha)(-\xi+x+i\epsilon))} + \frac{3\ln\left(\frac{\xi+x+i\epsilon}{\alpha(-\xi+x+i\epsilon)}\right)}{\alpha\xi(2\xi+(1-\alpha)(-\xi+x+i\epsilon))^2}, \quad \text{(A13)}$$

$$\int_0^1 T_B^\perp[B_1]\phi^{\text{as}}(z)dz = -\frac{3}{(1-\alpha)\xi(\xi-x-i\epsilon)(\xi+x+i\epsilon)},$$

$$\int_0^1 T_B^\perp[B_5]\phi^{\text{as}}(z)dz = -\frac{3}{\xi(\xi+x+i\epsilon)(2\xi+(1-\alpha)(-\xi+x+i\epsilon))} + \frac{3\ln\left(\frac{\xi+x+i\epsilon}{\alpha(-\xi+x+i\epsilon)}\right)}{\xi(2\xi+(1-\alpha)(-\xi+x+i\epsilon))^2}. \quad \text{(A14)}$$

Let us note that the last term in the previous expressions (A13) and (A14) might seem to have a double pole when $x = -\frac{1+\alpha}{\bar\alpha}\xi - i\epsilon$. However, the logarithm cancels under such conditions, so this pole is actually a simple pole.

Using Eqs. (A5) to (A8), we can write the integrals with respect to x in terms of building block integrals, given in Appendix D of Ref. [14]. Thus, we have

$$N_{TA}^q[A_3] = \frac{3}{2\alpha^2\bar\alpha\xi^2}(I_e - I_g), \quad \text{(A15)}$$

$$N_{TA}^q[A_4] = -\frac{3}{\alpha^2\xi}I_a + \frac{3}{\alpha\xi}I_d, \quad \text{(A16)}$$

$$N_{TB}^q[B_1] = \frac{3}{2\bar\alpha\xi^2}(I_e - I_f), \quad \text{(A17)}$$

$$N_{TB}^q[B_5] = -\frac{3}{\xi}I_l + \frac{3}{\xi}I_d. \quad \text{(A18)}$$

For symmetric GPDs, we have

$$N_{TA}^q[A_3]^s = \frac{3}{2\alpha^2\bar\alpha\xi^2}(2I_e), \quad \text{(A19)}$$

$$N_{TA}^q[A_4]^s = -\frac{3}{\alpha^2\xi}\left(\frac{1}{2\xi}I_e - \frac{\bar\alpha}{2\xi}I_i\right) + \frac{3}{\alpha\xi}I_d, \quad \text{(A20)}$$

$$N_{TB}^q[B_1]^s = \frac{3}{2\bar\alpha\xi^2}(I_e + \bar I_e), \quad \text{(A21)}$$

$$N_{TB}^q[B_5]^s = -\frac{3}{\xi}\left(-\frac{1}{2\alpha\xi}\bar I_e - \frac{\bar\alpha}{2\alpha\xi}I_i\right) + \frac{3}{\xi}I_d. \quad \text{(A22)}$$

For antisymmetric GPDs, we have

$$N_{TA}^q[A_3]^a = 0, \quad \text{(A23)}$$

$$N_{TA}^q[A_4]^a = -\frac{3}{\alpha^2\xi}\left(\frac{1}{2\xi}I_e - \frac{\bar\alpha}{2\xi}I_i\right) + \frac{3}{\alpha\xi}I_d, \quad \text{(A24)}$$

$$N_{TB}^q[B_1]^a = \frac{3}{2\bar\alpha\xi^2}(I_e - \bar I_e), \quad \text{(A25)}$$

$$N_{TB}^q[B_5]^a = -\frac{3}{\xi}\left(\frac{1}{2\alpha\xi}\bar I_e - \frac{\bar\alpha}{2\alpha\xi}I_i\right) + \frac{3}{\xi}I_d. \quad \text{(A26)}$$

So, only the building block integrals I_e, I_i and I_d are needed in the asymptotical DA case.

2. Holographic DA case

Here, we essentially repeat the above steps, but with a holographic DA whose form is given in Eq. (3.9), instead of an asymptotic DA. For the contributions to diagrams A_3 and B_1, the same results as in the asymptotic DA case can be used, with a change of the overall prefactor from 6 to 8; see Eqs. C.3 and C.4 in Ref. [1]. Therefore, we only focus on the results for the A_4 and B_5 diagrams here. The results, in terms of the building block integrals given in Appendix D of Ref. [14] and Appendix C of Ref. [1], read

$$N_{TA}^q[A_4] \equiv s^3 \int_{-1}^1 \int_0^1 T_A^\perp[A_4]\phi^{\text{hol}}(z)dz H_T(x,\xi)dx$$
$$= -\frac{4}{\alpha^2\xi}\left[\frac{1}{2\xi}I_e - \sqrt{\alpha}\chi_a\right], \quad \text{(A27)}$$

$$N_{TB}^q[B_5] \equiv s^3 \int_{-1}^1 \int_0^1 T_B^\perp[B_5]\phi^{\text{hol}}(z)dz H_T(x,\xi)dx$$
$$= \frac{4}{\xi}\left[-\frac{1}{2\alpha\xi}I_f + \frac{1}{\sqrt{\alpha}}\chi_a\right]. \quad \text{(A28)}$$

For symmetric GPDs, we have

$$N_{TA}^q[A_4]^s \equiv s^3 \int_{-1}^1 \int_0^1 T_A^\perp[A_4]^s\phi^{\text{hol}}(z)dz H_T(x,\xi)dx$$
$$= -\frac{4}{\alpha^2\xi}\left[\frac{1}{2\xi}I_e - \sqrt{\alpha}\chi_a\right], \quad \text{(A29)}$$

$$N_{TB}^q[B_5]^s \equiv s^3 \int_{-1}^1 \int_0^1 T_B^\perp[B_5]^s \phi^{\text{hol}}(z) dz H_T(x,\xi) dx$$
$$= \frac{4}{\xi} \left[\frac{1}{2\alpha\xi} \bar{I}_e + \frac{1}{\sqrt{\alpha}} \chi_a \right], \tag{A30}$$

and for antisymmetric GPDs, we have

$$N_{TA}^q[A_4]^a \equiv s^3 \int_{-1}^1 \int_0^1 T_A^\perp[A_4]^a \phi^{\text{hol}}(z) dz H_T(x,\xi) dx$$
$$= -\frac{4}{\alpha^2 \xi} \left[\frac{1}{2\xi} I_e - \sqrt{\alpha} \chi_a \right], \tag{A31}$$

$$N_{TB}^q[B_5]^a \equiv s^3 \int_{-1}^1 \int_0^1 T_B^\perp[B_5]^a \phi^{\text{hol}}(z) dz H_T(x,\xi) dx$$
$$= \frac{4}{\xi} \left[-\frac{1}{2\alpha\xi} \bar{I}_e + \frac{1}{\sqrt{\alpha}} \chi_a \right]. \tag{A32}$$

So, only the extra building block integral χ_a is needed.

APPENDIX B: EFFECT OF ANGULAR CUTS ON THE OUTGOING PHOTON AT JLab

In this appendix, we show the influence of angular cuts on the outgoing photon at JLab on the cross section.

1. Angular distribution

The derivation of the angular distribution was performed in Appendix E in Ref. [13], and we do not repeat the details here. However, for the sake of completeness, we reproduce here the relevant results.

We require the outgoing photon scattering angle in the rest frame of the nucleon target. This angle θ is defined with respect to the direction of the incoming photon (i.e. θ is the angle that the outgoing photon makes with the $-z$ axis in the nucleon rest frame). The angle θ satisfies

$$\tan\theta = -\frac{2Ms(1+\xi)\alpha|\vec{p}_t - \frac{\vec{\Delta}_t}{2}|}{-\alpha^2(1+\xi)^2 s^2 + (\vec{p}_t - \frac{\vec{\Delta}_t}{2})^2 M^2}. \tag{B1}$$

From the relation $\alpha = M_{\gamma\rho}^2/(-u')$ [see Eq. (2.17)], one can express $\tan\theta$ as a function of $-u'$. To solve for θ in Eq. (B1), one should take

$$\theta = \arctan(\tan\theta), \quad \text{for } \tan\theta > 0, \tag{B2}$$

$$\theta = \pi + \arctan(\tan\theta), \quad \text{for } \tan\theta < 0, \tag{B3}$$

since θ is positive. Setting $\vec{\Delta}_t = 0$, Eq. (B1) simplifies to

$$\tan\theta = -\frac{2Ms(1+\xi)\alpha|\vec{p}_t|}{-\alpha^2(1+\xi)^2 s^2 + \vec{p}_t^2 M^2}, \tag{B4}$$

and using the definition of the kinematical variables in Sec. II, one can obtain α in terms of θ,

$$\alpha = \frac{(1+\xi+\tilde{\tau})\tilde{\tau}\tan^2\theta + a\left(1 + \sqrt{1+\tan^2\theta}\right)}{(1+\xi+\tilde{\tau})^2 \tan^2\theta + 2a},$$
$$\text{for } \tan\theta > 0, \tag{B5}$$

$$\alpha = \frac{(1+\xi+\tilde{\tau})\tilde{\tau}\tan^2\theta + a\left(1 - \sqrt{1+\tan^2\theta}\right)}{(1+\xi+\tilde{\tau})^2 \tan^2\theta + 2a},$$
$$\text{for } \tan\theta < 0, \tag{B6}$$

where

$$a = \frac{4M_{\gamma\rho}^2}{s}, \qquad \tilde{\tau} = \frac{2\xi}{1+\xi}\frac{M_{\gamma\rho}^2}{s} = \tau\frac{M_{\gamma\rho}^2}{s}. \tag{B7}$$

This thus allows us to obtain $(-u')$ as a function of θ using $-u' = \alpha M_{\gamma\rho}^2$; see Eq. (2.17). Writing

$$\tan\theta = f(-u'), \tag{B8}$$

the angular distribution can be obtained from the fully differential cross section through

$$\frac{1}{\sigma}\frac{d\sigma}{d\theta} = \frac{1}{\sigma}\frac{d\sigma}{d(-u')}\frac{1 + f^2(-u'[\theta])}{f'(-u'[\theta])}. \tag{B9}$$

The obtained angular distribution in the chiral-even case is shown in Figs. 41, 42, 43 and 44 for $\rho_p^0, \rho_n^0, \rho_p^+$ and ρ_n^- respectively. Similarly, the obtained angular distribution in the chiral-odd case is shown in Figs. 45, 46, 47 and 48 for $\rho_p^0, \rho_n^0, \rho_p^+$ and ρ_n^- respectively. Each figure has three plots, corresponding to three different values of $S_{\gamma N}$, namely $10, 15, 20$ GeV^2. Finally, in each plot, two or three different curves are shown, which correspond to different $M_{\gamma\rho}^2$. The asymptotic DAs with the standard GPD scenario are used to generate the plots.

In the chiral-even case, the obtained angular distribution increases with θ for ρ_p^0 and ρ_n^0, while in the chiral-odd case,
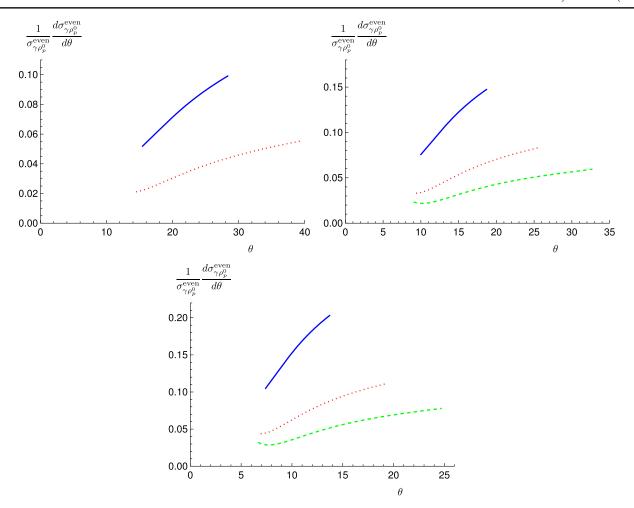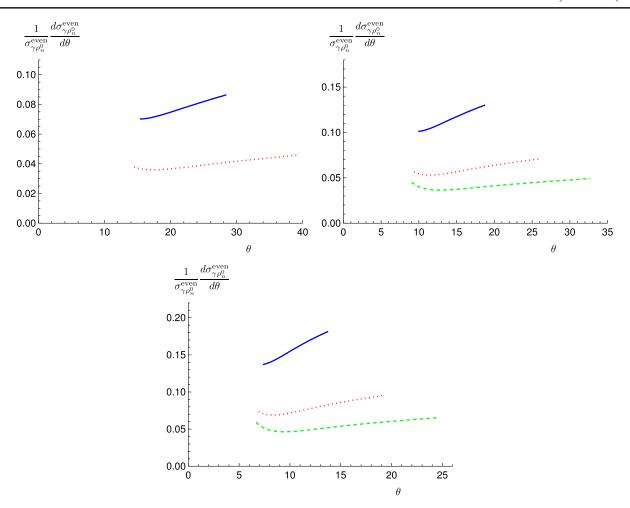
FIG. 41. Angular distribution in the chiral-even case for $\gamma\rho_p^0$ photoproduction. Upper left: $S_{\gamma N} = 10\,\text{GeV}^2$, for $M^2_{\gamma\rho_p^0} = 3\,\text{GeV}^2$ (solid blue) and $M^2_{\gamma\rho_p^0} = 4$ GeV^2 (dotted red). Upper right: $S_{\gamma N} = 15$ GeV^2, for $M^2_{\gamma\rho_p^0} = 3.5$ GeV^2 (solid blue), $M^2_{\gamma\rho_p^0} = 5$ GeV^2 (dotted red) and $M^2_{\gamma\rho_p^0} = 6.5$ GeV^2 (dashed green). Bottom: $S_{\gamma N} = 20$ GeV^2, for $M^2_{\gamma\rho_p^0} = 4$ GeV^2 (solid blue), $M^2_{\gamma\rho_p^0} = 6$ GeV^2 (dotted red) and $M^2_{\gamma\rho_p^0} = 8$ GeV^2 (dashed green).
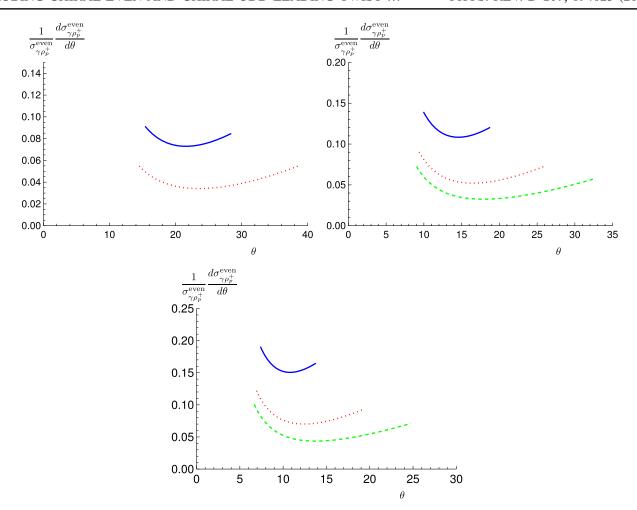
FIG. 42. Angular distribution in the chiral-even case for $\gamma \rho_n^0$ photoproduction. Upper left: $S_{\gamma N} = 10 \, \text{GeV}^2$, for $M^2_{\gamma \rho_n^0} = 3 \, \text{GeV}^2$ (solid blue) and $M^2_{\gamma \rho_n^0} = 4$ GeV^2 (dotted red). Upper right: $S_{\gamma N} = 15$ GeV^2, for $M^2_{\gamma \rho_n^0} = 3.5$ GeV^2 (solid blue), $M^2_{\gamma \rho_n^0} = 5$ GeV^2 (dotted red) and $M^2_{\gamma \rho_n^0} = 6.5$ GeV^2 (dashed green). Bottom: $S_{\gamma N} = 20$ GeV^2, for $M^2_{\gamma \rho_n^0} = 4$ GeV^2 (solid blue), $M^2_{\gamma \rho_n^0} = 6$ GeV^2 (dotted red) and $M^2_{\gamma \rho_n^0} = 8$ GeV^2 (dashed green).
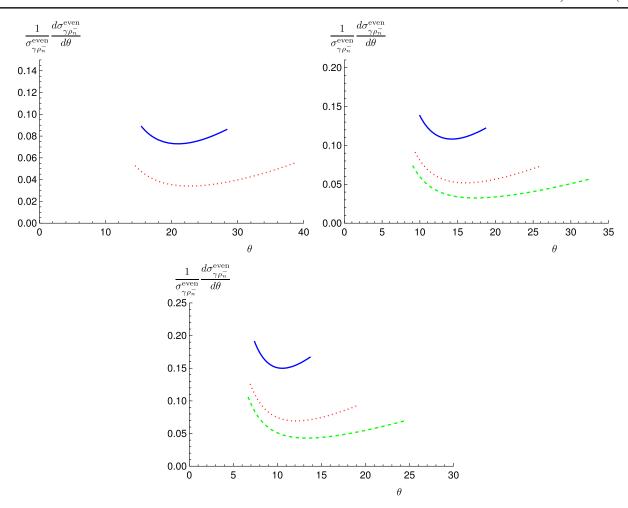
FIG. 43.　Angular distribution in the chiral-even case for $\gamma \rho_p^+$ photoproduction. Upper left: $S_{\gamma N} = 10\,\text{GeV}^2$, for $M^2_{\gamma \rho_p^+} = 3\,\text{GeV}^2$ (solid blue) and $M^2_{\gamma \rho_p^+} = 4$ GeV^2 (dotted red). Upper right: $S_{\gamma N} = 15$ GeV^2, for $M^2_{\gamma \rho_p^+} = 3.5$ GeV^2 (solid blue), $M^2_{\gamma \rho_p^+} = 5$ GeV^2 (dotted red) and $M^2_{\gamma \rho_p^+} = 6.5$ GeV^2 (dashed green). Bottom: $S_{\gamma N} = 20$ GeV^2, for $M^2_{\gamma \rho_p^+} = 4$ GeV^2 (solid blue), $M^2_{\gamma \rho_p^+} = 6$ GeV^2 (dotted red) and $M^2_{\gamma \rho_p^+} = 8$ GeV^2 (dashed green).
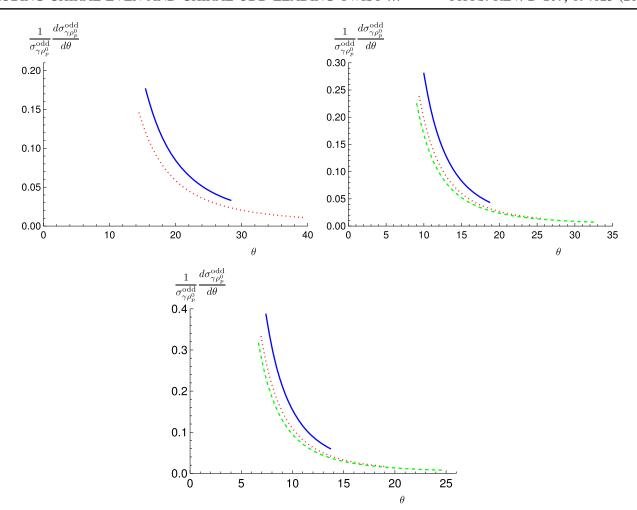
FIG. 44. Angular distribution in the chiral-even case for $\gamma\rho_n^-$ photoproduction. Upper left: $S_{\gamma N} = 10\,\text{GeV}^2$, for $M_{\gamma\rho_n^-}^2 = 3\,\text{GeV}^2$ (solid blue) and $M_{\gamma\rho_n^-}^2 = 4$ GeV^2 (dotted red). Upper right: $S_{\gamma N} = 15$ GeV^2, for $M_{\gamma\rho_n^-}^2 = 3.5$ GeV^2 (solid blue), $M_{\gamma\rho_n^-}^2 = 5$ GeV^2 (dotted red) and $M_{\gamma\rho_n^-}^2 = 6.5$ GeV^2 (dashed green). Bottom: $S_{\gamma N} = 20$ GeV^2, for $M_{\gamma\rho_n^-}^2 = 4$ GeV^2 (solid blue), $M_{\gamma\rho_n^-}^2 = 6$ GeV^2 (dotted red) and $M_{\gamma\rho_n^-}^2 = 8$ GeV^2 (dashed green).
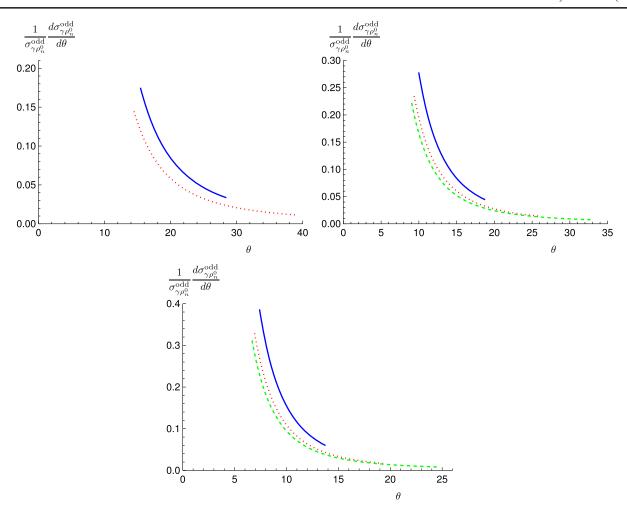
FIG. 45. Angular distribution in the chiral-odd case for $\gamma\rho_p^0$ photoproduction. Upper left: $S_{\gamma N} = 10\,\text{GeV}^2$, for $M^2_{\gamma\rho_p^0} = 3\,\text{GeV}^2$ (solid blue) and $M^2_{\gamma\rho_p^0} = 4$ GeV^2 (dotted red). Upper right: $S_{\gamma N} = 15$ GeV^2, for $M^2_{\gamma\rho_p^0} = 3.5$ GeV^2 (solid blue), $M^2_{\gamma\rho_p^0} = 5$ GeV^2 (dotted red) and $M^2_{\gamma\rho_p^0} = 6.5$ GeV^2 (dashed green). Bottom: $S_{\gamma N} = 20$ GeV^2, for $M^2_{\gamma\rho_p^0} = 4$ GeV^2 (solid blue), $M^2_{\gamma\rho_p^0} = 6$ GeV^2 (dotted red) and $M^2_{\gamma\rho_p^0} = 8$ GeV^2 (dashed green).
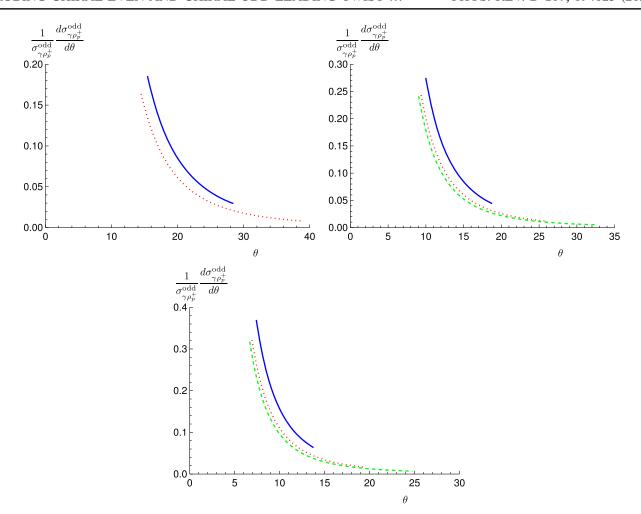
FIG. 46. Angular distribution in the chiral-odd case for $\gamma\rho_n^0$ photoproduction. Upper left: $S_{\gamma N} = 10 \, \text{GeV}^2$, for $M^2_{\gamma\rho_n^0} = 3 \, \text{GeV}^2$ (solid blue) and $M^2_{\gamma\rho_n^0} = 4 \, \text{GeV}^2$ (dotted red). Upper right: $S_{\gamma N} = 15 \, \text{GeV}^2$, for $M^2_{\gamma\rho_n^0} = 3.5 \, \text{GeV}^2$ (solid blue), $M^2_{\gamma\rho_n^0} = 5 \, \text{GeV}^2$ (dotted red) and $M^2_{\gamma\rho_n^0} = 6.5 \, \text{GeV}^2$ (dashed green). Bottom: $S_{\gamma N} = 20 \, \text{GeV}^2$, for $M^2_{\gamma\rho_n^0} = 4 \, \text{GeV}^2$ (solid blue), $M^2_{\gamma\rho_n^0} = 6 \, \text{GeV}^2$ (dotted red) and $M^2_{\gamma\rho_n^0} = 8 \, \text{GeV}^2$ (dashed green).

FIG. 47. Angular distribution in the chiral-odd case for $\gamma\rho_p^+$ photoproduction. Upper left: $S_{\gamma N} = 10\,\text{GeV}^2$, for $M^2_{\gamma\rho_p^+} = 3\,\text{GeV}^2$ (solid blue) and $M^2_{\gamma\rho_p^+} = 4\,\text{GeV}^2$ (dotted red). Upper right: $S_{\gamma N} = 15\,\text{GeV}^2$, for $M^2_{\gamma\rho_p^+} = 3.5\,\text{GeV}^2$ (solid blue), $M^2_{\gamma\rho_p^+} = 5\,\text{GeV}^2$ (dotted red) and $M^2_{\gamma\rho_p^+} = 6.5\,\text{GeV}^2$ (dashed green). Bottom: $S_{\gamma N} = 20\,\text{GeV}^2$, for $M^2_{\gamma\rho_p^+} = 4\,\text{GeV}^2$ (solid blue), $M^2_{\gamma\rho_p^+} = 6\,\text{GeV}^2$ (dotted red) and $M^2_{\gamma\rho_p^+} = 8\,\text{GeV}^2$ (dashed green).
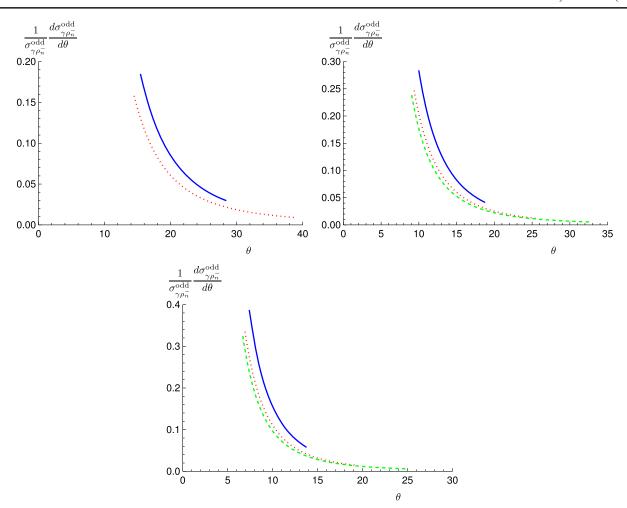
FIG. 48. Angular distribution in the chiral-odd case for $\gamma\rho_n^-$ photoproduction. Upper left: $S_{\gamma N} = 10\,\text{GeV}^2$, for $M^2_{\gamma\rho_n^-} = 3\,\text{GeV}^2$ (solid blue) and $M^2_{\gamma\rho_n^-} = 4\,\text{GeV}^2$ (dotted red). Upper right: $S_{\gamma N} = 15\,\text{GeV}^2$, for $M^2_{\gamma\rho_n^-} = 3.5\,\text{GeV}^2$ (solid blue), $M^2_{\gamma\rho_n^-} = 5\,\text{GeV}^2$ (dotted red) and $M^2_{\gamma\rho_n^-} = 6.5\,\text{GeV}^2$ (dashed green). Bottom: $S_{\gamma N} = 20\,\text{GeV}^2$, for $M^2_{\gamma\rho_n^-} = 4\,\text{GeV}^2$ (solid blue), $M^2_{\gamma\rho_n^-} = 6\,\text{GeV}^2$ (dotted red) and $M^2_{\gamma\rho_n^-} = 8\,\text{GeV}^2$ (dashed green).
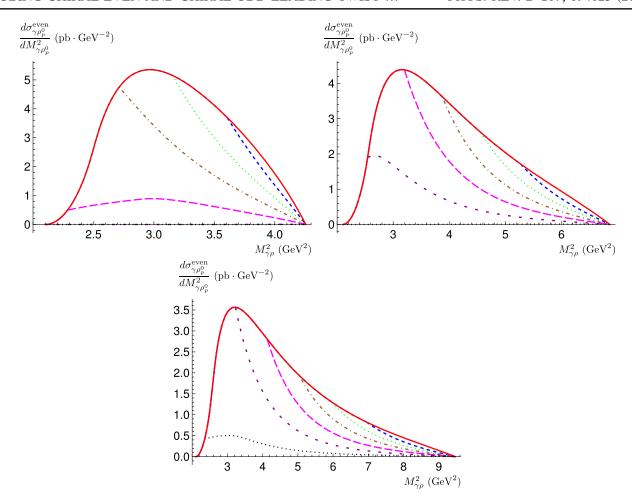
FIG. 49. The chiral-even single-differential cross section as a function of $M^2_{\gamma\rho}$ for $\gamma\rho^0_p$ photoproduction. Solid red: no angular cut. Other curves show the effect of an upper angular cut θ for the outgoing γ: 35° (dashed blue), 30° (dotted green), 25° (dashed-dotted brown), 20° (long-dashed magenta), 15° (short-dashed purple) and 10° (dotted black). Upper left: $S_{\gamma N} = 10$ GeV^2. Upper right: $S_{\gamma N} = 15$ GeV^2. Bottom: $S_{\gamma N} = 20$ GeV^2.

it decreases with θ for all of $\rho^0_p, \rho^0_n, \rho^+_p, \rho^-_n$. In all cases, the distributions are dominated by moderate values of θ. In practice, at JLab Hall B, the outgoing photon could be detected with an angle between 5° and 35° from the incoming beam. Therefore, we find that relatively few events will be lost at JLab due to the angular cut on the outgoing photon.

2. Single-differential cross section

In this subsection, we show the effect of choosing different angular cuts on the single-differential cross section, as a function of $M^2_{\gamma\rho}$. For the chiral-even case, this is shown in Figs. 49, 50, 51 and 52 for $\rho^0_p, \rho^0_n, \rho^+_p$ and ρ^-_n respectively, while for the chiral-odd case, this is shown in Figs. 53, 54, 55 and 56 for $\rho^0_p, \rho^0_n, \rho^+_p$ and ρ^-_n respectively.

Each figure consists of three plots, which correspond to three different values of $S_{\gamma N}$, namely 10,15 and 20 GeV^2. Each plot consists of seven curves, which correspond to six different angular cuts of 10°, 15°, 20°, 25°, 30°, 35°, and one with no angular cuts. The asymptotic DAs with the standard GPD scenario are used to generate the plots.

From the figures, we find that the angular cuts mainly affect the low $S_{\gamma N}$ domain. For the specific case of the JLab 35° upper cut (dashed-blue), the effect is negligible for both the chiral-even and chiral-odd cases.

Moreover, we note that by using cuts on θ, it is possible to significantly reduce the contribution of the chiral-even contribution, in particular in the high-$S_{\gamma N}$ region, while moderately reducing the chiral-odd contribution. Putting additional cuts on $M^2_{\gamma\rho}$, like $M^2_{\gamma\rho} > 6$ GeV^2, would allow for an increase in the ratio of odd cross section to even cross section.
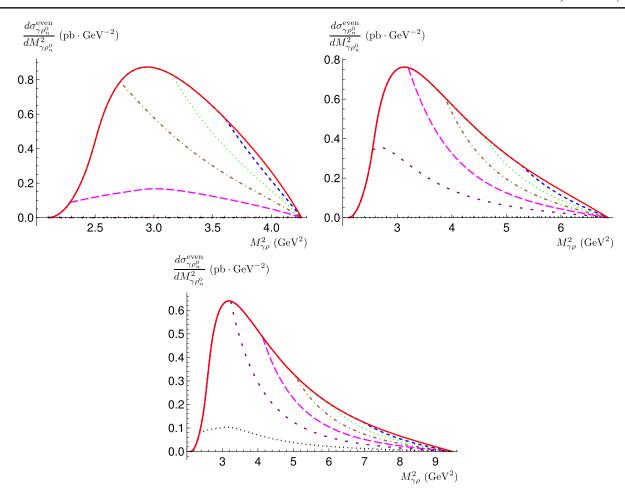
FIG. 50. The chiral-even single-differential cross section as a function of $M^2_{\gamma\rho}$ for $\gamma\rho^0_n$ photoproduction. Solid red: no angular cut. Other curves show the effect of an upper angular cut θ for the outgoing γ: 35° (dashed blue), 30° (dotted green), 25° (dashed-dotted brown), 20° (long-dashed magenta), 15° (short-dashed purple) and 10° (dotted black). Upper left: $S_{\gamma N} = 10$ GeV^2. Upper right: $S_{\gamma N} = 15$ GeV^2. Bottom: $S_{\gamma N} = 20$ GeV^2.
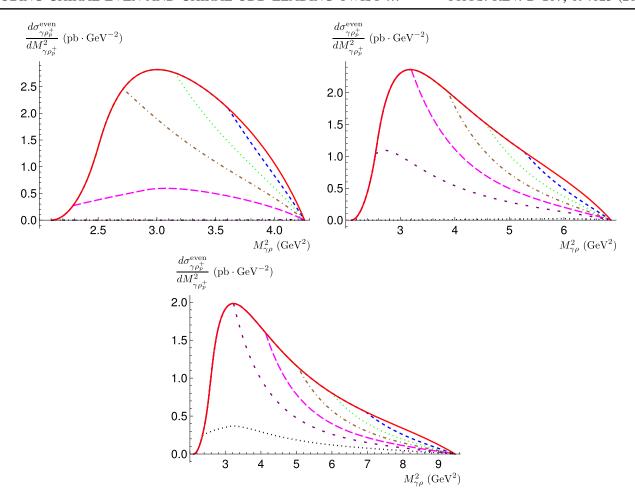
FIG. 51.   The chiral-even single-differential cross section as a function of $M^2_{\gamma\rho}$ for $\gamma\rho^+_p$ photoproduction. Solid red: no angular cut. Other curves show the effect of an upper angular cut θ for the outgoing γ: 35° (dashed blue), 30° (dotted green), 25° (dashed-dotted brown), 20° (long-dashed magenta), 15° (short-dashed purple) and 10° (dotted black). Upper left: $S_{\gamma N} = 10$ GeV^2. Upper right: $S_{\gamma N} = 15$ GeV^2. Bottom: $S_{\gamma N} = 20$ GeV^2.
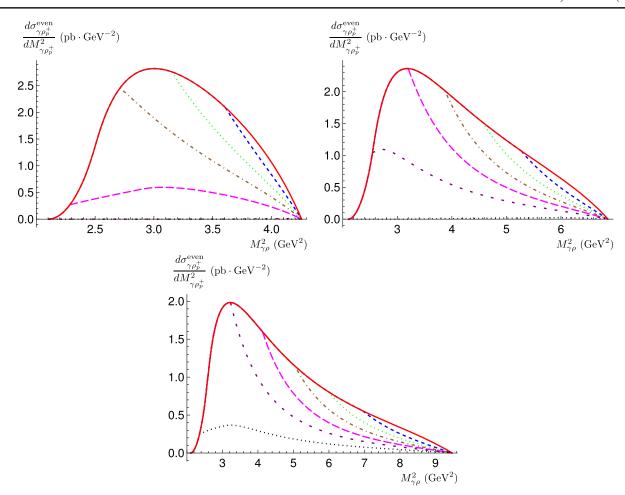
FIG. 52.   The chiral-even single-differential cross section as a function of $M_{\gamma\rho}^2$ for $\gamma\rho_n^-$ photoproduction. Solid red: no angular cut. Other curves show the effect of an upper angular cut θ for the outgoing γ: 35° (dashed blue), 30° (dotted green), 25° (dashed-dotted brown), 20° (long-dashed magenta), 15° (short-dashed purple) and 10° (dotted black). Upper left: $S_{\gamma N} = 10$ GeV^2. Upper right: $S_{\gamma N} = 15$ GeV^2. Bottom: $S_{\gamma N} = 20$ GeV^2.
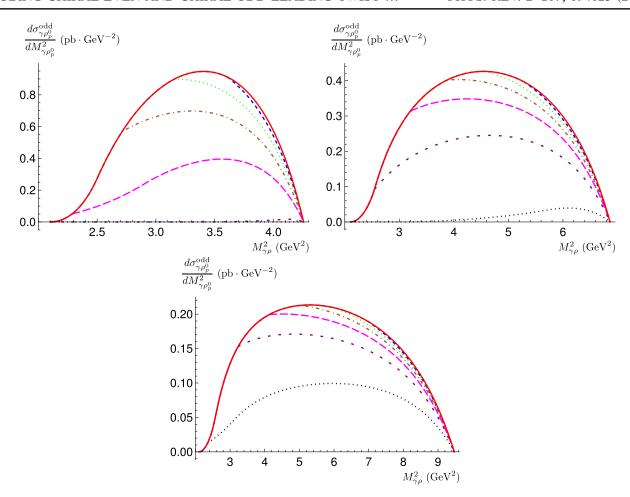
FIG. 53. The chiral-odd single-differential cross section as a function of $M^2_{\gamma\rho}$ for $\gamma\rho^0_p$ photoproduction. Solid red: no angular cut. Other curves show the effect of an upper angular cut θ for the outgoing γ: 35° (dashed blue), 30° (dotted green), 25° (dashed-dotted brown), 20° (long-dashed magenta), 15° (short-dashed purple) and 10° (dotted black). Upper left: $S_{\gamma N} = 10$ GeV^2. Upper right: $S_{\gamma N} = 15$ GeV^2. Bottom: $S_{\gamma N} = 20$ GeV^2.
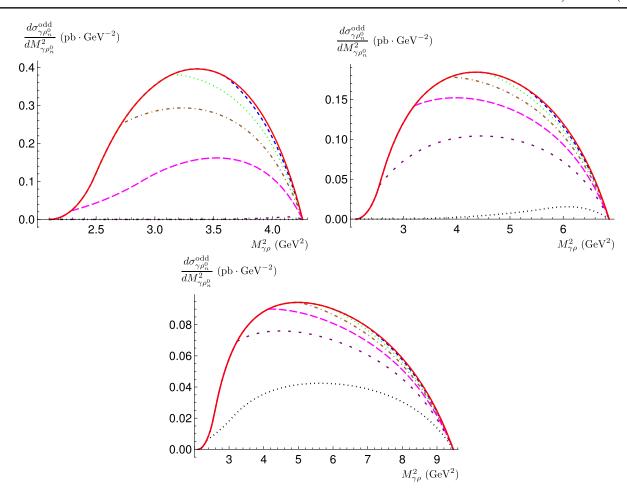
FIG. 54. The chiral-odd single-differential cross section as a function of $M_{\gamma\rho}^2$ for $\gamma\rho_n^0$ photoproduction. Solid red: no angular cut. Other curves show the effect of an upper angular cut θ for the outgoing γ: 35° (dashed blue), 30° (dotted green), 25° (dashed-dotted brown), 20° (long-dashed magenta), 15° (short-dashed purple) and 10° (dotted black). Upper left: $S_{\gamma N} = 10$ GeV^2. Upper right: $S_{\gamma N} = 15$ GeV^2. Bottom: $S_{\gamma N} = 20$ GeV^2.
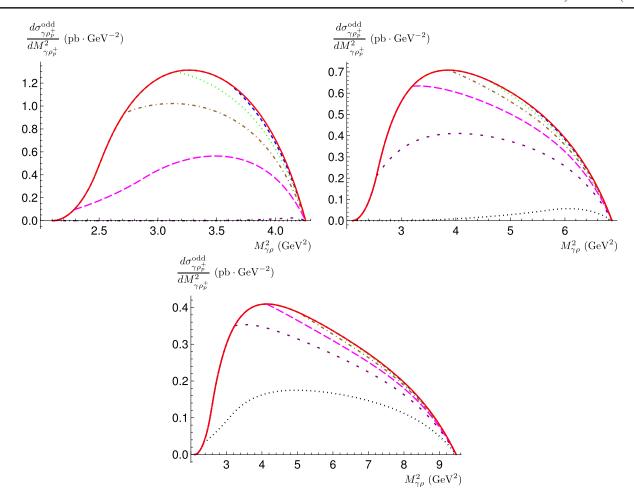
FIG. 55.   The chiral-odd single-differential cross section as a function of $M^2_{\gamma\rho}$ for $\gamma\rho^+_p$ photoproduction. Solid red: no angular cut. Other curves show the effect of an upper angular cut θ for the outgoing γ: 35° (dashed blue), 30° (dotted green), 25° (dashed-dotted brown), 20° (long-dashed magenta), 15° (short-dashed purple) and 10° (dotted black). Upper left: $S_{\gamma N} = 10$ GeV^2. Upper right: $S_{\gamma N} = 15$ GeV^2. Bottom: $S_{\gamma N} = 20$ GeV^2.
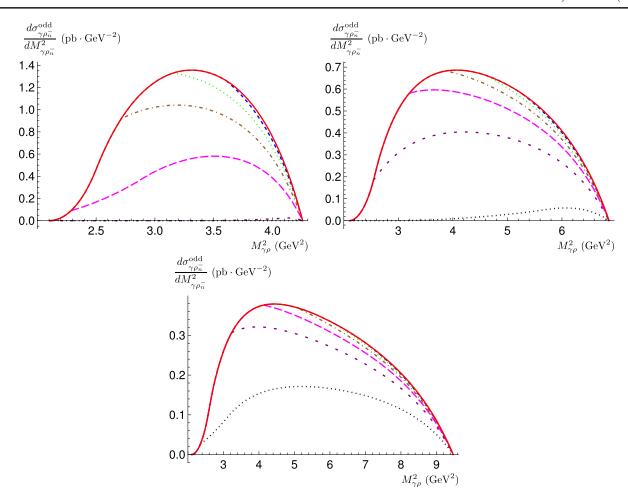
FIG. 56. The chiral-odd single-differential cross section as a function of $M_{\gamma\rho}^2$ for $\gamma\rho_n^-$ photoproduction. Solid red: no angular cut. Other curves show the effect of an upper angular cut θ for the outgoing γ: 35° (dashed blue), 30° (dotted green), 25° (dashed-dotted brown), 20° (long-dashed magenta), 15° (short-dashed purple) and 10° (dotted black). Upper left: $S_{\gamma N} = 10$ GeV^2. Upper right: $S_{\gamma N} = 15$ GeV^2. Bottom: $S_{\gamma N} = 20$ GeV^2.

APPENDIX C: VANISHING OF THE CIRCULAR ASYMMETRY IN THE CHIRAL-EVEN CASE

In this appendix, we discuss the vanishing of the circular asymmetry for the chiral-even case. For the circularly polarized amplitudes, the analogues of Eqs. (4.74) and (4.75) are given by

$$\sum_{\lambda_k} |\mathcal{M}_+|^2 = \frac{1}{2}\Big[2|C_A|^2 + |\vec{p}_t|^4|C_B|^2 + \frac{s^2}{4}|\vec{p}_t|^4|C_{A_5}|^2 + \frac{s^2}{4}|\vec{p}_t|^4|C_{B_5}|^2 - 2|\vec{p}_t|^2\mathrm{Re}(C_A^* C_B)$$
$$+ s|\vec{p}_t|^2\mathrm{Im}(C_A(C_{A_5}^* + C_{B_5}^*) + |\vec{p}_t|^2 C_{A_5} C_B^*)\Big], \tag{C1}$$

$$\sum_{\lambda_k} |\mathcal{M}_-|^2 = \frac{1}{2}\Big[2|C_A|^2 + |\vec{p}_t|^4|C_B|^2 + \frac{s^2}{4}|\vec{p}_t|^4|C_{A_5}|^2 + \frac{s^2}{4}|\vec{p}_t|^4|C_{B_5}|^2 - 2|\vec{p}_t|^2\mathrm{Re}(C_A^* C_B)$$
$$- s|\vec{p}_t|^2\mathrm{Im}(C_A(C_{A_5}^* + C_{B_5}^*) + |\vec{p}_t|^2 C_{A_5} C_B^*)\Big]. \tag{C2}$$

So,

$$\sum_{\lambda_k} |\mathcal{M}_+|^2 - \sum_{\lambda_k} |\mathcal{M}_-|^2 = s|\vec{p}_t|^2\mathrm{Im}(C_A(C_{A_5}^* + C_{B_5}^*) + |\vec{p}_t|^2 C_{A_5} C_B^*). \tag{C3}$$

An interesting feature of the circular asymmetry is that it only contains terms that mix vector GPD and axial GPD contributions (A and B, with A_5 and B_5). Thus, when averaging over the target helicity, it can be shown that all terms on the rhs of Eq. (C3) vanish. Indeed, using Eqs. (4.70) to (4.73), we obtain, after averaging and summing over the target helicities,

$$\frac{1}{2}\sum_{\lambda_1,\lambda_2}\left(\sum_{\lambda_k}|\mathcal{M}_+|^2 - \sum_{\lambda_k}|\mathcal{M}_-|^2\right) = \frac{|\vec{p}_t|^2}{(n\cdot p)}[\mathcal{H}_{\rho A}(\tilde{\mathcal{H}}^*_{\rho A_5} + \tilde{\mathcal{H}}^*_{\rho B_5}) + |\vec{p}_t|^2\tilde{\mathcal{H}}_{\rho A_5}\mathcal{H}^*_{\rho B}]\mathrm{tr}[\slashed{p}_2\slashed{n}\gamma^5\slashed{p}_1\slashed{n}] = 0. \qquad (C4)$$

This shows that for an unpolarized target, the circular asymmetry is identically zero. From a more physical point of view, the vanishing of the circular asymmetry is a consequence of parity invariance of QED and QCD. In particular, from Ref. [28], one deduces that the amplitude for our process, $\mathcal{M}_{\lambda_2\lambda_k;\lambda_1\lambda_q}$, has to obey the relation

$$\mathcal{M}_{\lambda_2\lambda_k;\lambda_1\lambda_q} = \eta(-1)^{\lambda_1-\lambda_q-(\lambda_2-\lambda_k)}\mathcal{M}_{-\lambda_2-\lambda_k;-\lambda_1-\lambda_q}, \qquad (C5)$$

where η represents a phase factor related to intrinsic spin. From this, we can deduce that

$$\sum_{\lambda_i,i\neq q}|\mathcal{M}_{\lambda_2\lambda_k;\lambda_1+}|^2 = \sum_{\lambda_i,i\neq q}|\mathcal{M}_{\lambda_2\lambda_k;\lambda_1-}|^2, \qquad (C6)$$

which implies that the circular asymmetry vanishes identically for an unpolarized target.

[1] G. Duplančić, S. Nabeebaccus, K. Passek-Kumerički, B. Pire, L. Szymanowski, and S. Wallon, Accessing chiral-even quark generalised parton distributions in the exclusive photoproduction of a $\gamma\pi$ pair with large invariant mass in both fixed-target and collider experiments, J. High Energy Phys. 03 (2023) 241.

[2] D. Y. Ivanov, B. Pire, L. Szymanowski, and O. V. Teryaev, Probing chiral odd GPD's in diffractive electroproduction of two vector mesons, Phys. Lett. B **550**, 65 (2002).

[3] R. Enberg, B. Pire, and L. Szymanowski, Transversity GPD in photo- and electroproduction of two vector mesons, Eur. Phys. J. C **47**, 87 (2006).

[4] M. El Beiyad, B. Pire, M. Segond, L. Szymanowski, and S. Wallon, Photoproduction of a $\pi\rho T$ pair with a large invariant mass and transversity generalized parton distribution, Phys. Lett. B **688**, 154 (2010).

[5] A. Pedrak, B. Pire, L. Szymanowski, and J. Wagner, Hard photoproduction of a diphoton with a large invariant mass, Phys. Rev. D **96**, 074008 (2017); **100**, 039901(E) (2019).

[6] B. Pire, L. Szymanowski, and S. Wallon, Diffractive deeply virtual Compton scattering, Phys. Rev. D **101**, 074005 (2020); **103**, 059901(E) (2021).

[7] A. Pedrak, B. Pire, L. Szymanowski, and J. Wagner, Electroproduction of a large invariant mass photon pair, Phys. Rev. D **101**, 114027 (2020).

[8] W. Cosyn and B. Pire, Diffractive rho plus lepton pair production at an electron-ion collider, Phys. Rev. D **103**, 114002 (2021).

[9] O. Grocholski, B. Pire, P. Sznajder, L. Szymanowski, and J. Wagner, Collinear factorization of diphoton photoproduction at next to leading order, Phys. Rev. D **104**, 114006 (2021).

[10] O. Grocholski, B. Pire, P. Sznajder, L. Szymanowski, and J. Wagner, Phenomenology of diphoton photoproduction at next-to-leading order, Phys. Rev. D **105**, 094025 (2022).

[11] J.-W. Qiu and Z. Yu, Exclusive production of a pair of high transverse momentum photons in pion-nucleon collisions for extracting generalized parton distributions, J. High Energy Phys. 08 (2022) 103.

[12] J.-W. Qiu and Z. Yu, Single diffractive hard exclusive processes for the study of generalized parton distributions, Phys. Rev. D **107**, 014007 (2023).

[13] R. Boussarie, B. Pire, L. Szymanowski, and S. Wallon, Exclusive photoproduction of a $\gamma\rho$ pair with a large invariant mass, J. High Energy Phys. 02 (2017) 054; 10 (2018) 29.

[14] G. Duplančić, K. Passek-Kumerički, B. Pire, L. Szymanowski, and S. Wallon, Probing axial quark generalized parton distributions through exclusive photoproduction of a $\gamma\pi^\pm$ pair with a large invariant mass, J. High Energy Phys. 11 (2018) 179.

[15] L. Mankiewicz, G. Piller, and T. Weigl, Hard leptoproduction of charged vector mesons, Phys. Rev. D **59**, 017501 (1999).

[16] M. Diehl, Generalized parton distributions, Phys. Rep. **388**, 41 (2003).

[17] A. V. Radyushkin, Double distributions and evolution equations, Phys. Rev. D **59**, 014030 (1999).

[18] M. Glück, E. Reya, and A. Vogt, Dynamical parton distributions revisited, Eur. Phys. J. C **5**, 461 (1998).

[19] M. Gluck, E. Reya, M. Stratmann, and W. Vogelsang, Models for the polarized parton distributions of the nucleon, Phys. Rev. D **63**, 094005 (2001).

[20] P. Ball and V. M. Braun, The Rho meson light cone distribution amplitudes of leading twist revisited, Phys. Rev. D **54**, 2182 (1996).

[21] R. Abdul Khalek et al., Science requirements and detector concepts for the electron-ion collider: EIC Yellow Report, Nucl. Phys. **A1026**, 122447 (2022).

[22] Y. V. Kovchegov, L. Szymanowski, and S. Wallon, Perturbative odderon in the dipole model, Phys. Lett. B **586**, 267 (2004).

[23] Y. Hatta, E. Iancu, K. Itakura, and L. McLerran, Odderon in the color glass condensate, Nucl. Phys. **A760**, 172 (2005).

[24] T. Lappi, A. Ramnath, K. Rummukainen, and H. Weigert, JIMWLK evolution of the odderon, Phys. Rev. D **94**, 054014 (2016).

[25] Z. Citron *et al.*, Report from Working Group 5: Future physics opportunities for high-density QCD at the LHC with heavy-ion and proton beams, CERN Yellow Rep. Monogr. **7**, 1159 (2019).

[26] C. Alexandrou, M. Constantinou, K. Hadjiyiannakou, K. Jansen, C. Kallidonis, G. Koutsou, A. Vaquero Avilés-Casco, and C. Wiese, Nucleon Spin and Momentum Decomposition Using Lattice QCD Simulations, Phys. Rev. Lett. **119**, 142002 (2017).

[27] C. Alexandrou, S. Bacchio, M. Constantinou, J. Finkenrath, K. Hadjiyiannakou, K. Jansen, G. Koutsou, H. Panagopoulos, and G. Spanoudes, Complete flavor decomposition of the spin and momentum fraction of the proton using lattice QCD simulations at physical pion mass, Phys. Rev. D **101**, 094513 (2020).

[28] C. Bourrely, J. Soffer, and E. Leader, Polarization phenomena in hadronic reactions, Phys. Rep. **59**, 95 (1980).